A Deuterated Neutron Detector Array for the Study of Nuclear Reactions with Stable and Rare Isotope Beams

by

Michael T. Febbraro

A dissertation submitted in partial fulfillment
of the requirements for the degree of
Doctor of Philosophy
(Applied Physics)
in the University of Michigan
2014

Doctoral Committee:

Professor Emeritus Frederick D. Becchetti Jr., Co-Chair
Assistant Professor Christine A. Aidala, Co-Chair
Associate Professor John E. Foster
Professor Cagliyan Kurdak
Associate Professor Sara A. Pozzi

In memory of my beloved mother who provided me with love, guidance, and support.

In spirit your encouragement and memory lives on. You are greatly missed.

Peggy Sue Riccobono

January 18, 1959 – March 4, 2013

ACKNOWLEDGEMENTS

To My Family – Sam Riccobono, Amber Febbraro, Rosalia and Joseph Riccobono. Thank you for your love and support.

Professor Frederick D. Becchetti – for providing me with the inspiration and opportunities over the years. Providing me with guidance but also the freedom to learn and make mistakes for myself. For the patience to work with me on numerous experiments, presentations, papers, and this dissertation. My sincere gratitude.

Professor James J. Kolata - Thank you for the years of guidance with the many experiments we have performed together. For showing me the important details on how to operate Van de Graaff accelerator. My sincere gratitude.

Mr. Ramon O. Torres-Isea – Thank you for the many hours of useful discussions, guidance, and incite throughout this work. You were an invaluable resource throughout my graduate education. My sincere gratitude.

Dr. Mitaire Ojaruega – Thank you for the years of guidance and friendship. You taught me the basics laboratory skills which led me to this point. In addition, you also were my inspiration for joining the applied physics program. My sincere gratitude.

Professor John Foster – Thank you for everything you have done for me during my undergraduate and graduate education. My favorite course during nuclear engineering undergraduate studies is still your plasma physics lab! You always made yourself available anytime I need advice on any topic. My sincere gratitude.

Dr. Alan Howard – Thank you for the many long hours spent at the accelerator setting up and working through these experiments with me. My sincere gratitude.

Professor Christine Aidala – Thank you for serving as co-chair for my thesis and taking me into your group. I've had many enlightening discussions with you and your group. I look forward to our future collaborative work.

Professor Sara Pozzi – Thank you for serving on my committee and the years of useful discussions in the field of nuclear safeguards and neutron detection.

Dr. Dan Robertson, Dr. Ed Stech, Dr. Wanpeng Tan, and all my friends at the University of Notre Dame Nuclear Structure Laboratory. I especially appreciate the warm welcome I received during my many visits to the lab. I'm looking forward to our future collaborative work together.

Dr. William Peters, Dr. Steve Pain, Dr. Ryan Clement, and all my friends from University of Tennessee, Idaho National Laboratory, Oak Ridge National Laboratory, and Rutgers University who welcomed me as one of your own, inviting me on many experiments and workshops with your group.

Professor Cagliyan Kurdak – Thank you for serving on for my thesis committee and your support in the applied physics program. You said when I first joined the AP program that AP is like a family. After many years in the program, I agree 100% with that statement. The program has supported me not only academically but also in the hardships outside the university. I can't thank you all enough for that.

Gabrielle Costello – I love you and thank you for being so supportive for all those long nights writing papers and running experiments and the many weeks we had to spend apart while I was away.

This work supported in part by NSF grant PHY 0969456.

TABLE OF CONTENTS

LIST OF TABLES

LIST OF FIGURES

LIST OF APPENDICES

LIST OF ABBREVIATIONS

AFM	atomic force microscopy
ANC	asymptotic normalization coefficient
APD	avalanche photodiode
CAMAC	computer automated measurement and control
CFD	constant-fraction discrimination (analog)
CM	center-of-mass frame of reference
CN	compound nucleus
CNO	carbon-nitrogen-oxygen cycle
CGNE	conjugate gradient normalized equations
DAQ	data acquisition
DCFD	digital constant fraction discrimination
DESCANT	Deuterated Scintillator Array for Neutron Tagging
DSP	digital signal processing
DPSD	digital pulse shape discrimination
DWBA	distorted-wave Born approximation
EJ	Eljen (Eljen Technologies)
FAIR	Facility for Antiprotons and Ion Research
FRIB	Facility for Rare Isotope Beams
FWHM	full width at half max
gs	ground state
GSI	Gesellschaft für Schwerionenforschung

HPGe	high-purity germanium
ISNAP	Institute for Structure and Nuclear Astrophysics
LAB	laboratory frame-of-reference
MLEM	maximum-likelihood expectation maximization
MSU	Michigan State University
n-TOF	neutron time-of-flight
NIM	nuclear instrumentation module
OM	optical model
OMP	optical model potential
PMT	photomultiplier tube
RIB	radioactive ion beam
RNB	radioactive nuclear beam
RBS	Rutherford backscatter
RSICC	Radiation Safety Information Computational Center
PSD	pulse-shape discrimination (analog)
SEM	scanning electron microscope
SiSB	silicon surface barrier
SNM	special nuclear material
TOF	time-of-flight (anything other than neutrons)
TTA	triplet – triplet annihilation
UM	University of Michigan
UM-DSA	University of Michigan Deuterated Scintillator Array
UND	University of Notre Dame
VANDLE	Versatile Array for Neutron Detection at Low Energy
VME	Versa Module Europa

LIST OF SYMBOLS

n_s	Concentration of electronic singlet states
n_t	Concentration of electronic triplet states
k_{TT}	Triplet-triplet annihilation rate constant
S_n	Electronic singlet excitation state at level n
T_n	Electronic triplet excitation state at level n
S	Astrophysical S factor
SF	Spectroscopic factor
$\mathcal{S}$	Spectroscopic strength
R	detector resolution
η	Sommerfeld parameter
ℓ	Orbital angular momentum
$\mathscr{v}$	Viscosity
L	light response

Chapter 1

Introduction

I. Motivation

In the past two decades the field of nuclear physics has expanded its experimental boundaries to radioactive nuclei historically thought unachievable. We are now in the 103rd year since the publication of Rutherford's groundbreaking paper describing properties of the atomic nucleus [Rut11]. Pushing further into the *sea of instability* toward the nuclear drip lines, which serve as the divider for bound and unbound nuclei, modern nuclear physics requires novel instrumentation and methods to progress our understanding of the natural world. This *sea of instability* is made up of short-lived exotic nuclei with fascinating properties which impact the observable (and unobservable) universe around us. To understand these exotic nuclei, measurements must be performed to determine their masses, half-lives, energy levels, as well as spin and parity of their states, which are needed to develop an understanding of their nuclear structure.

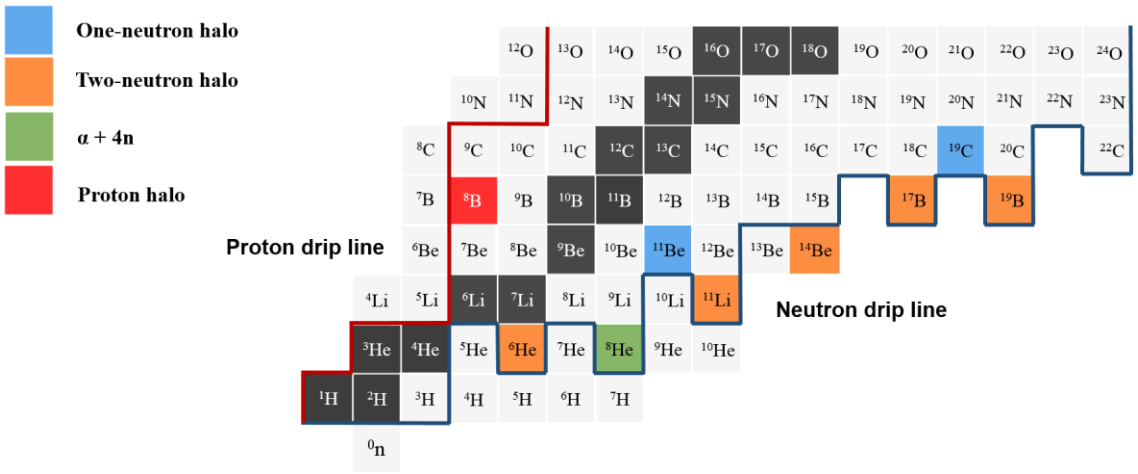

Figure 1.1 Portion of the chart of nuclei shown with neutron and proton drip lines and halo nuclei (based on [Ber07]).

These parameters are observables which allow us to infer the structure and configuration of nucleons within their cores. ^{11}Li for example is bound with a half-life of 8.75 ms compared to ^{10}Li which is neutron unbound by 25 keV with a half-life ~10^{-20} s (Γ = 230 keV) [ENDF/B-VII.0]. The high relative stability of ^{11}Li compared to ^{10}Li leads to one such property known as a Borromean-halo nuclei model which consists of a tightly bound core coupled to two loosely-bound neutrons. In the case of the neutron Borromean-halo nucleus ^{11}Li, its neutron halo extends out to a nuclear radius approximately equal to that of ^{208}Pb. An interesting observation is that if any piece of the 3-body nuclear system is broken, the entire system becomes unstable as if they were linked Borromean rings. ^{11}Li is by no means the only halo system, in fact many other halo nuclei have been observed (see Figure 1.1).

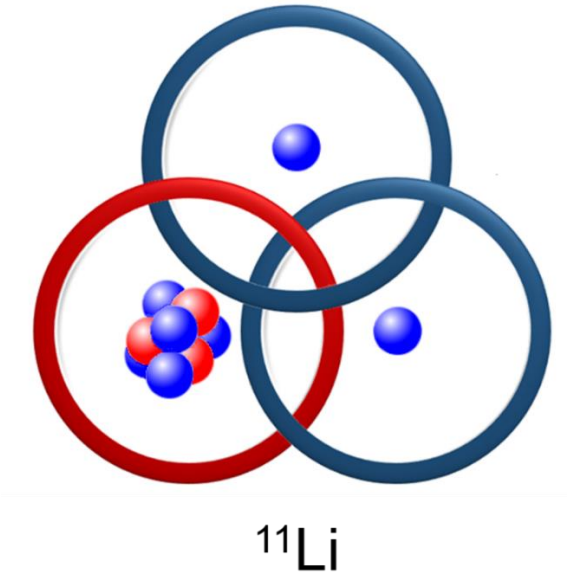

Figure 1.2 The Borromean nucleus ^{11}Li (based on [Ber07]).

These exotic nuclei are pushing the limits of existing theories and opening the door for new ones. This capability came about with the introduction of rare isotope beams (RIBs). Because many of these RIBs are far from stability, beam production cross sections and subsequent beam intensities are very low, typically < 10^6 particles/s. This has limited the type of experiments one can perform with such beams, mostly to those requiring the detection of charged particles. Few experiments have been conducted with RIBs which involve the detection of an outgoing neutron. The net neutrality of the neutron makes direct detection nearly impossible and thus less-efficient

indirect detection techniques must be used. Historically, the method of choice has been neutron time-of-flight (n-ToF) which relies on a measure of the flight time over a known flight path to determine the neutron's kinetic energy. This technique is often not possible when neutron energies are high, beam intensities are low, a non-pulsed accelerator must be used, or when room restrictions limit the use of a long-path n-ToF array.

Similarly, in the field of nuclear astrophysics, neutron detection has had minimal use due to the very low reaction cross sections. To address this issue high beam intensity stable-beam accelerators have been developed to maximize beam fluence on target, hence increasing the reaction rate. These high- intensity accelerators are typically DC machines and require additional beam bunching and pulse selection hardware to be used with n-ToF. However, this often reduces the overall beam intensity by a factor of 10 or more. ^{3}He detectors and (n,γ) converters have been used but they are very sensitive to background neutrons and in the case of (n,γ) converters, background γ-rays near the capture γ-energies. What is needed is a detection system which can provide neutron spectroscopic measurements without the use of n-ToF. This system would provide an alternative technology which can complement both reactions with RIBs and low cross section stable-beam measurements, which often occur for stellar processes. The system also would need good n/γ discrimination capability since separation via timing would not be assessable.

In a 1979 paper, titled "Development of organic scintillators", F.D. Brooks postulated the potential benefits of deuterated scintillators over conventional hydrogen-based scintillators for neutron spectrum measurements [Bro79]. Two years later, P.M. Lister in collaboration with F.D. Brooks, completed his thesis at the University of Birmingham on "Experimental reaction studies with polarized ion beams" in which spectrum unfolding was used with deuterated benzene (benzene-d_6, C_6D_6) based liquid and deuterated anthracene (anthracene-d_{10}, $C_{14}D_{10}$) [Lis81]. The results were published the same year in a conference proceeding [Bro81]. P.M. Lister concluded that improvement of unfolding codes and detectors with higher resolution were needed to improve the technique. In 1988, based on these conclusions, F.D. Brooks et al. published a paper introducing the deuterated anthracene spectrometer (DAS) [Bro88] which was an improved version of an older design. Over the next two decades, deuterated scintillators were used in a few experiments such as measurements of cold fusion [Rob90, Rob92] which included a measurement

setting a limit on cold-fusion neutron production [Rob90] and also other studies pertaining to the neutron decay of ^{120}Sb [Rob95]. These experiments all utilized neutron spectroscopy without n-ToF to extract neutron energy spectra. A few years later M. Ojaruega et al. [Oja10] (deuterated benzene) at the University of Michigan, showed that conventional pulse-shape discrimination (PSD) techniques, using discrete analog NIM and CAMAC modules can effectively be used to study reactions such as (d,n) and (^{3}He,n) involving neutrons without the measurement of n-ToF. Likewise in 2008, a team led by Paul Garret at University of Guelph started working on a large spherical 70 detector deuteated-liquid detector to be used for coincident neutron tagging [Gar13].

These detectors exploit the fact that the n + d cross sections, unlike n + p cross sections, are asymmetric for neutron energies in the range of a few keV to >150 MeV. This results in a forward-going recoil deuteron in the scintillator, produced with most of the incident neutron energy (i.e. $E_{d,max} = (8/9)E_n$)[1]. Thus, a distinct peak in the scintillator light spectrum is generated with a peak location directly related to the incident neutron energy [Oja10, Feb13, Feb14]. Such detectors should be well suited for experiments involving RIBs and astrophysics measurements since they can provide usable neutron energy spectra without measurement of the n-ToF. ToF, if available, can then be used if needed to separate beam impurities, i.e. secondary-beam analogs (e.g. ^{6}He from ^{4}He) in the RIB, or to reduce the neutron and gamma-ray background from room sources. In particular, background from room-return neutrons, which can be a problem with long-path neutron ToF systems, is greatly reduced.

Also, in recent years, the use of waveform digitizers for digital signal processing (DSP) has led to new possibilities for improved neutron detector systems. In particular, neutron-gamma digital pulse-shape-discrimination (DPSD) has made it possible to develop improved algorithms for optimal particle identification in liquid scintillators.

The importance of neutrons in nuclear research especially at RIB facilities such as the *TwinSol* [Lee99, Bec03] device at the ISNAP (Institute for Structure and Nuclear Astrophysics)

[1]Maximum energy transferred to the recoil in a neutron-nucleus elastic collision is $E_r|_{max} = (1 - \alpha^2)E_n$ where $\alpha = \frac{A-1}{A+1}$. [Kno00]
For a neutron + deuteron elastic collision, $\alpha = \frac{2-1}{2+1}$ and $E_r|_{max} = (1 - \alpha^2)E_n \rightarrow \left(1 - \frac{1}{9}\right)E_n$
$E_d|_{max} = \frac{8}{9}E_n$

laboratory at the University of Notre Dame (UND) and RIB facilities currently under construction such as FRIB (Facility for Rare Isotope Beams) [Tho10] at Michigan State University and FAIR (Facility for Antiproton and Ion Research) [Nil08] at GSI (Gesellschaft für Schwerionenforschung) stress the need for new, dedicated neutron spectroscopy instruments.

II. Description of Problem

Since most measurements of large cross-section nuclear reactions involving neutrons can utilized pulsed accelerator and neutron time-of-flight (n-ToF) methods for neutron spectroscopy, the use of deuterated scintillator was not always justified. As noted, there is now interest in studying nuclear reactions where n-ToF may not be feasible or optimal for the needed measurements and includes:

- Study of nuclear reactions using low-intensity secondary RIBs where long-path n-ToF is inefficient [Feb13, Oja10].
- Study of stable-beam reactions at large angles where n-ToF arrays cannot often be used and where cross sections at large angles can better define the reaction mechanism [Feb13, Oja10].
- Measurements at low energies for reactions of interest in nuclear astrophysics which often must utilize high-intensity DC i.e. non-pulsed accelerators, some even located underground [Feb13].
- Applications in homeland security and in particular detection and identification of neutron-emitting special nuclear material (SNM) where n-ToF is not practical [Law13].
- Coincident measurements e.g. n-γ where neutron scattering from a conventional ^{1}H-based scintillator can generate excessive $n + p \rightarrow d + \gamma$ γ-ray background [Pla03, Bor07].

Thus the goal of this work was to develop, evaluate, and implement a modern, digital-signal-processing (DSP) based deuterated scintillator array using fast waveform digitizers for the study of reactions involving neutrons where n-ToF may not be feasible or optimal. This entailed development of a Versa Module Europa (VME) based data-acquisition software, PSD

optimization, new improved data analysis procedures using deuterated detectors, and development of effective neutron-spectrum unfolding algorithms. Evaluation of the array was made by comparison of cross section measurements using the array to known cross sections measured using traditional n-ToF. The array will be noted by its acronym; the UM-DSA (University of Michigan Deuterated Scintillator Array).

III. Author's Contributions to This Work

The introductory chapters are meant to supply supplementary information on the specific aspects of the system and the nuclear models to be employed. The subsequent chapters describe the experimental measurements performed, which span various sub-fields of modern nuclear physics. The epilogue discusses possible future measurements and applications of the system. A list of the author's primary contributions to this and related work are as follows:

- Developed the DAQ software and event-mode DAQ system (with advice from Mr. Ramon Torres-Isea)
- Designed and fabricated gas target, n-beam scanner, Faraday cups, and many other components of thesis-related accelerator experiments
- Developed improved techniques for producing C_2D_4 targets
- Developed technique for producing single-sided oxygen targets on thin tantalum foils
- Developed neutron unfolding codes
- Wrote and published papers demonstrating that neutron spectroscopy can be conducted without n-ToF measurements
- Successfully implemented several off-site thesis-related accelerator experiments
- Collaborated on experiments with many research groups nationally and internationally
- Supervised 7 undergraduate students in medical physics, detector development, nuclear physics, and nuclear engineering research (with Prof. Becchetti)

Chapter 2

Instrumentation

I. Anatomy of a Neutron Detector Array

As the field of nuclear physics progresses, current technological limits are expanded and barriers must be overcome to meet new sets of challenges. In the case of neutron detection, spectroscopy is critical for measurement of physical observables of quantum-mechanical systems. With the shift toward radioactive beams and exploration of nuclei far from stability, a new set of challenges are introduced;

- Low beam intensity (typically $10^3 – 10^6$ particles per second)
- Beam purity issues
- Reactions often must be performed in inverse kinematics
- Beam-induced background is often high as beam itself is radioactive

The neutron detection system described in this dissertation has been designed to address these challenges. Of these challenges, low beam intensity is the major driving force for developing such new technologies.

The following sections will focus on the major components of the array which is comprised of fast waveform digitizers, the data acquisition system (DAQ), and the array of deuterated liquid scintillator detectors.

II. Fast Waveform Digitizers

In contrast to traditional analog electronics, fast waveform digitizer allow for the acquisition of detector signals by discrete digitization of the incoming waveforms. Typical digitization rates range from 250-1000 megasamples/s (MS/s) and up to 5000 MS/s for specialized applications at 10-14 bit resolution. This capability allows for simpler experimental setups with all signal processing done in software rather than hardware. The latter requires many modules, each susceptible to electronic noise, impendance mismatching, and other issues. In the case of neutron detection in which detector efficiency is energy-threshold dependent, the removal of active elements from the circuit reduces potential sources of gain shift to only two elements: the PMT and digitizer. Another important feature is that global triggers permit digitization of multiple channels with the same sampling clock. This allows for the application of advanced algorithms for precision timing measurements between channels e.g. as demonstrated with the VANDLE neutron array [Pau14]. Event-mode data recording of the digitized signals allows for optimization of the data-analysis software during and after the experiment.

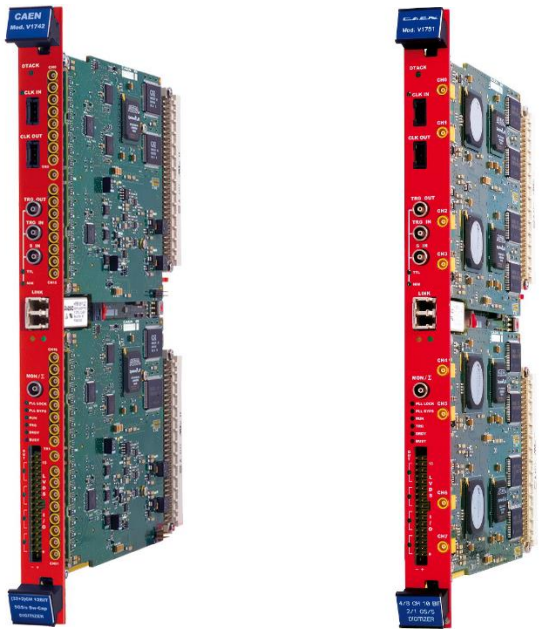

Figure 2.1 - CAEN 1742 (left) and CAEN 1751 (right) fast waveform digitizers. (Figure from CAEN technologies) [CAN42,CAN51].

For the UM-DSA, both the CAEN V1751 and CAEN V1742 fast waveform digitizers [CAN51, CAN42] were evaluated. The CAEN V1751 is a 1-2 GS/s 10-bit 4-8 channel fast waveform digitizer [CAN51]. In 2 GS/s mode operation, only 4 channels are usable. The CAEN V1742 is a 1-5 GS/s 12-bit 32+2 channel fast waveform digitizer [CAN42]. Both digitizers have a 1 V_{pp} dynamic range.

III. Data Acquisition System (DAQ)

Digitizers present additional challenges over traditional analog-to-digital (ADC) devices primarily due to their large data output per trigger per channel. For example, if you have four channels of a traditional 12-bit ADC, each time an event is triggered the system will transfer four 12-bit integers to memory. With a 12-bit fast waveform digitizer operating at 1 GS/s for a 1μs window, the data throughput increases to a thousand 12-bit integers per event per channel! This leads to an enormous amount of data throughput for even the most modest of experiments. Also, once the waveform arrives at the processing computer, the event must undergo digital signal processing (DSP) to extract basic pulse information. Without large computing power, it is often not possible to view the full data stream in 'real time' and monitoring of the data must be done using a small, manageable fraction of the total data stream. Based on these complications and others, there is currently only a small number of specialized DAQ systems which can be used with digitizers. For the UM-DSA, the decision was made to create our own DAQ which would be tailored for use with deuterated scintillators and permit modifications as the evaluation of the system was underway.

The DAQ was designed around the VME framework with a communication link supplied by a VME crate controller. High voltage supply, digitizers, and data management are all controlled in software. Details are given in Appendix E.

The primary VME-based DSP system employs two iSeq VHS-404 four-channel programmable high-voltage power supplies, a CAEN V1751 8/4-channel 10-bit 1/2 GS/s digitizer, and a Struck SIS3150 USB2 VME controller [Stu50]. Communication with the VME crate is done

using a simple USB 2.0 connection from the Struck SIS3150 VME controller or more recently with a fiber-optic communication link directly to the CAEN digitizer units. The custom data-acquisition software, which includes a user-friendly GUI, was written by the author in the C language using LabWindows CVI®. It controls every aspect of the VME system including the PMT high voltage power supplies, digitization settings, data acquisition with event-mode recording, and implementation of the DPSD algorithm.

The software allows for the storage of full-event waveforms or pseudo real-time event processing for compressed data storage. In pseudo real-time event processing mode, the user is given the option of storing sampled full-event waveforms at a user-defined interval. In addition, the digitizer system was adapted to detect and identify coincident recoils such as ^{3}He ions from the ^{2}H(d,n) reaction using a ΔE-E silicon-surface-barrier (SiSB) detector telescope. This permits spectral and efficiency measurements for coincident neutrons at selected emission angles with specific, well-defined neutron energies, and similar coincident measurements. Details are given in Appendix E.

The PSD can be optimized using the DSP software and real-time display system developed via suitable signal averaging of the main PMT pulse and likewise to determine and correct for any d.c. voltage offsets on the incoming signals. Also, since the digitizer input signals are limited to 1.0 volt maximum amplitude, suitable i.e. high-bandwidth attenuators are used to reduce the PMT signals as needed. This allows the PMTs to be operated at or near their stated operating high voltage to maintain good signal-to-noise characteristics in the PMT. The PMT HV is then adjusted slightly if necessary to optimize the DPSD. In addition to DPSD, the digitized signal and the signals in adjacent channels can be used for coincident timing (e.g. for associated-particle coincidence). In this case a digital constant-fraction discrimination (DCFD) algorithm (typically set at 50% of the maximum pulse height) is applied to the digitized signals to provide fast timing signals from each detector. As noted, the latter can include both energy and timing signals generated by a silicon surface-barrier detector telescope to provide coincident, and hence mono-energetic neutrons for efficiency measurements.

Both the DPSD (using a long gate/ falling-edge short gate algorithm) and DCFD timing can be optimized online during an experiment. However, if needed additional improvements can

be done off-line during a replay of the experiment using the fully-digitized data stored in event-mode on large data disks.

IV. Liquid Scintillator Detectors

1. Liquid scintillators

The current setup for the UM-DSA consists of a combination of 5.08 cm diameter x 5.08 cm and 10.16 cm diameter x 15.24 cm EJ-315 deuterated-benzene (C_6D_6) based organic scintillator detectors. In addition, the enhanced PSD liquid EJ-315M scintillator and non-deuterated benzene (C_6H_6) based liquid EJ-315H scintillator were evaluated. All liquid detectors used were supplied by Eljen Technology [Eljen]. Each detector consists of an aluminum housing coated with TiO_2 based reflective coating (EJ-520) and a 6.3 mm thick Pyrex® glass window. An expansion gap of 3% by volume of nitrogen gas is contained within the aluminum housing. The PMTs are magnetically shielded within a formed MuMetal® housing. Optical coupling of the PMT to the scintillator canister is done with either optical coupling grease (EJ-550) or by a silicone rubber optical interface pad (EJ-560). All measurements unless stated were taken with the detectors in the horizontal position, with minimal light losses due to the expansion bubble. Table 2.1 lists the properties of the detectors used in this work. Throughout the dissertation, for simplicity the detectors will be referred to by their scintillator liquid and assigned ID listed in Table 2.1.

Table 2.1 – Organic Liquid Scintillators used in this work

Scintillator	ID	Dimensions (cm)	PMT	PMT base	V. Divider chain
EJ-315	2x2	5.08 dia. x 5.08	ETEL 9807B	Eljen -VD23-9807	Divider A[1]
EJ-315	4x6	10.16 dia. x 15.24	ETEL 9821B	Eljen – VD43-9821	Divider A[2]
EJ-315H	2x2	5.08 dia. x 5.08	ETEL 9807B	Eljen -VD23-9807	Divider A[1]
EJ-315H	4x6	10.16 dia. x 15.24	ETEL 9821B	Eljen – VD43-9821	Divider A[2]
EJ-315M	4x6	10.16 dia. x 15.24	ETEL 9821B	Eljen – VD43-9821	Divider A[2]
EJ-315M	5x5	12.70 dia. x 12.70	Hamamatsu R1250	Eljen – VD53N-1250	Std. Div.[3]

[1][9807B]
[2][9821B]
[3][R1250]

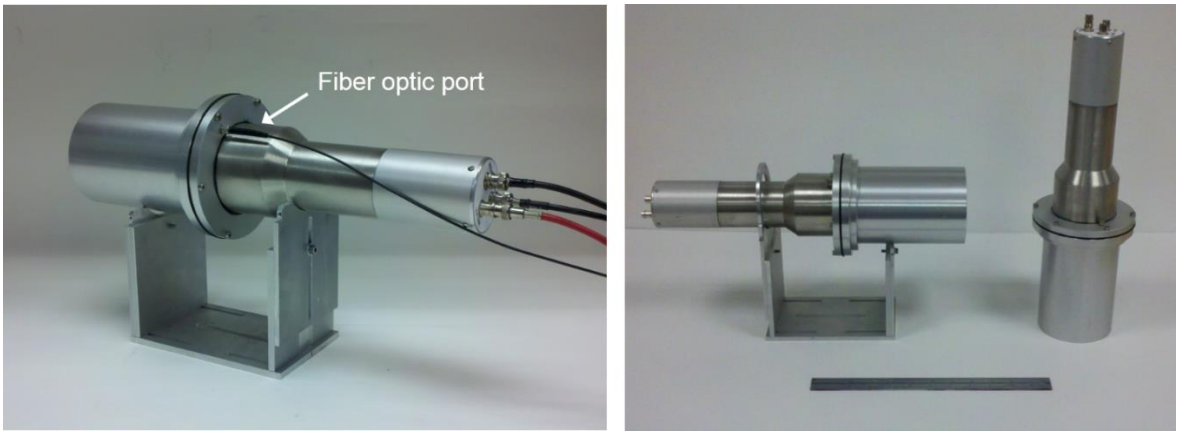

Figure 2.2 – Rear and side view of the 4x6 EJ-315 detector with fiber optic port labeled.

2. Photomultiplier tubes and bases

Details of the bialkali photocathode PMTs, PMT bases, and divider chain for each detector used are shown in Table 2.1. All measurements were taken using the anode output of the PMT base. Electrical schematics of the bases are shown in Appendix D. A SMA-type fiber optic port located on the flange (see Figure 2.4) provides an input for a stable LED pusler, such as the CAEN SP5601 [CAN56] to monitor PMT drift and noise during an experiment. Figure 2.3 shows the detectors which were evaluated for this work. The results in this dissertation will focus on the 2x2, 4x6 and 5x5 detector sizes.

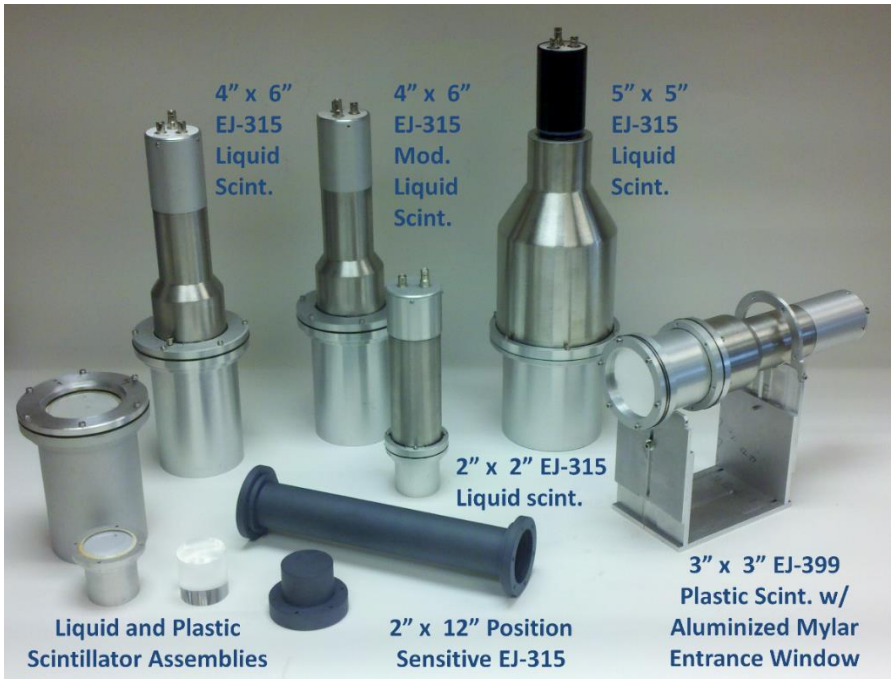

Figure 2.3 - Organic scintillators evaluated in this work.

Chapter 3

Neutron Detection

I. Organic Scintillators

Organic scintillators are a class of radiation detectors which rely on a scintillation material, in this case hydrocarbon-based compounds, to convert ionizing radiation (~MeV in energy) into scintillation photons (~eV). The number of scintillation photons produced is then related to the energy deposited by the incident ionizing particle. These photons, in the visible to UV spectrum, may then be detected using an optical-photon detector such as a photomultiplier tube (PMT) or avalanche photodiode (APD).

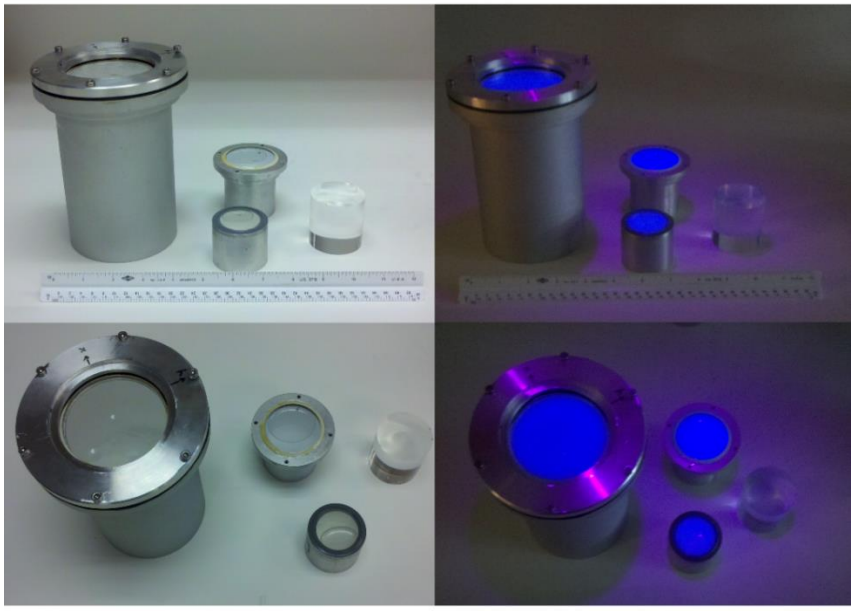

Figure 3.1 - EJ-315, NE-213 liquid scintillators, and EJ-200 plastic scintillator under white light (left) and UV illumination (right).

There are two main types of organic scintillating systems: unitary systems and binary systems. In unitary systems, the scintillation material consists of a single aromatic compound in ether a liquid, crystalline, or polymeric state. Unitary systems such as single-crystal anthracene and *p*-terphenyl (1,4-Diphenylbenzene) exhibit very high photon yield and n/γ pulse shape discrimination (PSD) with respect to liquid organic scintillators. In binary systems, the scintillation material consists of an aromatic solvent such as toluene or xylene and a solute of an organic fluorescent compound. This permits the use of fluorescent compounds with high quantum efficiency which may be difficult to produce as a unitary system (i.e. as a crystal, polymer, etc.).

The source of scintillation photons in organic scintillators is the product of *radiation transitions* in electronic energy levels of fluorescent molecules. These electronic energy levels are populated as the ionizing particle deposits energy into the material exciting π elections in the aromatic rings of the fluorescence species. The radiation transitions can occur by fluorescence (spin-allowed transitions of singlet states) or phosphorescence (spin-forbidden transitions of triplet states) which are known by their fast and slow decay times, respectively [Kno00]. *Radiationless transitions* are also prevalent in organic scintillators in the form of *intersystem crossing*, *internal conversion*, *vibrational relaxation*, and the *up conversion process* or *triplet-triplet annihilation* (TTA) as represented in the Jablonski diagram in Figure 3.2. Of these *radiationless transition* processes, it is the TTA process that is important to this work and is in discussed in §3.4.

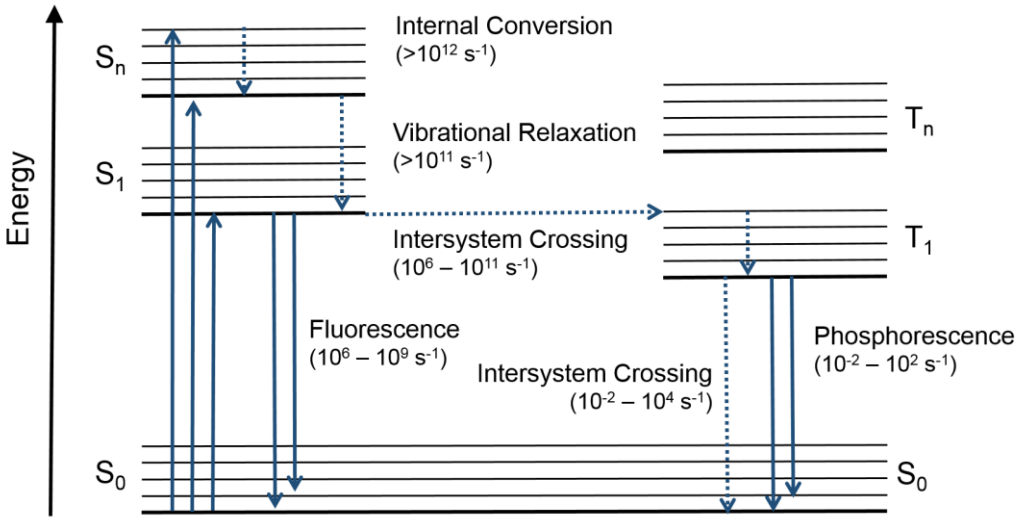

Figure 3.2 - Jablonski diagram (based on [Mon06]).

In the case of organic scintillators for neutron detection, a fast prompt decay time and capability for pulse-shape discrimination are typically desired. In addition, engineering aspects such as ease of manufacturing into desired geometry, stability to mechanical stress, temperature dependence, and flammability also must be taken into consideration. Properties of the scintillators used in this work are shown in Table 3.1.

Table 3.1 – Properties of liquid scintillators used in this work

Property*	EJ-315	EJ-315H	EJ-315M	EJ-309
Light output (% Anthracene)	60%	60%	60%	75%
Photons per MeVee (electron)	9200	9200	9200	11,500
Prompt decay time (ns)	3.5	3.5	3.5	3.5
Max. emission (nm)	425	425	425	424
Refractive index	1.498	1.501	1.494	1.57
# D atoms / cm^3	4.06×10^{22}	-	4.02×10^{22}	-
# H atoms / cm^3	2.87×10^{20}	4.04×10^{22}	3.10×10^{20}	5.43×10^{22}
# C atoms / cm^3	4.10×10^{22}	4.06×10^{22}	4.12×10^{22}	4.35×10^{22}

*References: [EJ315], [EJ315H], [EJ315M], [EJ309]; See also Appendix B

II. ^{1}H versus ^{2}H for Neutron Detection

As noted, deuterated scintillators exploit the fact that the n+d cross sections, unlike the n+p cross sections, are asymmetric for neutron energies in the range of a few keV to > 50 MeV (shown in Figure 3.3 at E_n = 11.5 MeV).

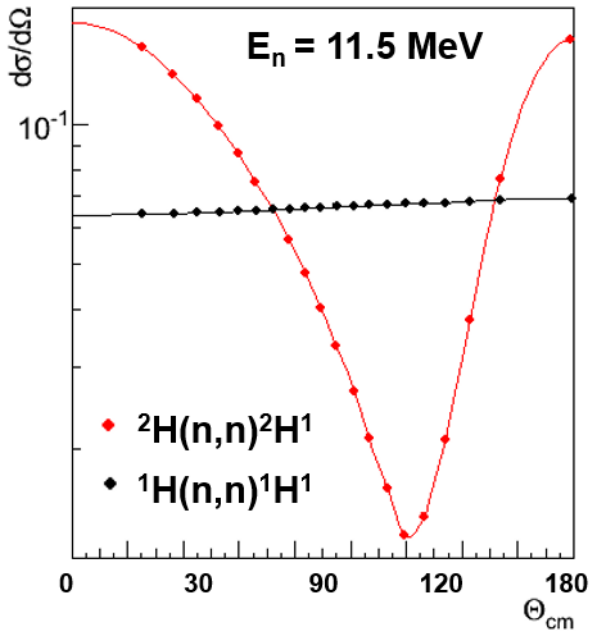

Figure 3.3 – n+p and n+d elastic scatter cross sections at E_n=11.5 MeV. [1][ENDF/B-VII.0].

This results in a forward-going recoil deuteron in the scintillator, produced with most of the incident neutron energy ($E_{d,max} = (8/9)E_n$). Thus a distinct peak in the scintillator light spectrum is generated with the peak directly related to the incident neutron energy [Oja11, Feb13]. The resulting light response spectrum in both cases takes on the shape of the elastic scatter cross section convoluted with the detector response. An example of this effect is demonstrated with C_6D_6 and C_6H_6 in Figure 3.4.

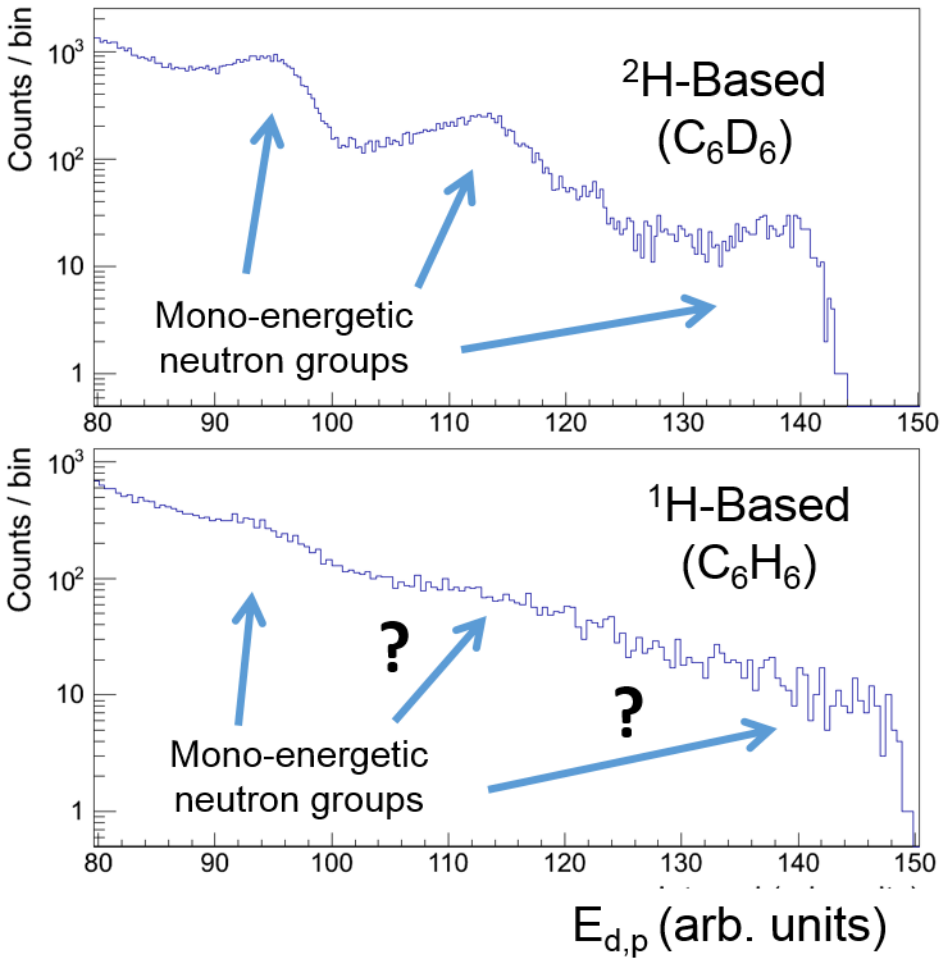

Figure 3.4 – Comparison of deuterated (C_6D_6) and non-deuterated (C_6H_6) organic scintillators to 3 monoenergetic neutron groups. The deuterated scintillator shows a clear advantage in identification of the monoenergetic neutron groups.

Three clear peaks from three incident mono-energetic neutron groups are visible in the deuterated scintillator spectrum (C_6D_6) but are not visible in the standard hydrogen based scintillator (C_6H_6) to the unbiased eye. This is the underlining feature which make deuterated scintillators an attractive option for neutron spectroscopy without n-ToF measurement.

III. Light Response

The primary interaction for gamma rays in the scintillator is gamma-electron elastic scattering, known as Compton scattering, where a gamma ray transfers a portion of its energy to an atomic electron which in turn ionizes the scintillator material from energy losses along the path, dE/dx. From reaction kinematics, this results in a continuous distribution of electron energies

governed by the Compton scatter formula. The recoil electron energy from a gamma-electron collision is as follows,

$$\frac{1}{E_f} - \frac{1}{E_i} = \frac{1}{m_e c^2}[1 - \cos(\theta_{cm})] \tag{3.1}$$

$$E_e = E_i - \frac{m_e c^2}{(1 - \cos(\theta_{cm})) + \frac{m_e c^2}{E_i}} \tag{3.2}$$

where E_i and E_f are the intial and final gamma-ray energies, E_e is the recoil electron energy, and $m_e c^2$ is the rest mass of the electron (511 keV). The shape of the Compton-spectra response from a mono-energetic gamma-ray source is governed by the scattering cross section for the gamma-electron elastic scattering, given by the Klein-Nishina formula [Kno00].

The primary interaction for neutrons is elastic and inelastic scattering with an atomic nucleus in the scintillator, e.g. hydrogen, deuterium, or carbon. Similar to the electron case, ionizations occur as the energetic recoil nucleus travels through the scintillation medium depositing energy from dE/dx losses. Since elastic and inelastic scattering can involve any nucleus in the scintillator and surrounding material having sufficient energy to enter the scintillation material, all relative cross sections must be taken into account. This leads to a complication in determining the spectral response shape and typically requires a Monte Carlo calculation with all relative isotopes and cross sections included.

So far, this discussion has included the process of scintillation and a prediction of the shape based on scattering kinematics and cross sections. We will now expand on the relationship between the energy deposited and the number of scintillation photons produced, known as the *light- response function* $L(E)$. The light response of an organic scintillator to ionizing particles can be described by the well-known extended Birks formula [Kno00],

$$\frac{dL}{dx} = \frac{S_{eff}\frac{dE}{dx}}{1 + kB\frac{dE}{dx} + C\left(\frac{dE}{dx}\right)^2} \tag{3.3}$$

where dE/dx is the energy loss per track length and S_{eff}, kB and C are constants. S_{eff} is known as the normal scintillation efficiency and kB is the quenching probability. C is an adjustable parameter which has been shown to improve the empirical fit to experimental data. Birk's formula illustrates a few important properties. When dE/dx is small, as is the case for electrons, Equation 3.3 reduces to a linear regime where the light response is *proportional* to the energy deposited

$$\left.\frac{dL}{dx}\right|_e \approx S_{eff}\frac{dE}{dx} \tag{3.4}$$

and hence

$$L \approx \int_0^E \left.\frac{dL}{dx}\right|_e dE = S_{eff}E \tag{3.5}$$

When dE/dx is large, as is the case for recoil nuclei, Equation 3.3 becomes a constant and it is said that the light response reaches a saturation limit at $\frac{S_{eff}}{kB}$. This phenomenon is known as the *pulse-height deflect*. Empirical studies of this effect for a range of ions has been well-documented in plastic scintillators by F.D. Becchetti [Bec76] and others. They have shown that the process can be described by the empirical formula as follows,

$$L \approx \int_0^E \left.\frac{dL}{dx}\right|_e dE = S_{eff}E \tag{3.6}$$

$$L(E) = CZ^a(R - bZ) \tag{3.7}$$

where a and b are empirically-fit constants, R is the range of the ion in (mg/cm^2), Z is the atomic number, and C is a normalization constant. In practice, the light response function of organic scintillators for Z$\leq$ 6 are measured experimentally and empirically fit well with the following equation,

$$L(E_x) = aE_x + b(1 - e^{cE_x}) \tag{3.8}$$

where E_x is the initial energy of the ionizing particle (i.e. electrons E_e, protons E_p, …) and a and b are again empirically-fit constants [Law13].

IV. Calibration

The absence of a photo peak in the gamma spectra owing to the low Z of the scintillator material requires the use of some other unambiguous and distinct feature of the light spectrum from which a relationship for with energy deposited can be drawn. A typical calibration procedure is to use the Compton edge produced by standard gamma ray sources in which the edge represents the maximum energy imparted to a recoil electron from Compton scattering in units of MeVee[2]. The use of the edge itself brings some level of ambiguity as it is a convolution of the Compton continuum and the detector resolution leading to an overall broadening of the edge. Extraction of the edge, and in turn the overall calibration, is now partially dependent on the resolution of the detector. To reduce this complication, the systematic procedure of [Die82] should be used. In the method of [Die82], a Monte Carlo simulation of the detector is made with and without the detector resolution included, the prior yielding the actual location of the Compton edge. The location at which these spectra intersect is the position of the Compton edge for the spectra with resolution as shown in Figure 3.5. In practice this is often reported as a percent of the total height.

[2] By definition, 1MeVee ≡ 1 MeV energy deposited by an electron

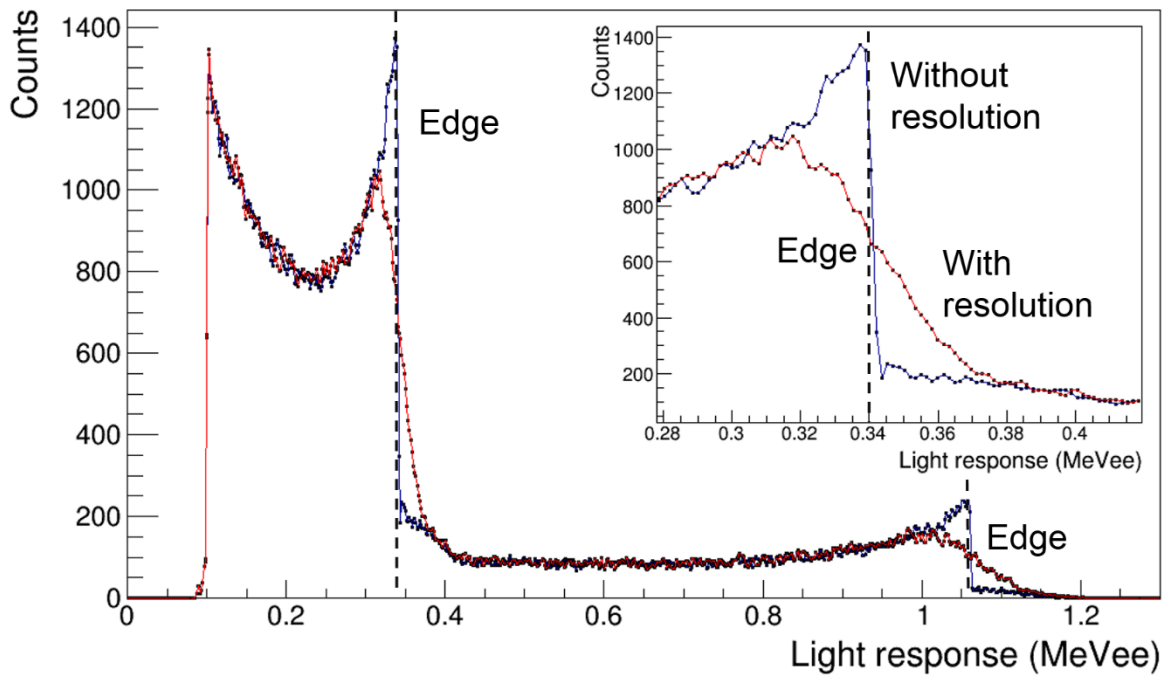

Figure 3.5 – A simulated ^{22}Na spectrum showing the location of the Compton edges with and without detector resolution included.

The same procedure can also be applied to data involving the light response from n+p or n+d elastic scattering in the scintillator.

V. Pulse-Shape Discrimination

In the design of an array for fast neutron spectroscopy without the use of n-ToF it is essential that the detector have the capability to discriminate between many possible incident particles such as cosmic-ray muons, γ rays, and neutrons. In traditional n-ToF systems, neutrons can be discriminated from γ-rays originating from a beam pulse by their difference in flight times[3]. This of course limits one to pulsed accelerators with sufficient beam bunching. Historically, organic crystals and liquids have shown excellent discrimination capabilities towards μ/γ/n but until recently not plastics. This discrimination is done by comparing the pulse shapes of the recoil

[3] Collective trends only, not on an event-by-event basis.

ions, i.e. pulse-shape discrimination (PSD). There is a slight subtlety in the term γ/n discrimination that must be addressed. One is not discriminating the γ/n directly but their associated recoil particles. I will refer to the recoil particle instead of the incident particle for the rest of this discussion for reasons that will soon become clear.

$S_1 \rightarrow S_0 + h\nu_f$	Fluorescence
$S_n \rightarrow T_n$	Intersystem crossing
$T_1 \rightarrow S_0 + en$	Internal conversion
$T_1 \rightarrow S_0 + h\nu_p$	Phosphorescence
$T_1 + T_1 \rightarrow \begin{cases} T_1 + S_0 + en \\ 2S_0 + en \\ S_0 + S_1 \end{cases}$	Partial self-quenching Total self-quenching P-type delayed fluorescence
$T_1 \xrightarrow{Thermal} S_1$	E-type delayed fluorescence
$I^+ + e^- \rightarrow \begin{cases} S_n & (\sim 25\%) \\ T_n & (\sim 75\%) \end{cases}$	Ion recombination

Figure 3.6 - A few examples of intermolecular and excitation processes in organic scintillators (adapted from D.L. Horrocks [Hor70]).

As the incident neutron energy increases, more reaction channels open up. In the case of deuterium, the low binding energy leads to a large cross section for deuteron breakup, d(n,nnp) in the scintillator. At higher neutron energies, reactions on carbon such as $^{12}C(n,\alpha)^{9}Be$, $^{12}C(n,n')3\alpha$, and $^{12}C(n,p)^{12}B$ can occur with E_{thres} = 6.18, 8.29, and 13.69 MeV respectively [Uwa82]. This unfortunately, introduces additional particles which must be discriminated, e/p/d/α. In order to understand the problem at hand, I will develop a basic model for the generation of the pulse shapes.

To begin, I'll go back to the electronic mechanisms which govern scintillation (shown in Figure 3.6). If we consider a finite volume element along the ionization track, we can write population equations for the singlet and triplet electronic state concentrations as a function of time. These equations can be broken down into three characteristic time scales: short, long, and

intermittent. Short and long time scales are dominated by prompt fluorescence and phosphorescence, respectively [Kno00].

$$\frac{dn_S(t)}{dt} = -\frac{n_S(t)}{\tau_S} + \gamma n_T^2(t) - D\nabla^2 n_S(t) \cong -\frac{n_S(t)}{\tau_S} + \gamma n_T^2(t) \tag{3.9}$$

$$\frac{dn_T(t)}{dt} = -\frac{n_T(t)}{\tau_T} - 2\gamma n_T^2(t) - D\nabla^2 n_T(t) \cong -\frac{n_T(t)}{\tau_T} - 2k_{TT} n_T^2(t) \tag{3.10}$$

The dominant source of fluorescent photons for the intermittent time scales, is the delayed fluorescence processes, which is a result of singlet-state production from TTAs (P-type) and thermally induced intersystem crossing (E-type). The energy deposition along the track can be approximated as the stopping power for length R given by the continuous slowing-down approximation (CSDA). The intensity of photons from delayed fluorescence scales as the square of the concentration of triplet states multiplied by a rate constant k_{TT}, known as the Auger up-conversion coefficient. Because TTA relies on molecular interactions, the value of k_{TT} depends on the temperature T, and the viscosity ν, of the system [Hor70]. It can be approximated as follows,

$$k_{TT} = \frac{3000\, RT}{\nu} \tag{3.11}$$

The triplet-state differential equations can be solved with initial condition $n_T(0)$. Then by inserting this solution into the singlet-state differential equations with initial conditions $n_S(0)$, we arrive at the following time, temperature, and viscosity-dependent singlet population equation:

$$n_S(t) = n_S(0)e^{-\frac{t}{\tau_S}} + e^{-\frac{t}{\tau_S}} \int_0^t f(t)\, dt \tag{3.12}$$

Prompt Fluorescence + Delayed Fluorescence

$$f(t) = \frac{k_{TT} n_T^2(0) e^{\frac{t}{\tau_S}}}{\left(e^{\frac{t}{\tau_T}} - 2k_{TT}\tau_T n_T(0)\left(1 - e^{\frac{t}{\tau_T}}\right)\right)^2} \tag{3.13}$$

As mentioned above, the initial conditions $n_S(0)$ and $n_T(0)$ are related to the stopping power multiplied by the number of excitations per deposited energy and the quantum efficiency for the radiation transitions. The concentration of triplet states for a given particle energy per unit volume increases with increasing stopping power dE/dx. Equations 3.12 and 3.13 then state that this results in an increase in delayed fluorescence yield for increasing particle mass (A) and charge (Z). Particle discrimination can then be made by comparison of delayed fluorescence to the total fluorescence (shown in Figure 3.7). In summary, the non-linearity in the differential concentration equations leads to the discrimination of particles.

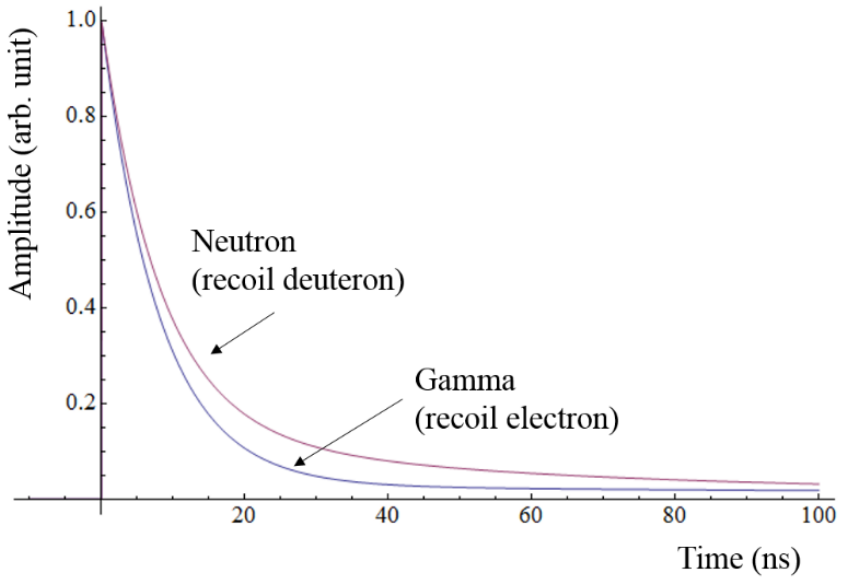

Figure 3.7 - Scintillation decay curves from a simple model showing neutron and gamma discrimination.

This basic PSD model agrees quite well with the recent success in PSD-capable plastic scintillators (i.e. EJ299-33), which were produced by increasing the concentration of fluorescent compound in the plastic, thus increasing the collisional probability and subsequent k_{TT}. Now one may ask "why wasn't that done sooner?" which is a fair question. The answer lies in the stability of the plastic matrix. Previously, increasing the fluorescent compound caused the solute to precipitate out of the matrix over time degrading the optical properties of the plastic. The first plastic capable of PSD called 'Plastic 77', was demonstrated in 1958 by [Bro58]. A commercial PSD plastic NE-150 [Hor70, Rou64] based on 'Plastic 77', was produced but suffered from

stability issues from clouding of the plastic overtime and never had widespread use [Hur14]. New, improved versions of PSD plastics now exist [Zai12] which appears to be more stable.

Using the above simple model of PSD, the optimal location of the offset parameter relative to the start of the pulse can be determined by finding the maximum of the delayed to total fluorescent yield, shown graphically in Figure 3.8. This agrees well with values used to optimize PSD.

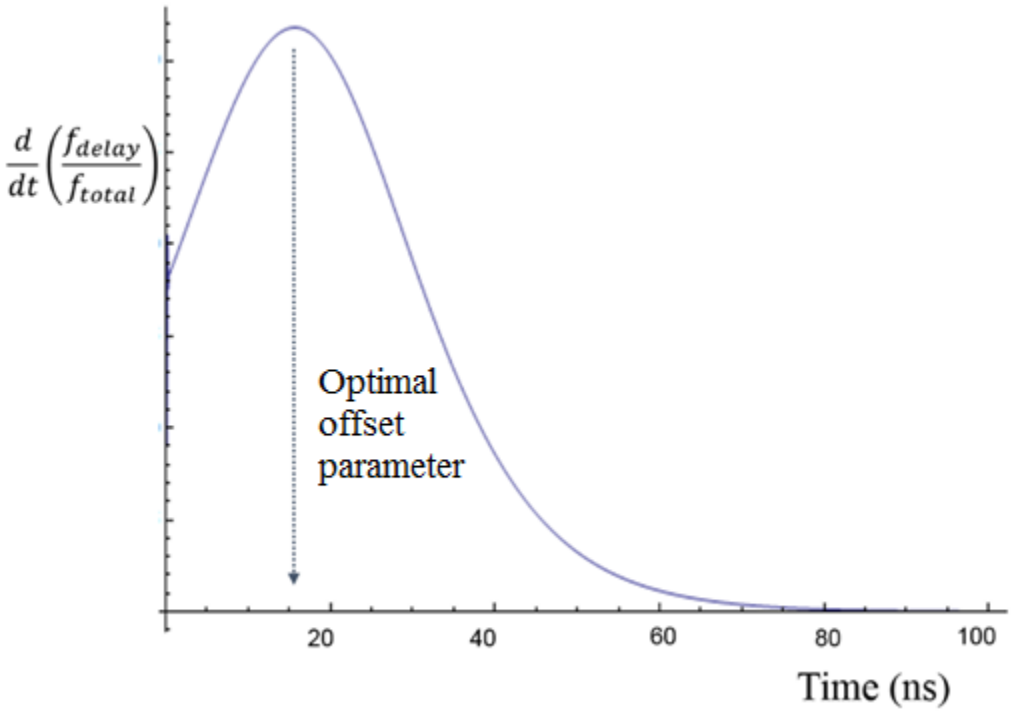

Figure 3.8 - Optimization of the offset parameter from the simple PSD model.

VI. Spectrum Unfolding

We will now turn our attention to the process of extraction of a neutron spectrum with organic scintillators i.e. spectrum unfolding. In particular, it has been shown that deuterated scintillators exhibit an advantage over hydrogen-based scintillators for spectrum unfolding [Law14] due to improvement in the condition of the response matrix. It is thought that this improvement originates from a reduction in the oscillatory error and invertability of the matrix due

to the increased elastic cross section at maximum recoil deuteron energy ($E_d = 8/9E_n$) known as the recoil peak [Feb13]. The nomenclature of a recoil peak is solely based on observation that the response to mono-energetic neutrons appears to have a 'peak' in the continuum. This is analogous to the nomenclature used in describing the 'photo-peak' for gamma-rays in high-Z scintillators. The appearance of this peak is particularly useful as a quasi-quantitative identification of neutron energy groups in light-response spectra prior to unfolding into neutron energy spectra.

1. Description of the problem

As discussed in the previous sections, neutron detection in organic scintillators relies on the elastic scattering of neutrons with atomic nuclei in the bulk scintillation material. The resulting recoil ion induces molecular excitation and subsequent photons which are detected and amplified by a high-gain photo detector (PMT, APD, etc). Because each interaction results in a continuous probabilistic scattering distribution from $\theta \in (0, \pi)$, a mono-energetic neutron group results in a continuum in the light response spectrum. Mathematically, this system can be described by a Fredholm integral equation of the first kind where the kernel function is the detector response function $\mathcal{R}(\ell, E)$ with incident neutron spectrum $\emptyset(E)$ and light response $N(\ell)$.

$$N(\ell) = \int \mathcal{R}(\ell, E)\emptyset(E)dE \tag{3.14}$$

The measurement then gives the superposition of individual light response $N(\ell)$ for the incident spectrum $\emptyset(E)$. It is useful from a numerical point-of-view to approximate this system as a linearly discretized matrix equation as follows:

$$\bar{S} = \bar{\bar{R}}\bar{x} \tag{3.15}$$

where $\bar{\bar{R}}$ is known as the response matrix of the detector with incident neutron spectrum $\bar{x}$ and light response $\bar{S}$. The extraction of the neutron spectrum $\bar{x}$ from the measured light-response spectrum $\bar{S}$ results in an ill-posed matrix inversion problem. As stated, there have been many

algorithms developed for solving these types of inverse problems. The resulting neutron energy spectra after spectrum unfolding is a *probabilistic distribution* of neutrons. Thus one cannot correlate neutrons on an event-by-event basis without additional information. This is drastically different than n-ToF, in which neutrons of a specific energy (i.e. ToF) ideally correlate to specific events. If an experiment requires correlated observables for example, experimental designs using this technique must permit projection of neutron spectra from another physical observable rather the contrary.

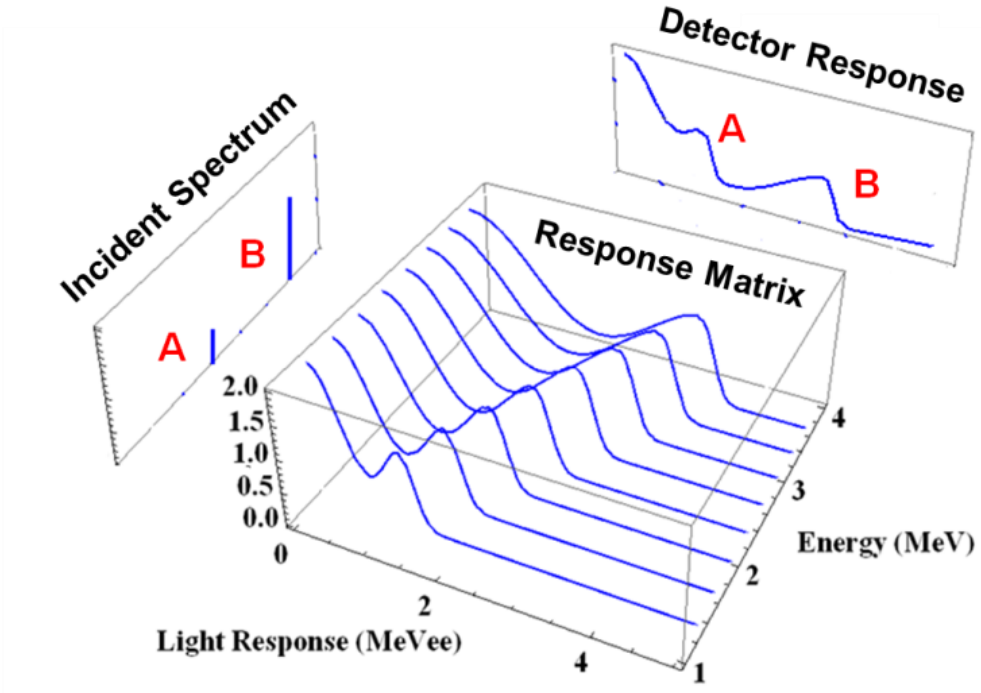

Figure 3.9 - Graphical interpretation of Equation 3.15.

Early mention of this technique in deuterated scintillators dates back to a 1979 paper by Frank D. Brooks [Bro79] with physics results on vector analyzing powers for $^{12}C(d,n)^{13}N$, $^{9}Be(d,n)^{10}B$, and $^{28}Si(d,n)^{29}P$ released in 1981 [Bro81, Lis81]. The deuterated-anthracene crystal scintillator used in these early experiments became known later as the deuterated-anthracene spectrometer (DAS) [Bro88].

2. Maximum–Likelihood Expectation Maximization (MLEM)

One particularly attractive spectrum unfolding algorithm is the maximum-likelihood expectation maximization method (MLEM) [Peh13]. The MLEM algorithm falls under the large class of Bayesian inference methods. To understand how Bayesian inference methods can be used for spectrum unfolding we'll review a simple example.

Let's start by representing an incident neutron spectrum as probability distribution $\bar{x}$. After many measurements we obtain a spectral detector response $\bar{s}$. We can then begin to ask the question, "given the makeup of $\bar{s}$, what is the likelihood of an incident spectrum $\bar{x}^k$" where the superscript k represents the k^{th} estimate. This is analogous to asking "given n flips of a coin, what is the *fairness* of the coin?" where fairness is a parameter of the probability distribution just as incident neutron energy is a parameter of the probability distribution $\bar{x}$. Each measure of $\bar{s}$ becomes evidence which is used to infer probability distribution $\bar{x}$ according to Bayes's rule.

The MLEM method starts with defining a likelihood function for the process. In the case of liquid scintillators, the likelihood function can be represented with a Poisson distribution. This representation is quite natural since it accounts for the Poisson nature of noise in the light response spectra [Peh13].

$$P = \prod_{i=1}^{I} \frac{e^{-\mu_i}(\mu_i)^n}{n!} \tag{3.16}$$

The expectation value $\mu_i = \sum_j^J R_{ij}\, x_j$ where $\bar{S} = \bar{\bar{R}}\bar{x}$ as defined in Equation 3.15. Inserting this expression into Equation 3.16 we arrive at the likelihood function for the detectors.

$$P = \prod_{i=1}^{I} \frac{e^{-\sum_j^J R_{ij} x_j} \left(\sum_j^J R_{ij}\, x_j\right)^{S_i}}{S_i!} \tag{3.16}$$

It is common to define the log-likelihood function to avoid negative values, which converts the product into a sum.

$$\ln(P) = \sum_{i=1}^{I}\left[-\sum_{j}^{J} R_{ij}\, x_j + S_i \ln\left(\sum_{j}^{J} R_{ij}\, x_j\right) - ln(S_i!)\right] \tag{3.17}$$

Given a set of measurements which composes $\bar{S}$, we'd like to determine the likelihood of that this distribution is the result of a neutron energy bin x_j. To do this we can take the derivative of the log-likelihood function with respect to x_j.

$$\frac{\partial \ln(P)}{\partial x_j} = \sum_{i=1}^{I}\left[-R_{ij} + S_i \frac{S_i R_{ij}}{\sum_j^J R_{ij}\, x_j}\right] \tag{3.16}$$

Equation 3.16 can be iteratively solved where $x_j^{(k+1)}$the new estimate from previous estimate is $x_j^{(k)}$ shown in Equation 3.17.

$$x_j^{(k+1)} = x_j^{(k)} \sum_{i=1}^{l} R_{ij} \frac{S_i}{\sum_{l=1}^{J} R_{il} x_l^{(k)}}, \quad j = 1, \ldots, J \tag{3.17}$$

The response matrix $\bar{\bar{R}}$ can then ether be determined by experiment or simulation using a Monte Carlo transport code. A simulated response matrix for the 5x5 EJ-315M scintillator is shown in Figure 3.10.

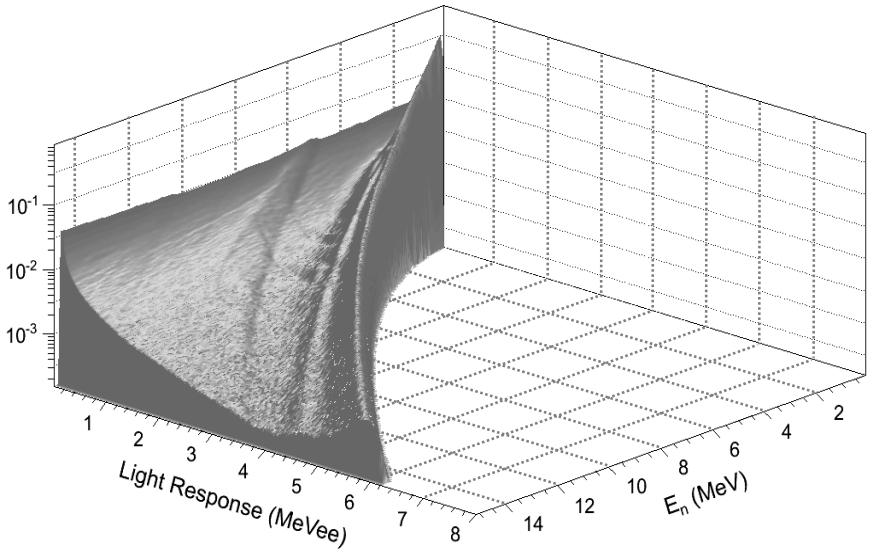

Figure 3.10 - Simulated response matrix for the 5x5 EJ-315M detector.

VII. Methods for Pulse Shape Discrimination (PSD)

1. Zero cross-over method

The zero cross-over method was one of the early techniques for the discrimination of particle based on the differences in their associated decay times. The benefit of this method over a total-charge to pulse-height method previously used is that the method is *independent* of pulse height [Owe62, Ale61] which eliminates any corrections that must be made in pulse-height *dependent* techniques. In the analog circuit, the signal is split into two copies typically using a linear fan in/out. One copy is sent into a constant fraction discriminator (CFD) to generate a start signal. The other copy is first integrated and then differentiated twice in order to obtain a baseline cross over (ie. zero cross over), which can then be fed into a zero cross-over pick off to generate a stop signal. The start and stop signals can then be fed into a time-to-amplitude convertor (TAC) or time-to-digital converter (TDC) to generate a pulse which is proportional to its decay time and *independent* of the initial pulse height [Owe62, Ale61]. The robustness and simplicity of this method is shown in its ability to accept essentially any smooth pulse with a rise and fall decay time within the bandwidth of the electronics.

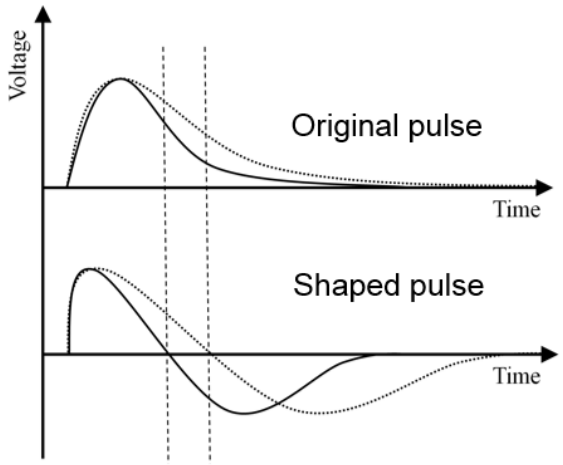

Figure 3.11 - Zero cross-over method with time differences clearly shown: gamma ray pulse (solid) and neutron pulse (dotted).

The method, which was originally developed using analog electronics, is not trivial to implement in digital systems because of error propagation associated with numerical differentiation on a discrete set of samples. Noise and fluctuations in the pulse shape can lead to erratic behavior in the differentiated set. Typically, smoothing or filtering algorithms such as moving average is applied to the set prior to numerical differentiation.

2. Charge-integration method

The charge-integration method is a popular discrimination technique of particle types due to its simplicity and easy implementation within digital systems. In this method, particle discrimination is made by comparing the total charge-pulse integral (also known as the 'long integral') to the tail charge-pulse integral (also known as the 'short integral'). In the case of organic scintillators for example, this is a measure of the prompt fluorescence versus delayed fluorescence. This method is easily implemented in both analog and digital systems. In the analog version, the signal is copied into two pairs typically using a linear fan in/out. Each pair is then composed of a charge and gate signal. The charge signal is sent to a charge-to-digital converter (QDC) which is gated using the gate signal passed through a CFD. The width of the logic pulse (NIM signal) of the CFD is set to span the length of the initial pulse. This yields the total charge integral. The short integral, is essentially the same configuration as the long integral with the exception of a delay added between the CFD and QDC. This delays the gate by a prescribed time after the beginning of the initial pulse to generate the short charge integral (see Figure 3.12).

The quality of discrimination is strongly dependent on the starting location of the short gate and must be optimized for each detector and PMT voltage setting. The PMT voltage setting sensitivity comes from the fact that, in PMTs, the transit time (typically 10-30 ns) is a function of the applied voltage which governs the time-spread width of the anode charge pulse.

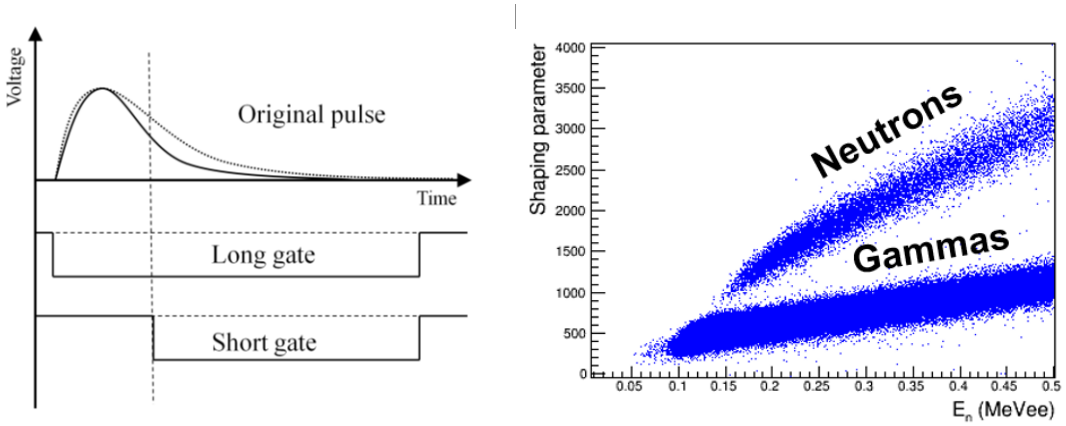

Figure 3.12 – Charge-integration method showing relative time settings for charge-integration gates. Left: Gamma-ray pulse (solid) and neutron pulse (dotted). Right: Results showing separation of neutron and gamma-ray events.

3. Neural networks

A recent and attractive method for the discrimination of particle types involves the use of neural networks. In this method, an Artificial neural network (ANN) is typically created as a Multi-Layer Perceptron (MLP). A three or more layered, feed-forward model is trained to map input sets (in this case detector signals) to give an appropriate output or particle ID. The quality of discrimination is dependent on the training set used to generate the weighting constants in the ANN. This can be done by using a time-of-flight (ToF) technique or coincident recoil tagging [i.e., tagging the ^{3}He recoil from the d(d,n)^{3}He reaction] for neutrons and gamma to create a training set of neutron data with gamma-ray rejection. Results from a simple example are shown in Figure 3.13.

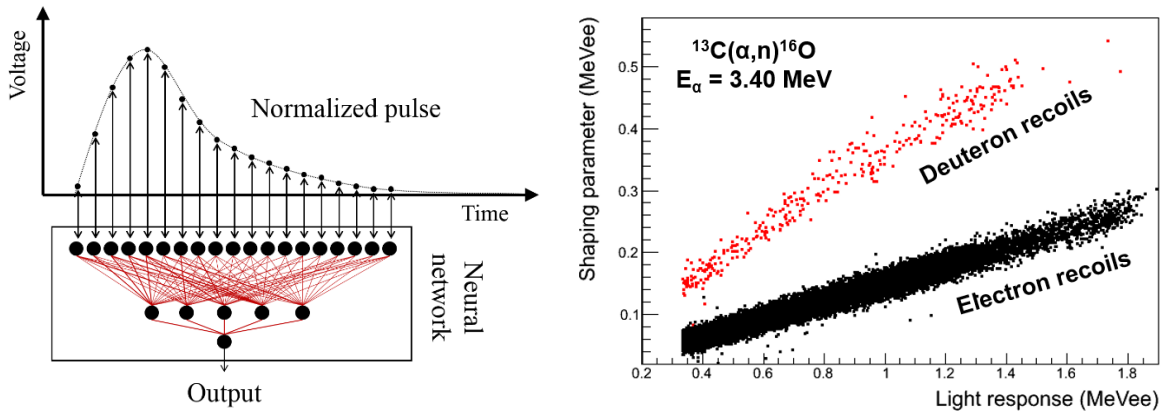

Figure 3.13 - Left: Neural network method showing the input stream of a normalized pulse, hidden layers of neurons, and single output. Right: Results for a simple ANN with neutron events in red (deuteron recoils) and gamma events in black (electron recoils).

Unlike the zero cross-over and charge-integration methods, ANN discrimination is made on a point-by-point basis over the range of a pulse instead of just two parameters. It has been shown that this point-by-point comparison reduces the misidentification probability for neutrons and gammas [Liu09]. In certain situations, false identifications can be produced if additional noise, impedance mismatching, or aging of the scintillator and/or PMT, resulting in significant distortions of pulse shapes. Processing rates of ~2.9 μs/event (~345 kHz) have been reported [Ron09] for 71 inputs.

4. Other methods

Other techniques for particle identification, again mainly between gamma rays and neutrons using fuzzy logic [Luo10], wavelet transforms [You09], pulse-gradient analysis (PGA) [Mel07, Asp07], and a correlation method [Kor03] have been reported with varying degrees of success.

Chapter 4

Nuclear Transfer Reactions

I. Direct Nuclear Reactions

Direct nuclear reactions are a type of nuclear reaction in which target – projectile interactions occur over a short time period i.e. on the order of the nuclear transversal time and do not proceed with formation of a compound nuclear state. Within the category of direct reactions exist three main subcategories; elastic scattering, inelastic scattering, and transfer reactions. Of these three, inelastic scattering and transfer reactions are interesting from a reaction mechanism and structure perspective. The former mechanism often results in excitation of collective modes such as rotational and vibrational bands [Ber04]. The latter mechanism often results in a rearrangement of the nucleon composition of the target-projectile system. Both reactions provide a useful tool to probe particle states and thus serve as a test for the nuclear shell model. The simplest type of transfer reaction is the single- nucleon transfer reaction in which an exchange of a single nucleon occurs. These include for example (d,n) or (d,p) stripping reactions and (n,d) or (p,d) pickup reactions. The weakly bound deuteron serves as an ideal nucleus for these types of reactions due in part to having a single neutron and proton and no bound excited states. The (d,p) and (d,n) reactions on stable nuclei were studied extensively during the 1950-1970s when interest then shifted toward heavy-ion transfer reactions. The recent introduction of radioactive ion beams with reasonable intensities has renewed interest in (d,n) and (d,p) transfer reactions with these exotic and short-lived nuclei to probe nuclear models at the limits of nuclear stability [Ber04].

In this chapter, I will discuss the theoretical aspects of transfer reactions, what are the measureable observables, and how this relates to neutron spectroscopy measurements. Since I will

be studying the (d,n) reaction with the UM-DSA, I will briefly outline the nuclear model (Distorted-Wave Born Approximation) that will be used to analyze the (d,n) data (Chapter 7).

II. Basics of Transfer Reactions

Transfer reactions allow for the measurement of many useful properties of nuclei. In particular, the angular distributions contain a rich amount of information regarding the transfer reaction. The transferred angular momentum ℓ is limited to values of,

$$\left|\left|J_i - \ell\right| - \frac{1}{2}\right| \leq J_f \leq J_i + \ell + \frac{1}{2} \tag{4.1}$$

where J_i and J_f are the spin of the target and product nucleus, respectively [Ber04]. Likewise, the initial and final parities are limited to values given by the relationship,

$$\pi_i \pi_f = (-1)^{\ell} \tag{4.2}$$

The shape of the angular distribution can be described using a simple semiclassical approach [Ber04]. For example consider a A(d,n)B reaction with incoming deuteron momentum $\vec{p}_d$, outgoing neutron momentum $\vec{p}_n$, and transfer proton momentum $\vec{q}$. The transferred angular momentum becomes,

$$\vec{\ell} = \vec{R} \times \vec{q} \tag{4.3}$$

Now applying conservation of linear momentum,

$$q^2 = p_d^2 + p_n^2 - 2|\vec{p}_d||\vec{p}_n| cos(\theta_\ell) \tag{4.4}$$

One obtains a relationship between the magnitude of the transferred angular momentum ℓ and the angle θ_ℓ, where the latter represents the first maximum in the angular distribution (Figure 4.1). This can be simplified further to obtain,

$$\theta_\ell \approx const \times \ell \tag{4.5}$$

Therefore θ_ℓ increases with ℓ.

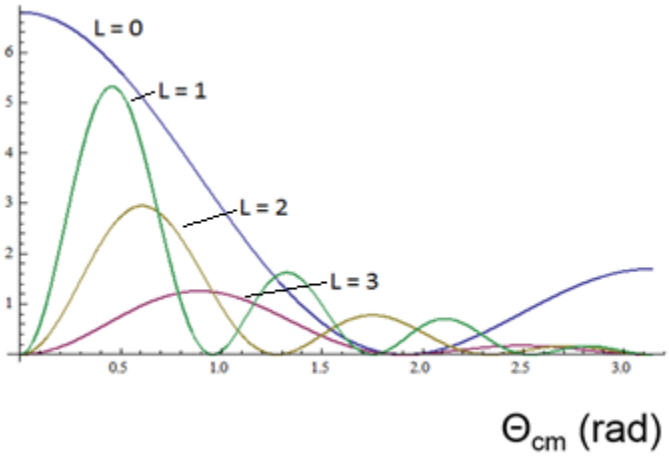

Figure 4.1 - ℓ - dependence of the differential cross-section using partial wave expansion [Sat83, Ber04]

If the parity of the target nucleus is known, Equation 4.2 along with Equation 4.1 allows for determination of the parity of the final nucleus and places a restriction on J_f.

III. Distorted-Wave Born Approximation

The distorted-wave Born approximation (DWBA) has been successfully applied to single-nucleon transfer reactions, as well as to elastic and inelastic reactions [Lee64]. The theory is based on the physical assumption that the elastic scattering potential dominates the interaction between nucleons and other reaction channels are weak and not strongly correlated [Sat83].

Mathematically, these other reactions can be described applying perturbations to the reaction elastic scattering channels. The derivation of the formal DWBA transition amplitude is worked through beautifully in many texts [Sat83, Fes92, Gle83, Ber04]. For the purpose of this dissertation, I've chosen to show a simplified derivation using a practical example which will provide the reader with a working knowledge of the theory.

Let us consider a proton stripping reaction (d,n) on the doubly magic nucleus ^{16}O. Now we wish to calculate the DWBA transition amplitude and ultimately the differential cross section ($d\sigma/d\Omega$) for this reaction. The entire reaction can be described by the Schrödinger equation,

$$(\mathcal{H} - E)\Psi = 0 \tag{4.6}$$

It is often useful to describe these processes diagrammatically as shown in Figure 4.2 though this approach has not been widely adopted [Fes92].

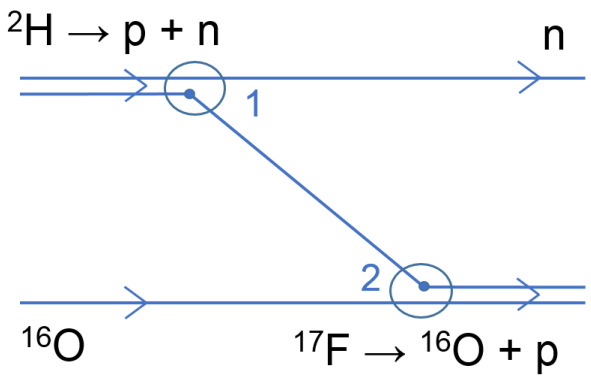

Figure 4.2 - Diagrammatical interpretation of the ^{16}O(d,n)^{17}F reaction.

Using this interpretation, we can break the system up into an entrance and exit channel. This is possible since the Hamiltonian can be represented in any partitions of the original nucleons [Sat83].

$$\begin{aligned}(E_\alpha - \mathcal{H}_\alpha - T_\alpha)\Psi^{(+)} &= V_\alpha\Psi^{(+)} \\ (E_\beta - \mathcal{H}_\beta - T_\beta)\Psi^{(+)} &= V_\beta\Psi^{(+)}\end{aligned} \tag{4.7}$$

The entrance channel consists of an incoming deuteron and ^{16}O target nucleus. The deuteron transfers a proton to the target leaving a neutron and the reaction product ^{17}F in the exit channel. Vertex 1 describes the core-proton (in the deuteron) and an outgoing transfer proton and neutron which can be described as an incoming plane wave and outgoing distorted wave with distorting potential U_α.

$$\langle e^{i\bar{K}_\alpha \cdot \bar{r}_\alpha} | U_\alpha | \Psi_\alpha^{(+)} \rangle \tag{4.8}$$

Vertex 2 contains an incoming proton and ^{16}O resulting in the ^{17}F nucleus (p + ^{16}O core) with interaction potential $V_\beta - U_\beta$.

$$\langle \phi_\beta^{(-)} | V_\beta - U_\beta | \Psi^{(+)} \rangle \tag{4.9}$$

Putting these components together, one can immediately write down the exact form of the transition matrix or T-matrix,

$$\mathcal{T}_{\beta\alpha} = \langle e^{i\bar{K}_\alpha \cdot \bar{r}_\alpha} | U_\alpha | \Psi^{(+)} \rangle + \langle \phi_\beta^{(-)} | V_\beta - U_\beta | \Psi^{(+)} \rangle \tag{4.10}$$

U_α is the primary interaction and $V_\beta - U_\beta$ is known as the *residual interaction*. At this point the system is still not computable since our expression contains the unknown wave function $\Psi^{(+)}$.

In DWBA theory, we make the assumption that $V_\alpha = 0$ reducing the many-body problem into a solvable one-body problem. This assumption allows us to make the following approximation,

$$\Psi^{(+)} \cong \Phi_\alpha \chi_\alpha^{(+)} \tag{4.11}$$

This is known as the *first-Born approximation*. Introducing this approximation into Equation 4.10 one arrives at a new transition matrix,

$$\mathcal{T} = \langle e^{i\bar{K}_\alpha \cdot \bar{r}_\alpha} | U_\alpha | \chi_\alpha^{(+)} \rangle + \langle \chi_\beta^{(-)} \Phi_\beta | V_\beta - U_\beta | \Phi_\alpha \chi_\alpha^{(+)} \rangle \tag{4.12}$$

We are only interested in the second term of Equation 4.12 for the (d,n) transfer reaction. Thus, we arrive at the scattering amplitude for the distorted-wave Born approximation.

$$\mathcal{T}_{\beta\alpha}^{DWBA} = \langle \chi_{\beta}^{(-)} \Phi_{\beta} | V_{\beta} - U_{\beta} | \Phi_{\alpha} \chi_{\alpha}^{(+)} \rangle \tag{4.13}$$

IV. Optical-Model Potential

An empirical complex optical model is used to generate the potential which must include all relevant nucleon-nucleon interactions with an empirically-fit potential which takes into account both scattering and absorptive effects. This potential, which consists of many components as discussed below, is empirically fit to experimental data from elastic scattering measurements. These fits are applied ether locally on a case-by-case basis or on a global basis. The latter give an overall representation of the mass region and is preferred. Early work on the optical model potential (OMP) is well documented by P.E. Hodgson [Hod94] and early global OMP fits for nucleon scattering were determined by F.D. Becchetti and G.W. Greenlees [Bec69].

The usual choice of the distorting potentials is of the form,

$$U(\vec{r}) = U_c(\vec{r}) + U_{OM}(\vec{r}) \tag{4.14}$$

where $U_c(\vec{r})$ is the Coulomb potential and $U_{OM}(\vec{r})$ is the complex optical model potential. For a charged sphere of radius r_c,

$$U_c(\vec{r}) = \begin{cases} \dfrac{Z_1 Z_2 e^2}{2r_c}\left(3 - \dfrac{r^2}{r_c^2}\right) & (r \leq r_c) \\ \dfrac{Z_1 Z_2 e^2}{r} & (r > r_c) \end{cases} \tag{4.15}$$

The optical model term $U_{OM}(\vec{r})$ consists of a volume term $U_v(r)$, surface term $W_s(r)$, and spin-orbit term $U_{so}(r)$. Each term is described by a real and imaginary component, where the latter accounts for nuclear reactions, i.e. absorptive processes:

$$U_{OM}(\vec{r}) = U_v(r) + U_s(r) + U_{so}(r) \tag{4.16}$$

The functional form of the volume potential takes the shape of a complex Woods-Saxon form factor shown graphically in Figure 4.2,

$$U(r) = -Vf(r, R, a) - iWf(r, R_w, a_w) \tag{4.17}$$

$$f(r, R, a) = \frac{1}{1 + e^{\frac{r-R}{a}}} \tag{4.18}$$

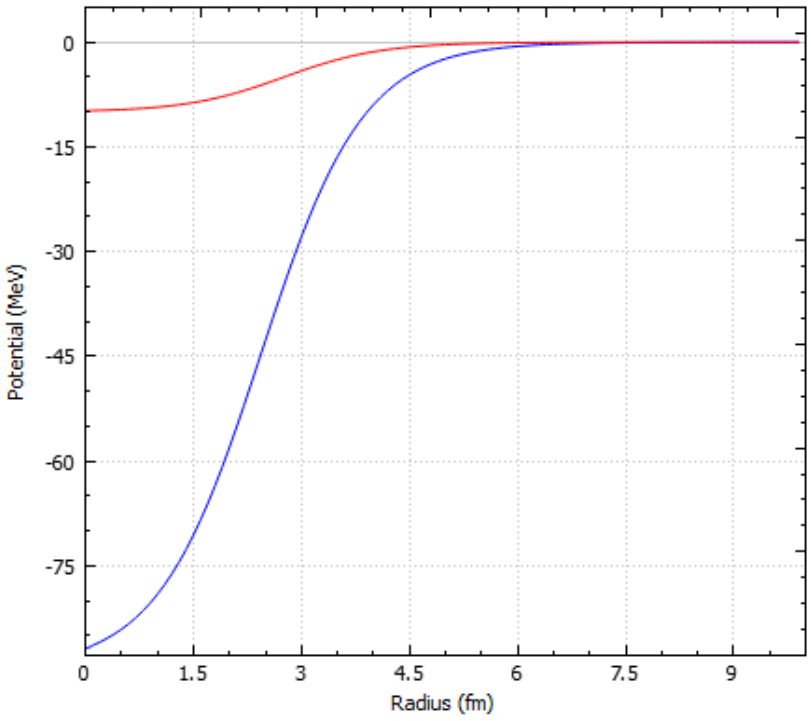

Figure 4.3 – Characteristic shape of a Woods-Saxon (WS) potential with two WS potentials shown at different well depths.

Where V, W represents the depth of the nuclear wells, R is related to the radius of the nucleus and a is the diffuseness of the potential. The surface term is usually taken as,

$$U_s(r) = -V'f(r, R', a') - iW'f(r, R'_w, a'_w) \tag{4.19}$$

$$f'(r, R', a') = 4ia\frac{d}{dr}f(r, R', a') \tag{4.20}$$

Where again V', W' represents the depth of the potential, R' is the radius parameter and, a' is the diffuseness of the potential. The spin-orbit term is taken as,

$$U_{so}(r) = \vec{s} \cdot \vec{l} \left(\frac{\hbar}{m_\pi c^2}\right)^2 V_{so} \frac{1}{r} \frac{d}{dr} f(r, R_{so}, a_{so}) \tag{4.21}$$

Where $\vec{s}$ is the spin operator, $\vec{l}$ is the orbital angular momentum vector, and m_π is the mass of the pion responsible for the force.

V. Spectroscopic Factors and Strengths

The DWBA transition amplitude assumes the reaction progresses to a single final particle state. In reality, this is complicated by residual interactions which may lead to configuration mixing of states with the same angular momentum and parity.

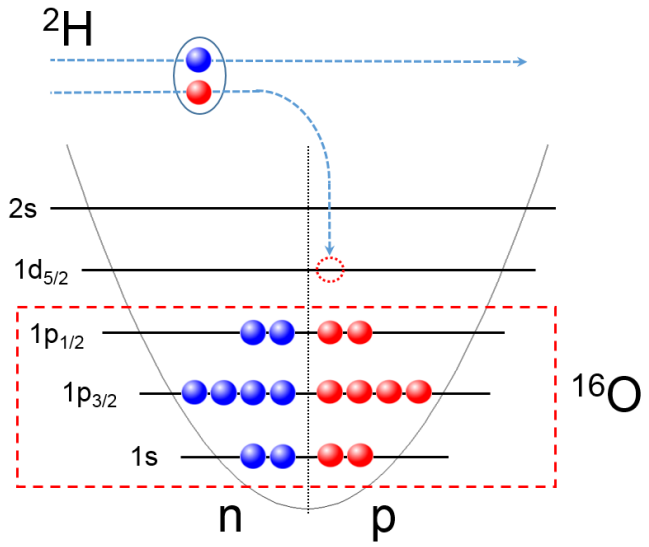

Figure 4.4 - Graphical level structure interpretation of ^{16}O(d,n)^{17}F.

For example if we go back to the ^{16}O(d,n)^{17}F reaction, we can predict the final spin and parity form the single-particle model (also known as the extreme shell model) which assumes the final nucleus ^{17}F consists of an even-even ^{16}O core plus an unpaired valence proton, as graphically

represented in Figure 4.4. The model predicts for ground-state transfer the proton will occupy the 1d5/2 orbital leading to overall spin/parity of $J^{\pi} = 5/2^{+}$ with $\ell = 2$. Deviations from a pure single-particle state can then be described by the *spectroscopic factor SF* as defined,

$$\left(\frac{d\sigma}{d\Omega}\right)_{exp} = \frac{2J_f + 1}{2J_i + 1}(SF)_{ij}\left(\frac{d\sigma}{d\Omega}\right)_{DWBA} \tag{4.22}$$

If the final spin is unknown, the spectroscopic factor can be written as the *spectroscopic strength* $\mathcal{S}$ which absorbs the initial and final state angular momentum terms as the latter may be unknown:

$$\mathcal{S} = \frac{2J_f + 1}{2J_i + 1}\,SF \tag{4.23}$$

and hence,

$$\left(\frac{d\sigma}{d\Omega}\right)_{exp} = \mathcal{S}\left(\frac{d\sigma}{d\Omega}\right)_{DWBA} \tag{4.24}$$

Another example is the ^{31}P(d,n)^{32}S reaction at E_d = 25 MeV shown in Figure 4.5 from [Ber04]. DWBA calculations are shown as the black curves for the indicated ℓ value.

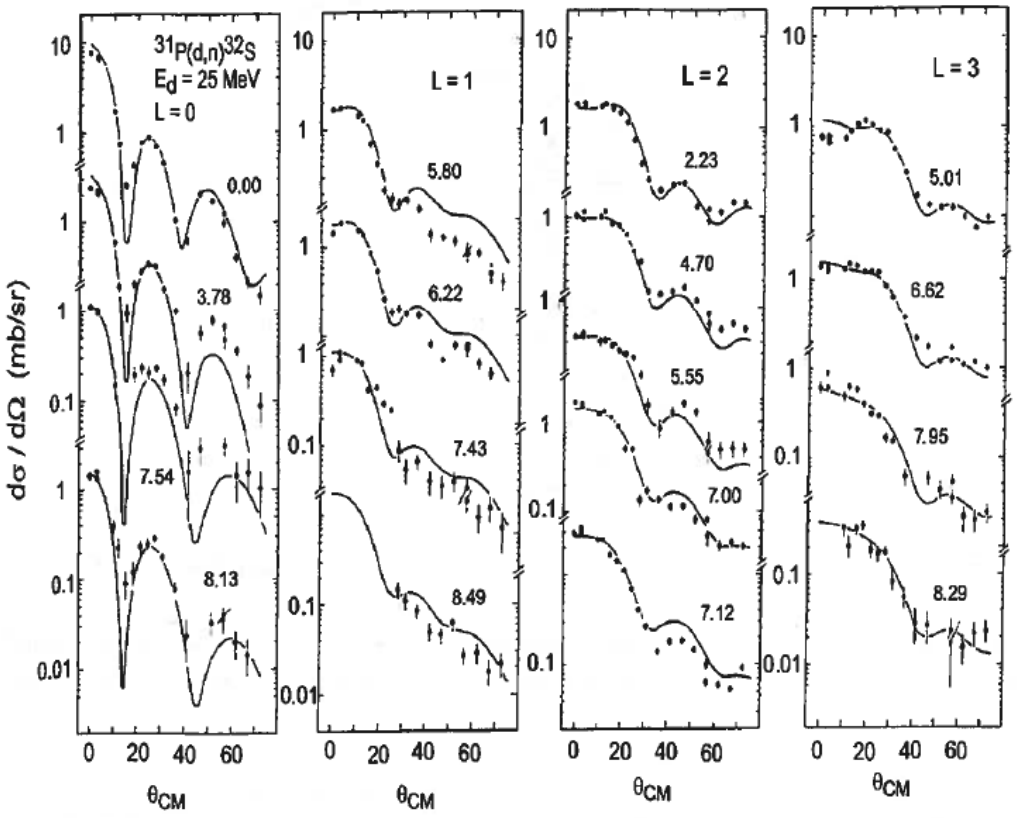

Figure 4.5 – Differential cross section measurements of $^{31}P(d,n)^{32}S$ reaction from [Ber04].

The DWBA calculations show good agreement in describing the shape of the angular distributions. These measurements were conducted using n-ToF which as shown in Figure 4.5 can be limited to forward angles, excluding the back angles where compound-nuclear contributions might be observed. Since neutrons can easily 'evaporate' from a nucleus that has absorbed a deuteron [i.e. as possible with (d,n) reactions], these neutrons can contribute to the measured differential cross section and be falsely identified as neutrons from the direct reaction [Ber04]. The increase in cross sections effects the extracted spectroscopic factors and thus it is important that the compound-nuclear contributions be removed. Figure 4.5 also shows that in order determine the transferred angular momentum of a (d,n) reaction at similar energies, an angular resolution of < 5-7 degrees is required.

Chapter 5

Detector Characterization

I. Detector Characterization Measurements

1. Recoil proton and deuteron response

The light-response measurements for EJ-315, EJ-315H, and EJ-315M scintillators were conducted at the University of Notre Dame Institute for Structure and Nuclear Astrophysics (ISNAP). The 9 MV FN tandem Van de Graaff accelerator was used to accelerate an E_d = 15 MeV primary deuteron beam with approximately 20 nA of current on target. The beam was bunched with 800 ns between bunches (1 in 8 pulse selection from a primary 10 MHz pulsed beam). Neutrons were produced by stopping the primary beam in an enriched thick ^{11}B target. This effectively produced a broad 'white' neutron source. Information regarding the target can be found in [Law13]. The target was positioned in the beam pipe located within a thick concrete wall dividing two target halls (Figure 5.1). This was done to limit the unwanted neutron flux to the target halls and provide some collimation to the secondary neutron beam.

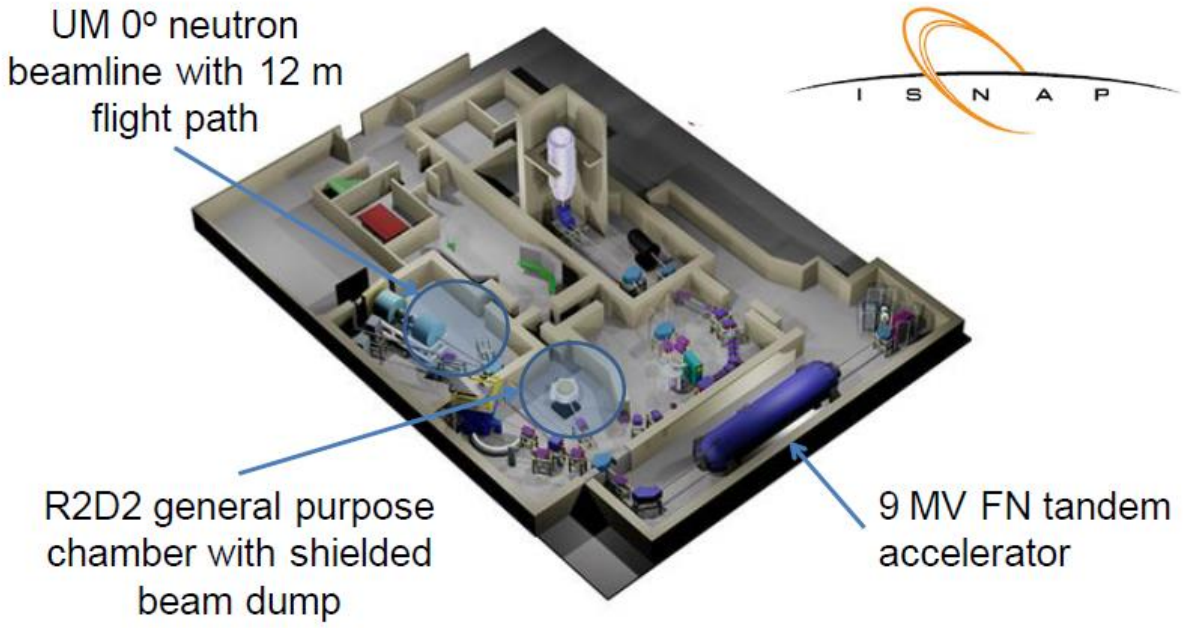

Figure 5.1 - Layout of the UND Institute for Structure and Nuclear Astrophysics laboratory.

Further collimation was provided using borated-polyethylene blocks and pellets. Each detector was located 13.25 m from the target to the front face of the detector, which was mounted to an aluminum fixture with electronically-controlled translator via a USB 2.0 link constructed by the author. This permitted rapid neutron flux profile measurements to optimize placement of the detector for the response measurements. The detector stand with translator is shown in Figure 5.2 and a flux profile map is shown in Figure 5.3.

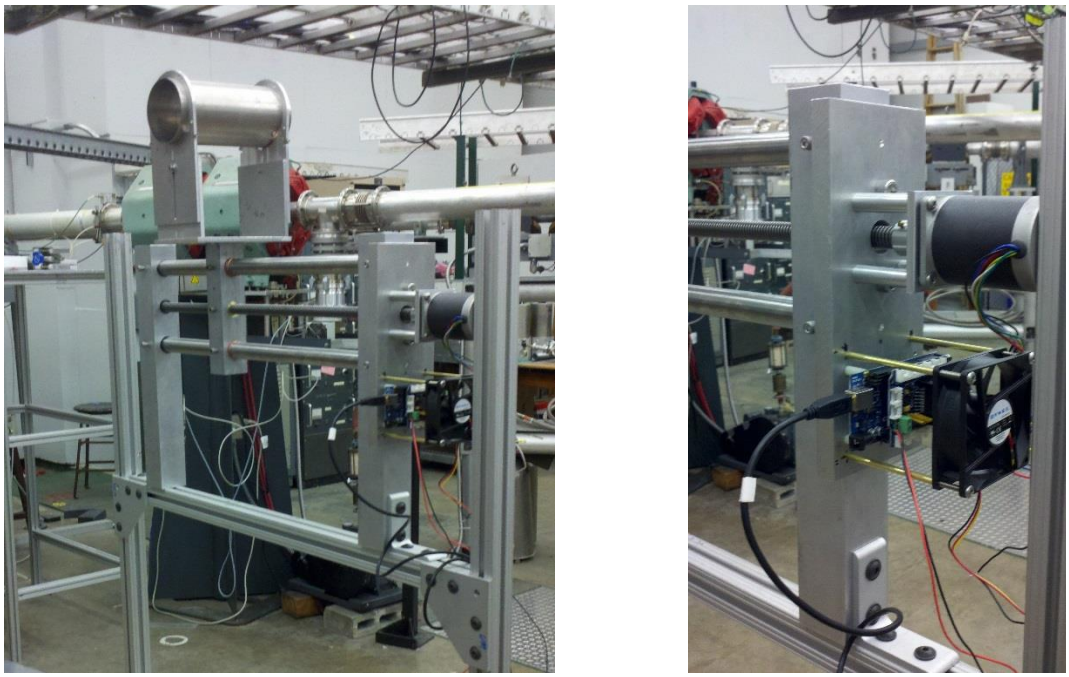

Figure 5.2 - Detector stand with translator (left). Close up of USB based Arduino® control system and stepper motor (right).

Digitized scintillation pulses were acquired at 2 GS/s at 10-bit pulse-height resolution with a 996 ns acquisition window using the CAEN V1751 waveform digitizer. In order to minimize electronic noise and signal broadening (from time dispersion and noise in the cables), which negatively affects particle discrimination capability and timing resolution, the digitizer was located in close proximity to the detector with 8 ns of RG56 coaxial cabling. The coaxial cable and its length was carefully selected out of a batch of cables based on the quality of the ^{252}Cf neutron/gamma discrimination and ^{22}Na gamma-gamma coincidence timing measurements. This was done in an attempt to optimize proton-deuteron separation and provide optimal beam timing for n-ToF. A fast signal from the beam buncher was digitized at 2 GS/s in coincidence with the neutron beam pulse for the n-ToF measurement.

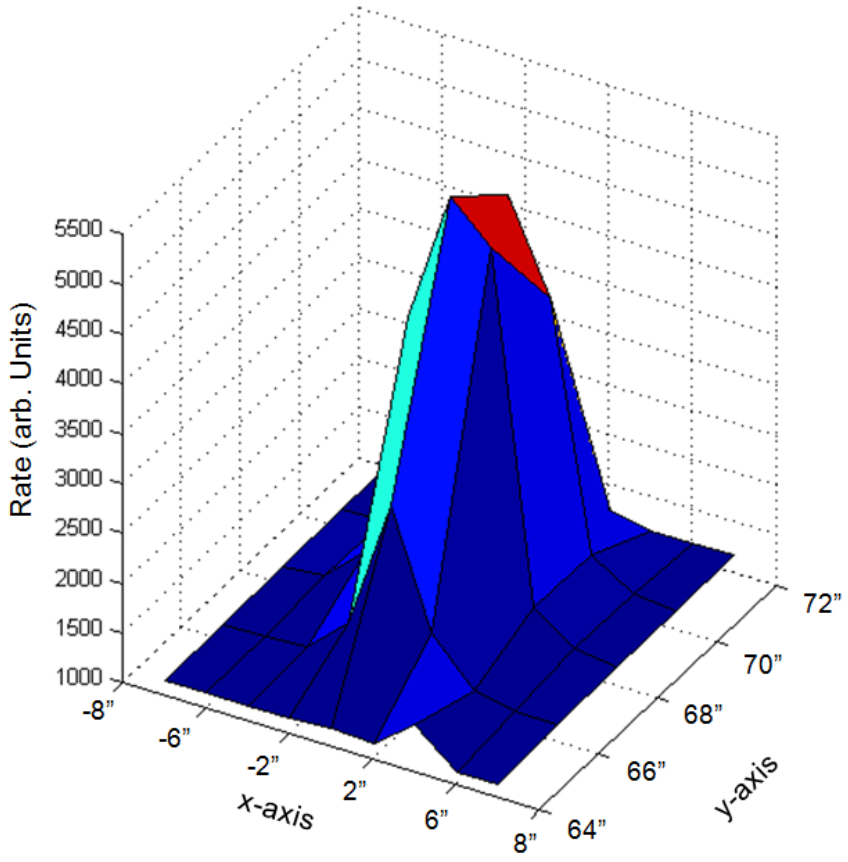

Figure 5.3 - Flux distribution map of the neutron production beam at the detector position measured using the translator shown in Fig. 5.2.

2. Recoil electron response

The electron response for each detector was determined by Compton scattering using standard long-lived gamma-ray sources. The recoil electron energy was then extracted from the Compton edge of the Compton continuum. Standard laboratory sealed ‘button’ sources were used to produce low-energy recoil electrons, $E_\gamma < 2$ MeV: ^{60}Co, ^{22}Na, ^{137}Cs, and ^{133}Ba. Short-lived ^{24}Na and ^{16}N sources were made via neutron irradiation and used for high-energy recoil electrons, $E_\gamma >$ 2 MeV.

The ^{24}Na source was produced by ^{23}Na(n,γ) neutron capture of an aqueous solution of 50% NaOH in a sealed plastic container, placed in a large container of water, located near the in-wall ^{11}B target. The neutron flux moderated by the water proved to be adequate to produce a weak but

usable ^{24}Na source. The ^{16}N production was a bit more challenging due to its short half-life, $T_{1/2}$ = 7.13 sec. Two methods were used for production: $^{13}C(\alpha,n)^{16}O^*$ and $^{16}O(n,p)^{16}N$ reactions.

Previously, $^{16}O(n,p)^{16}N$ production was studied at the University of Michigan Neutron Science Laboratory (NSL). The NSL facility has a Thermal Scientific Model DL711 deuterium-tritium (DT) fusion neutron generator capable of 14.1 MeV neutron yield of > 10^{10} neutrons/s. The facility is equipped with a pneumatic tube (p-tube) system [Pie15] for quickly transporting samples from the irradiation area to various HPGe γ detectors and general-purpose stations with transit time < 300 ms [Pie15]. This permits measurements of short half life products such as ^{16}N, $T_{1/2}$ = 7.13 s. For possible oxygen targets, comparison was made between a polycarbonate pellet and compressed $LiCO_3$ powder. Liquid ^{16}O sources such as water were not used due to hazards and possible contamination issues of placing liquid samples in the pneumatic tube system. It was found in the HPGe γ-ray measurements with both samples, that both polycarbonate and $LiCO_3$ produced a 'clean' spectrum near the 6.128 MeV γ-ray region (Figure 5.4). The higher atomic % oxygen in $LiCO_3$ (64.96% vs. ~19% for polycarbonate) and overall density led to the decision to use compressed $LiCO_3$ since a higher intensity source could be produced. The $LiCO_3$ was irradiated for 25 s followed by a 95 s counting time interval at a low background counting station. These timing intervals correspond to > 95% saturation for $^{16}O(n,p)^{16}N$ reaction during irradiation and < 0.1% residual activity for the given count time interval. This process was repeated automatically using in-house p-tube control software till adequate counting statistics were reached.

At UND, ~15 nA 7.5 MeV ^{4}He beam for the $^{13}C(\alpha,n)^{16}O^*$ reaction was accelerated using the FN tandem Van de Graaff accelerator. The ^{4}He beam bombarded a ~200 μg/cm^2 enriched ^{13}C target. The beam was then dumped into the center of a well-shielded 76 cm x 76 cm x 76 cm lead cave. Excited $^{16}O^*$ from the $^{13}C(\alpha,n)^{16}O^*$ reaction then provided an adequate source of 6.128 MeV gammas for calibration with high-energy recoil electrons.

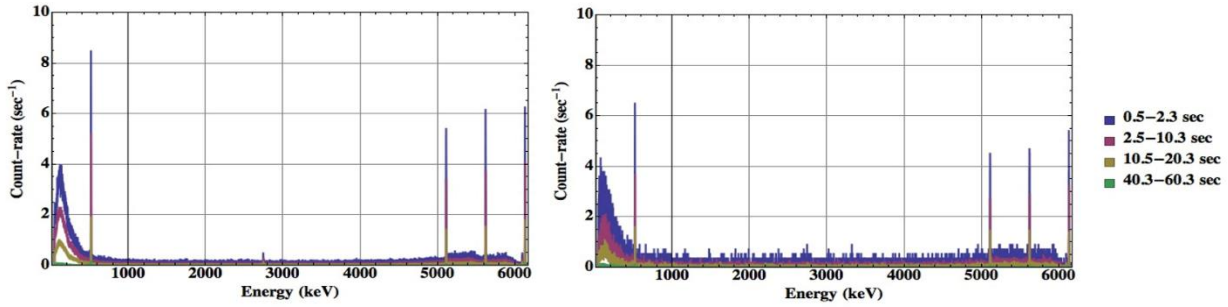

Figure 5.4 – Time-resolved HPGe γ-spectra from 14.1 MeV neutron-irradiated compressed $LiCO_3$ powder (left) and polycarbonate pellet (right).

3. Detector energy resolution

Detector energy resolution was determined using two techniques. Below 1 MeVee, Compton scattering was used at UM to produce quasi-monoenergic recoil electrons by γ-coincidence tagging using a 5 cm dia. x 5 cm NaI(Tl) detector. Intense sources of collimated gamma rays were supplied using ~1 mCi ^{137}Cs and ~100 μCi ^{22}Na sources in a lead pig (Figure 5.5). 1.0 cm diameter lead collimators in front of the sources and on the face of the NaI(Tl) detector constrained the angular acceptance of the of γ-rays.

Resolution was also determined from the ToF data using the Compton-edge width method described by V. Bildstein [Bil13]. Information regarding this procedure is described in §6.1.

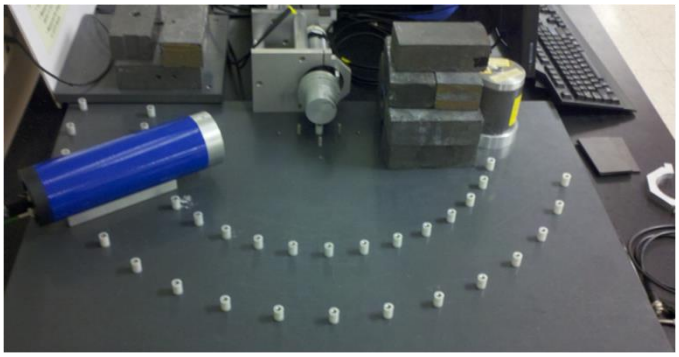

Figure 5.5 - The UM Compton scatter setup for determination of detector energy resolution. A 1 mCi ^{137}Cs source is shown in the lead pig on the right.

II. Processing of Digitized Waveforms

I will now outline the processing of the digitized detector signals using DSP.

1. Event reconstruction

Once the system is triggered, an event is constructed and stored to the onboard memory of the digitizer as a collection of 32-bits known as a Dword. These events are stored until a buffer threshold is met. The contents are transferred to the acquisition computer, and then stored in binary files. The format of a signal event is shown in Figure 5.6. Each event contains a 4 line header with 4 character event start code 1010 starting in bit 31 followed by the event size. The subsequent lines contain the channel mask, event counter, and trigger time tag. The active channels are recorded in the channel mask where 1 = on and 0 = off and each bit corresponds to a channel number (i.e. channel 2 is bit 2, …).

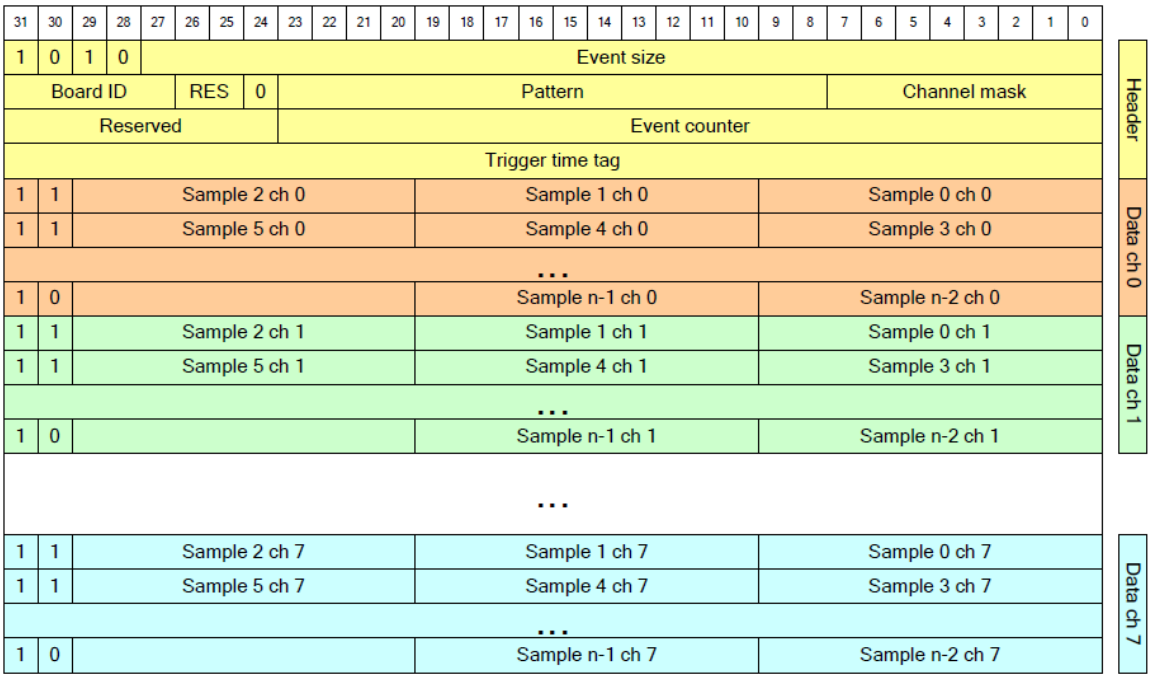

Figure 5.6 - The 32-bit structure of a digitized event (from CAEN Technologies).

2. Digital signal processing and DPSD

In order to extract useful quantities from the digitized detector waveforms, post processing is required. For processing an analysis package was written in C++ with routines specific for analysis of digital waveforms of fast scintillation pulses. The steps used in DSP share the same basic process flow diagram (PFD) components but are done in software rather than analog hardware. For scintillation pulses the PFD is shown in Figure 5.7.

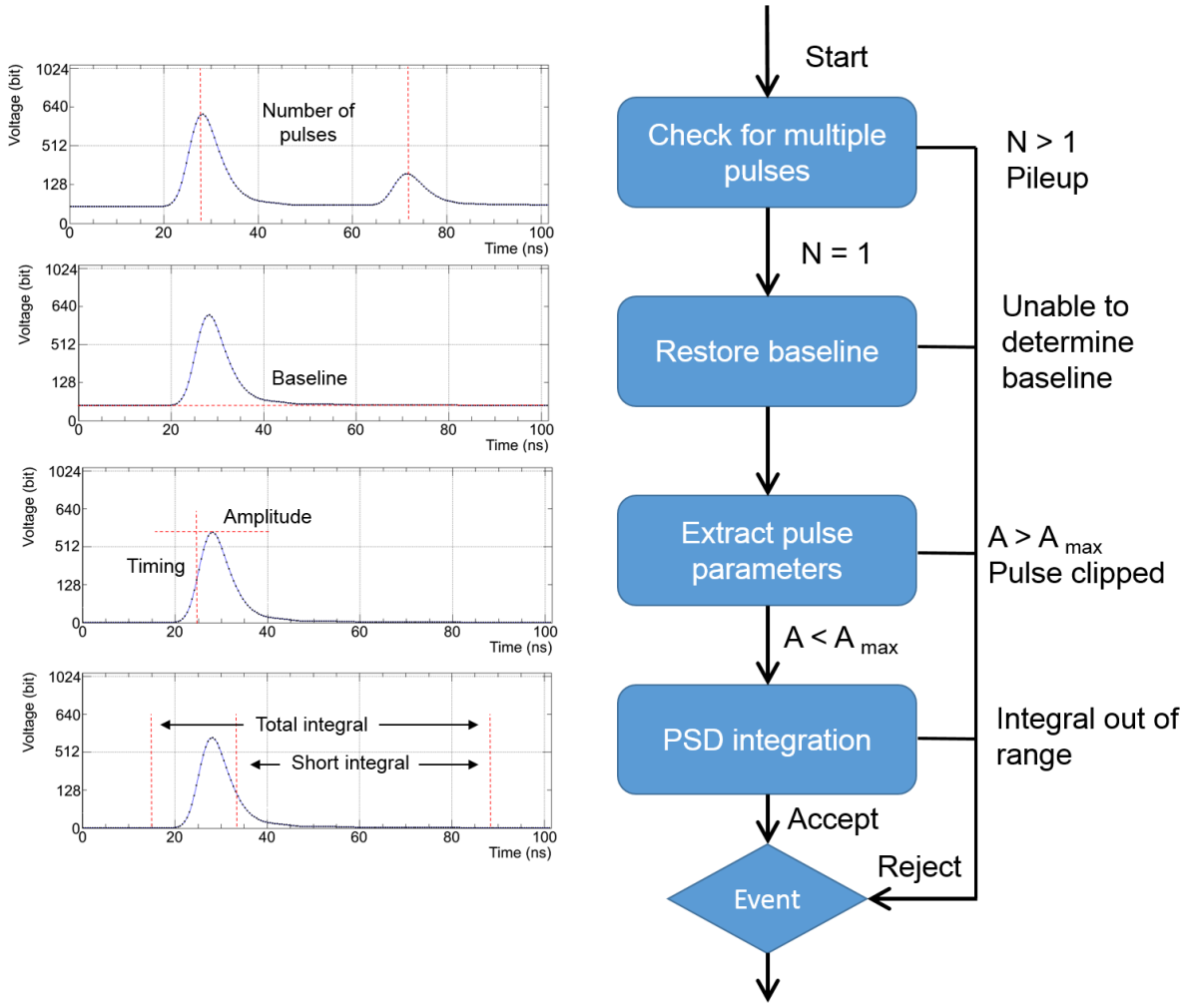

Figure 5.7 - Process flow diagram (PFD) for pulse processing

Scintillation pulses are first sent to a peak-finding routine which is used to determine if there are multiple peaks in a given digitizer time window. This is done by calculating the

numerical derivative of the waveform, calculating the standard deviation of the baseline, and checking for sections of the waveform which go above a user-defined threshold (typically 5σ). If two peaks occur within the integration range of each other in the region, the waveform is rejected. No attempt is made to extract the individual pulses from these events because of their infrequency (typically < 0.1 % of events). Next the waveform goes through a baseline-correction routine which determines the baseline by averaging a flat section of the waveform for a given interval. Typically this was set to 50 ns (50 samples at 1 GS/s). Next the amplitude and digital constant-fraction timing (DCFD) is determined. If the amplitude > (dynamic range – baseline), the waveform is rejected due to pulse clipping. Finally, a pulse-shape discrimination routine is used for identification of recoil particle type. Recoil-particle identification and subsequent discrimination is accomplished using the charge-integration technique as described in §3.7. A comparison is made of long and short PMT anode pulse integrals.

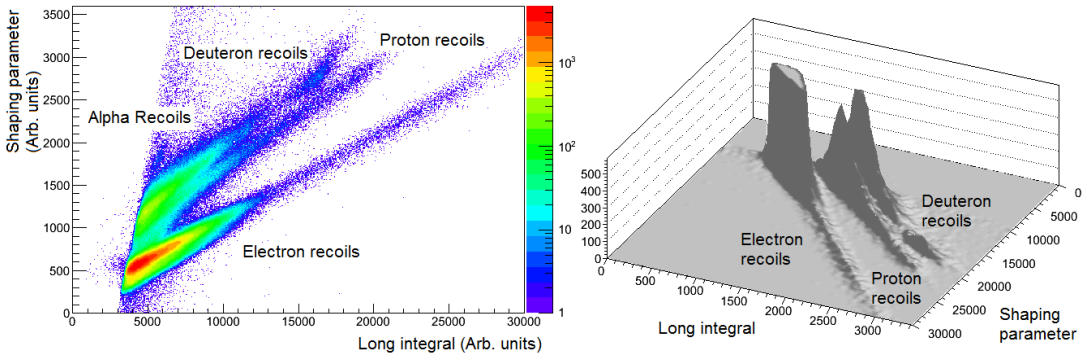

Figure 5.8 - DPSD of α/d/p/e discrimination in the 5.08 cm dia. x 5.08 cm cylindrical EJ-315 deuterated-liquid scintillation detector

These integrals are a measure of the total light yield (i.e. prompt + delayed fluorescence) and the delayed fluorescence contribution of a recoil-particle interaction, respectively. In DSP, this is made by computing the numerical integral, in this case using a trapezoidal method, over the entire pulse and the corresponding short integral from a user-defined offset (typically 25 ns from 50% amplitude of the leading edge) to the end of the pulse. The choice of the offset parameter is made by maximizing the Figure-of-Merit (FOM) for recoil electron-deuteron-proton separation.

Good n/γ separation is observed down to 100 keVee. A sample of the pulse-analysis code, known as the 'scanner code', is given in Appendix E.

III. Simulation of Detector Efficiency

The short-range nuclear interaction of the neutron yields a low interaction probability and permits it to not only escape the target but also the target chamber and into the surrounding experimental setup. Unlike charged-particle detection, care must be taken inside *and* outside of the target chamber and everything in the experimental setup as it all serves as a potential scattering source, including the surrounding air! To complicate matters, neutron detection efficiency for liquid scintillators, being recoil-particle spectrometers, is threshold dependent. This becomes a daunting computational problem which can only be solved by Monte Carlo based neutron-transport codes such as MCNPX [MCNPX]. An extension to MCNPX known as MCNPX-PoliMi [Poz03] provides a convenient event-by-event output file which can be used to determine contributions from scattering sources, detector efficiency, and cross talk between elements.

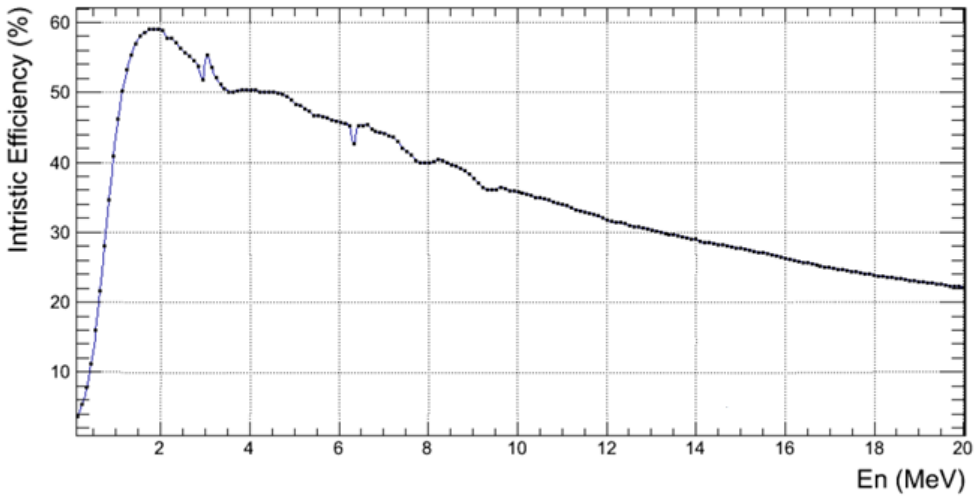

Figure 5.9 – Simulated efficiency of one of the 4x6 EJ-315 detectors with a threshold of 50 keVee.

Each of the experimental setups in §6.1-6.4 were simulated with MCNPX-PoliMi [Poz03] to simulate detection efficiency, cross talk, and contributions from scattering sources in the experimental setups.

IV. Experiments

Analysis of the digitized waveforms was processed off-line using an analysis package written for analysis and discrimination of fast scintillation pulses (see §5.6 for details on pulse analysis). The number of pulses for each scintillation waveform is determined using a peak-identification routine. If two pulses occurred within the integration limits of ether pulse, they were both vetoed. Otherwise, the timing, pulse-height, total charge, and Digital Pulse Shape Discrimination (DPSD) parameters were determined. Timing was calculated using a constant-fraction discrimination method where linear interpolation was used between points on the leading edge. Because of the high digitization rate, enough points are sampled on the slowly varying region of the leading edge (~ 6 samples between 10% & 90% amplitude) to justify linear interpolation versus more elegant functional fitting methods [Pau14]. Neutron ToF and the subsequent kinetic energy (including relativistic corrections) was determined by the timing difference between coincident scintillation-pulse and beam-buncher signals relative to the gamma-ray peak. Corrections for the flight time of the gamma ray also were taken into account. The intrinsic coincident timing resolution of the CAEN V1751 digitizer was measured to be < 50 ps using a Phillips fast pulser which mimics scintillation pulses for the analysis package described above. The analysis package is included in the discussion of intrinsic timing of the system because the timing in discrete digitized data is a direct result of the quality of interpolation between sampled points. A typical ToF spectrum for both gamma ray and neutrons is shown in Figure 5.10. The large peak toward the left of plot is the gamma-ray peak from gammas produced at the target position. Subsequent peaks are due to the beam striking various tuning elements in the beam line before reaching the target. The large 'hump' after the gamma-ray peak is the neutrons primarily from reactions in the target. The FWHM of the gamma-ray peak shown is 1.5 ns. Since the < 50 ps intrinsic coincident timing resolution of the digitizer and analysis software is much less than the timing resolution of the experimental setup, we can conclude that the timing resolution is dominated by the width of the beam bunch rather than the electronics or software DSP.

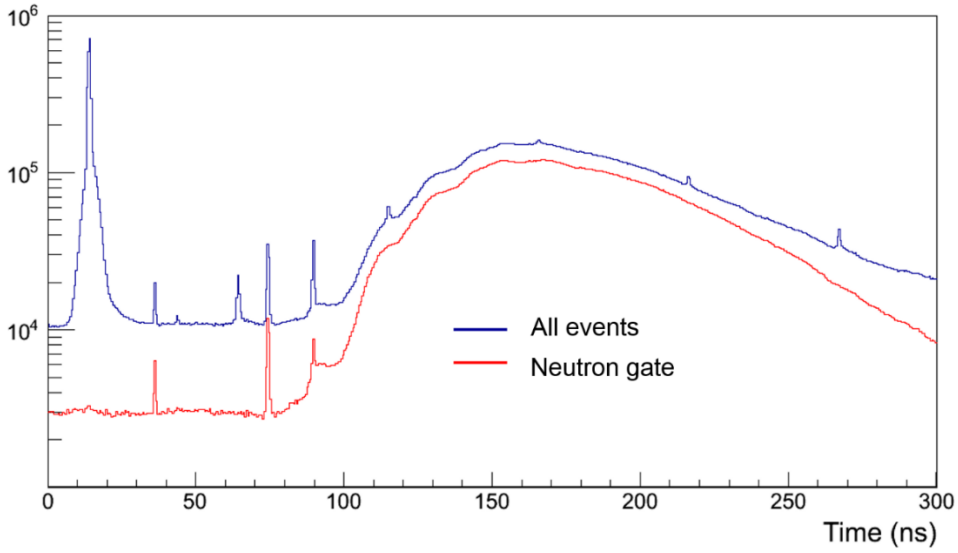

Figure 5.10 - Typical n-ToF plot

1. Pulse-shape discrimination (PSD)

DPSD is evaluated using the charge-integration method. The quality of discrimination of the charge-integration method is strongly dependent on the offset parameter. Optimization of the offset parameter is made by maximizing the FOM over a range of offset parameters. The optimal offset parameter for EJ-315 and EJ-315M was found to be 18 ns which is in good agreement with the simplified scintillation model in §3.5. Figure 5.11 shows 5000 pulses averaged and gated on electron and deuteron recoils. The resulting DPSD data for the 2x2 detectors were slightly better than those for the large 5x5 EJ-315M detector, while the DPSD spectra for the existing 4x6 EJ-315 detectors were somewhat worse. In several of these tests the dynode signal rather than the anode signal was utilized for digitization, with the PMT HV adjusted slightly downward from its specified HV to give improved DPSD. The exact HV needed varies between PMTs and the particular PMT base used, and is determined empirically in-beam at the moment. The use of the dynode appears to yield a signal with a better signal to noise ratio then the anode signal as it apparently bypasses noise added in the later stages of the PMT. The lower PMT voltage lengthens both the pulse rise and fall times which allows for a greater number of digitized points (using 1 ns/point) for the pulse.

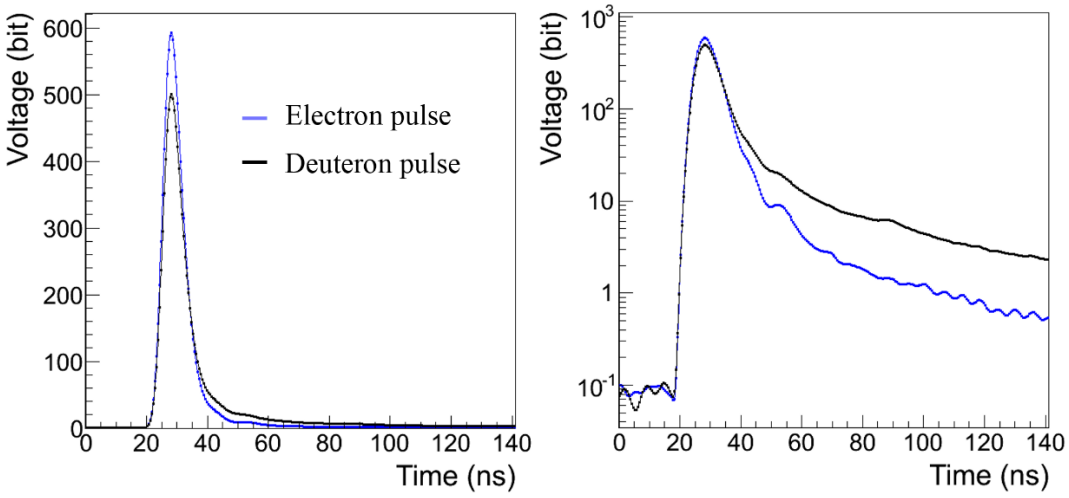

Figure 5.11 - 5000 averaged recoil deuteron and electron pulses (linear scale left; log scale right)

As the neutron energy increases the d(n,nnp) breakup cross section in the scintillator increases thus producing a higher proton contribution [Pau75]. Inclusion of protons from breakup (Figure 5.8) can lead to a masking of recoil deuteron peaks for low statistics data [Feb13]. Figure 5.12 shows a histogram of total integral to short integral (also known as shaping parameter) at E_n = 28 MeV. The contamination of protons from deuteron breakup in the recoil deuteron spectrum is clearly visible.

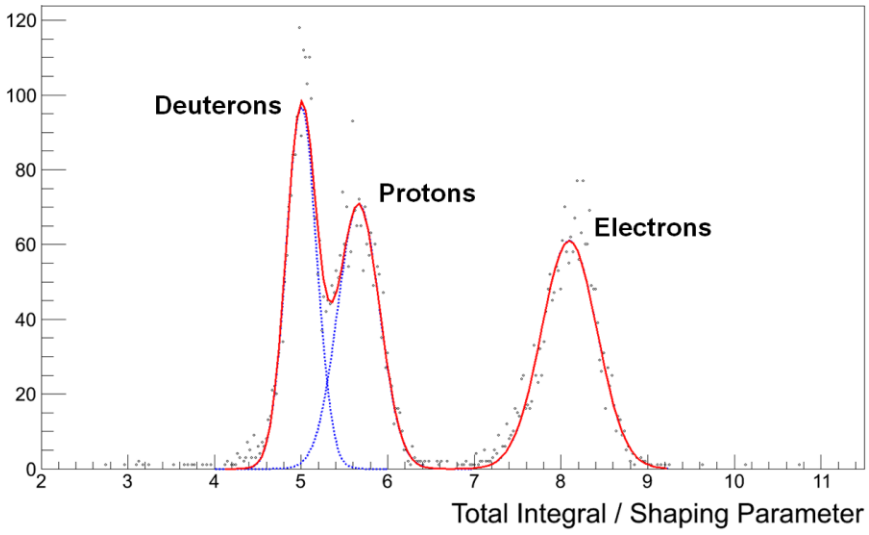

Figure 5.12 - DPSD spectrum in the region near E_n = 28 MeV showing the contributions of recoil electrons, protons, and deuterons

2. Detector energy resolution

In theory, a measure of the detector energy resolution from a light-response continuum spectrum cannot be determined without the intrinsic detector resolution known as the resolution function is needed for accurate placement of the response edge. It turns out this circular argument can be mediated by providing an initial guess of the edge, then extraction of the resolution function which in turn determines a new placement of the response edge, and then re-extraction of the detector resolution. This process can be repeated till it converges. Another possible method is to use γ-coincidence tagged recoil electrons from Compton scattering where the resolution can be extracted from the recoil-electron peak. The detector resolution function for high-energy recoils, is $dL/L \approx constant$, thus accurate edge placement is not as critical.

The UM-DSA detector resolutions were determined using two techniques; Compton scattered, γ-coincidence tagged electrons at low energies, and direct extraction from the measured spectral response in the light-energy linear regime. Below 1 MeVee, Compton scattering was used to produce quasi-mono-energetic recoil electrons by γ-coincidence tagging using a 5 cm dia. x 5 cm NaI(Tl) detector. The recoil electron peak was identified from each spectrum, and the full-width at half maximum (FWHM) was extracted. The edge width method described by V. Bildstein [Bil13] was used for direct extraction from the light-response continuum of nToF sliced spectra in the linear regime. In this method, resolution (in %) is defined as

$$R = 100 \left| \frac{C_{12.5} - C_{87.5}}{C_{50}} \right| \tag{5.1}$$

where C_x is the channel number corresponding to the location of the xth percent of the maximum edge height. It was found that a half-Gaussian fit each n-ToF sliced light-response spectrum adequately and could be used for extraction of the channel number for each edge C_x. Results from both methods for the EJ-315 5x5 large scintillator are shown in Figure 5.13.

$$\frac{\Delta L}{L} = \sqrt{a^2 + \frac{\beta^2}{L} + \frac{\gamma^2}{L^2}} \tag{5.2}$$

The resolution function parameters (Equation 5.2) for each detector were then fit using a chi-squared fitting routine. The resulting resolution constants α, β, and γ are listed in Table 5.1.

Table 5.1 – Detector resolution constants as fit to Equation 5.2

Scintillator	ID	α	β	γ
EJ-315M	5x5	0.0969	0.07132	0.005803
EJ-315M	4x6	0.1351	0.05287	0.006608
EJ-315	4x6	0.1353	0.08576	0.008381
EJ-315	2x2	0.08235	0.05155	0.001054
EJ-315H	2x2	0.07452	0.1280	0.003822

As mentioned above, for neutron measurements above ~5 MeV the detector resolution is dominated by the α term denoted in Equation 5.2. Table 5.1 shows a decrease in α with detector size, with the exception of the 4x6 detectors. This discrepancy is most likely due to poor light collection from the mismatch of the 7.62 cm dia. PMT coupled to a 10.16 cm dia. cell. There also appears to be no major difference between EJ-315 and EJ-315M in terms of detector resolution. This suggests that the improvement of DPSD for EJ-315M over EJ-315 is due to an increase in the ratio of delayed fluorescence to total fluorescence rather than on an overall increase of total scintillation photons per energy deposited.

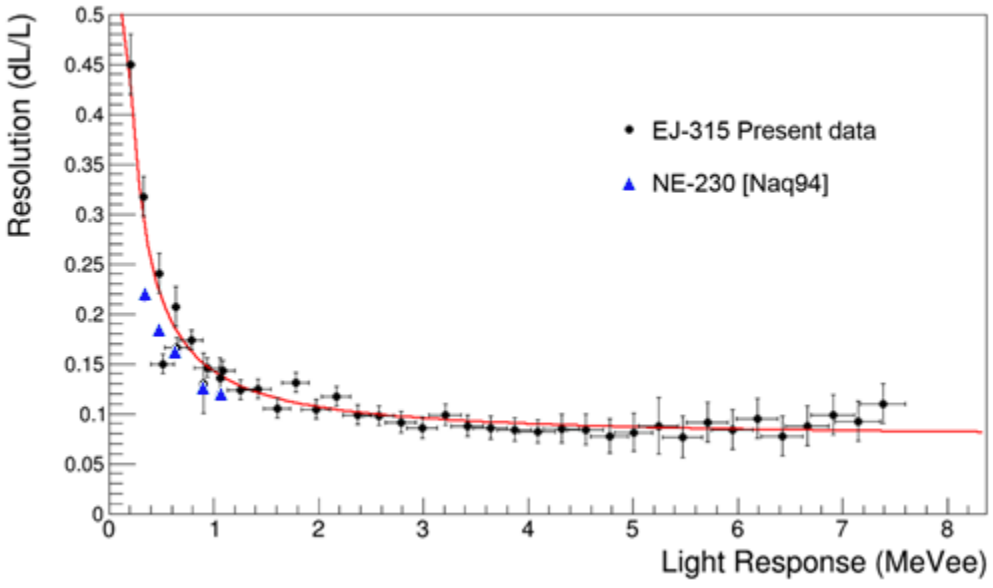

Figure 5.13 - Detector resolution of EJ-315 2x2 compared to data for NE-230 [Naq94]

Proper placement of the light response edge can then be described as the location along the edge at a fraction of recoil peak height, $f = B/A$. With detector resolution determined, proper placement of the light-response continuum edge can be determined using Monte Carlo simulation. Now again we run into the same issue that the proper placement from a Monte Carlo simulation depends on the light-response function which depends on the resolution and thus proper placement. Since it is known that the light-response functions tend to become linear above E ~5 MeV, we can use the same approximation and iterative procedure as before. Figure 5.14 shows a MC response spectra at E_n = 15 MeV with and without resolution.

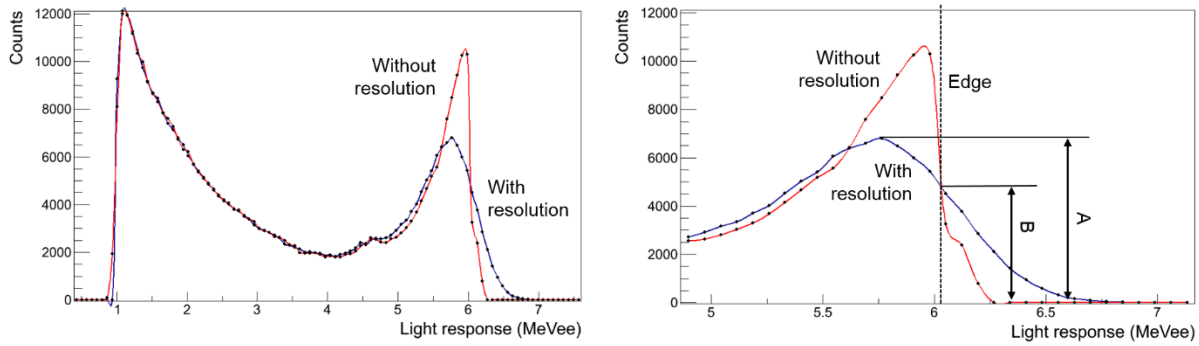

Figure 5.14 - E_n = 15 MeV recoil-deuteron light-response MC spectra with and without detector resolution.

3. Light response

Pulse-height response for a given incident neutron energy was determined by applying timing cuts associated with the corresponding energy to the ToF distributions and projecting the gated events. A further cut was made on DPSD to extract the recoil particle of interest (i.e proton, deuteron). In the case of the deuterated scintillators, as noted there is a significant contribution from protons which are a result of the d(n,nnp) deuteron breakup reaction in the scintillator for incident neutron energies above the reaction threshold 2.22 MeV. There also is a small amount of hydrogen which is in the EJ-315/EJ-315M formulation but contribution from this alone is minimal, < 5 %. To obtain the proper response of deuteron recoils without distortions from recoil protons (which due to their higher light response can extend the leading edge of the deuteron response), good recoil particle discrimination is necessary.

Due to uncertainties in reporting the placement of the edge for a Compton or elastic scattering response, a symmetric approach was adopted for this work. The edge for a continuum-based detector response, such as that from Compton or elastic scatter, is the result of the differential cross section for that interaction convoluted with the detector response, which can be modeled as a Gaussian blur. This leads to the overall Gaussian-like shape of the response edge. Using this, a Gaussian fit was systematically applied to each response edge. The response value was determined by taking the position at the specific fraction of the leading edge amplitude for the deuteron response. This fraction was determined by determining the crossing of simulation spectra with and without resolution. For the electron response, the Compton edge was taken to be the intersection of the simulation's Compton continuum with and without resolution.

The response data was then fitted to the functional form given below. This functional form accounts for both the non-linear regime at lower energies and linear regime at higher recoil particle energies and goes to zero at $E_{p,d} = 0$.

$$\mathcal{L}(E_{p,d}) = aE_{p,d} - b(1 - e^{-cE_{p,d}}) \tag{5.3}$$

Measured light-response curves are shown in Figure 5.15 for EJ-315 and in Figure 5.16 for EJ-315M. The parameterized fits for recoil protons and deuterons are shown in Table 5.2. For both EJ-315 and EJ-315M no detector size effects were observed with EJ-315 and EJ-315M which showed similar light-response curves.

Table 5.2 – Fit to experimental response data for each detector

		Recoil-deuteron light-response parameters		
Scintillator	ID	a	b	c
EJ-315	2x2	0.57 ± 0.04	1.87 ± 0.61	0.267 ± 0.09
EJ-315	4x6	0.56 ± 0.03	2.64 ± 0.22	0.16 ± 8E-3
EJ-315M	4x6	0.52 ± 0.03	2.43 ± 0.55	0.19 ± 0.04
EJ-315M	5x5	0.56 ± 0.03	2.64 ± 0.51	0.20 ± 0.04

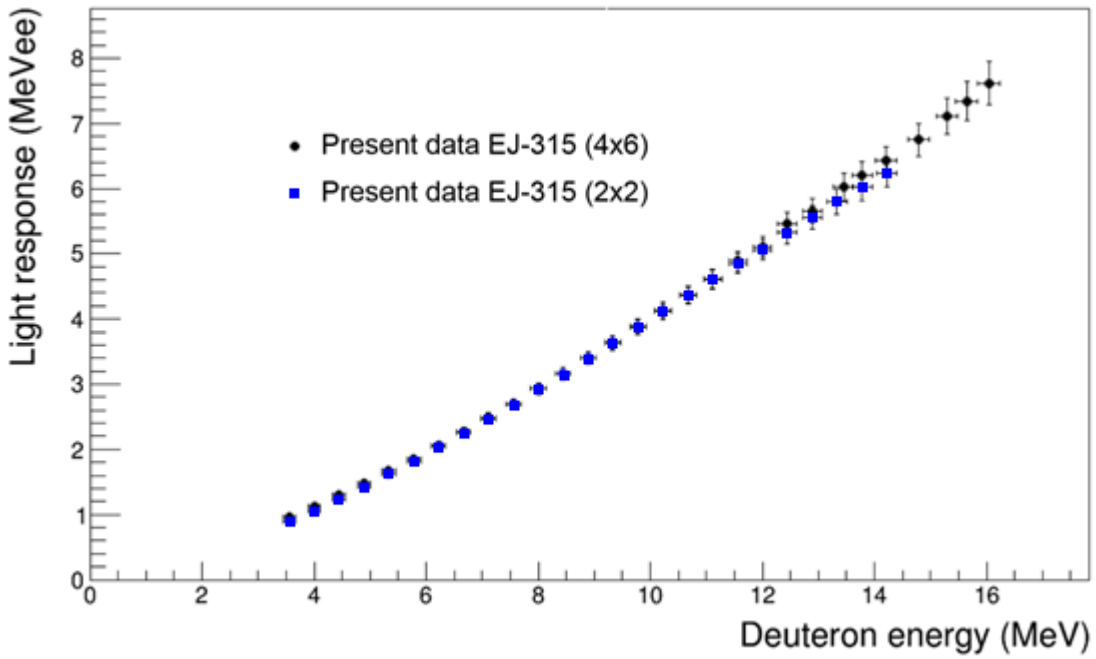

Figure 5.15 - Light-response curve for 2x2 and 4x6 EJ-315 liquid scintillator

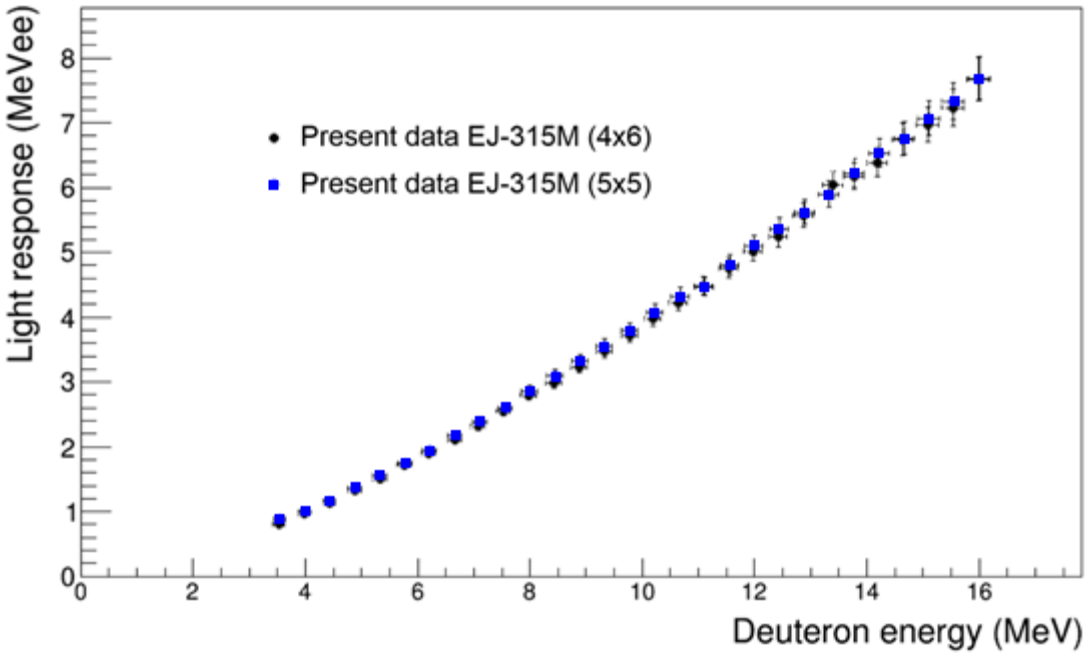

Figure 5.16 – Light-response curve for 4x6 and 5x5 EJ-315M liquid scintillator

This is an indication that the improved PSD performance of EJ-315M is due to an enhancement in the TTA yield rather than an overall increase in light response [Hur14].

Table 5.3 – Fit to combined experimental response data for each scintillation liquid

	Recoil-deuteron light-response parameters		
Scintillator	a	b	c
EJ-315	0.60 ± 0.04	2.33 ± 0.66	0.21 ± 0.05
EJ-315MOD	0.71 ± 0.06	4.21 ± 1.20	0.15 ± 0.03

A survey of response data and empirical fits for Eljen liquids EJ-315, EJ-309, Nuclear Enterprise liquids NE-230, and C_6D_6 was conducted. [Naq94, Cro92, Smi68, Zei74, Law13, Bil13]. The data of [Smi68, Zei74] was converted to MeVee using the relative electron response data provided. A complication of the data relative to the present data is shown in Figure 5.17.

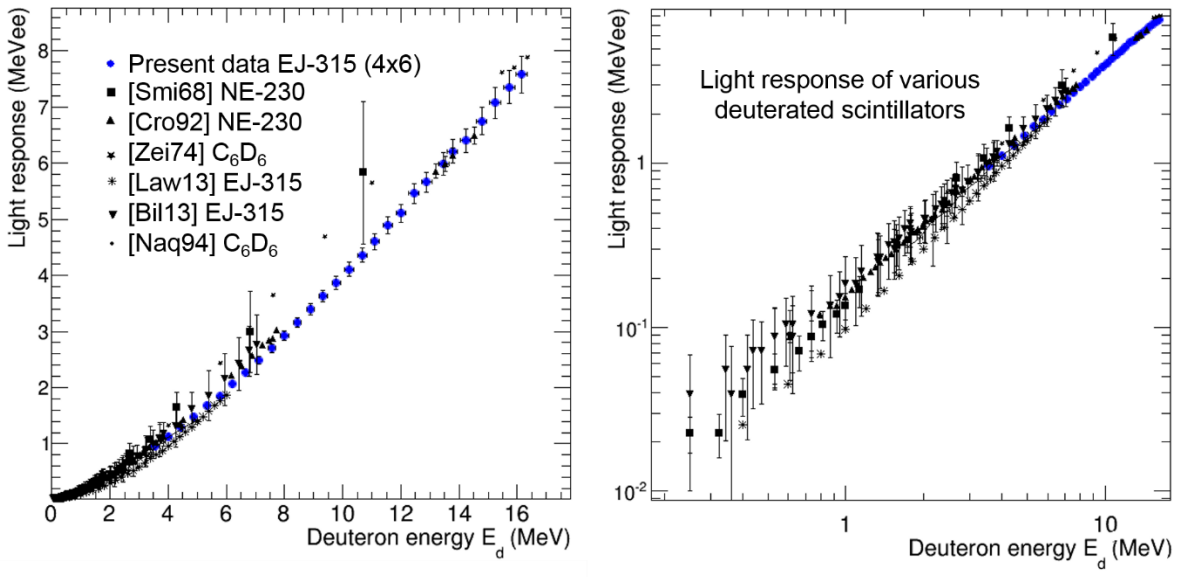

Figure 5.17 – Comparison of light-response data for deuterated scintillators taken from literature

With the exception of the data from [Smi68, Zei74] above 4 MeV, the present data exhibits good agreement with previous measurements. In addition to experimental uncertainties, the differences can be partially explained by the choice of the location to extract the recoil particle

energy to determine the mono-energetic response. For EJ-315 which is the deuterated liquid used in the UM-DSA and DESCANT arrays, the data sets of [Law13] and [Bil13] show very good agreement with the present results. In an attempt to obtain a universal representative response function for EJ-315, a fit was applied to the combination of these three data sets. The parameters are shown in Table 5.4. This combined fit is valid for $0.07 < E_d < 18$ MeV.

Table 5.4 – Fit to experimental response data combined with data from published literature[1]

Recoil-deuteron light-response parameters

Scintillator	a	b	c
EJ-315[1]	0.64 ± 0.05	2.83 ± 0.87	0.18 ± 0.04

[1] Combined with [Law13] and [Bil13]

4. Detector efficiency

In any measurements involving the detection of neutrons the largest source of uncertainty is usually the neutron detection efficiency. Organic scintillator neutron detectors unlike charged particle detectors have an efficiency which is threshold dependent. This is due to the fact that organic scintillators rely on a continuous light response from zero to the maximum transferable energy for monoenergic neutrons. Charged-particle detectors exhibit a single, well-defined peak which is proportional to the energy depositied and thus the efficiency is not threshold dependent. Determination of the neutron detection efficiency must then be measured over the energy range of the desired experiment. Often this is not possible due to difficulties in producing neutron beams with a known flunece and also can be prohibitaly time consuming if many energy steps are required. Due to these difficulties and others, Monte Carlo calculations are often used to simulate detection efficiency in lieu of actual measurements, though this often leads to large uncertainties in cross sections measured. One method around this threshold-dependent efficiency issue is to fit the recoil-deutron peak directly and assign a corresponding recoil peak efficiency. Because this method relies on events in a ‘peak’ rather than a continuum, the efficiency is now threshold *independent*.

The total and recoil-peak neutron detection efficiency of the 2x2 EJ-315 detectors was determined using two techinques. The first techique involved the use of the well-known $d(d,n)^3He$

cross section [Die72]. Since the cross section has been well-documented over a large range of specific energies, it can be used to determine the absolute neutron yield and thus is useful for determination of neturon detection efficiency. The second techique uses the same reaction but in this case the outgoing ^{3}He is measued in coincidence using a SiSB ΔE-E telescope detector. Since every ^{3}He detected has a corresponding neutron produced at a certain angle and energy, the absolute neutron flux at a specific angle can be determined and thus the neutron detection efficiency determined for a specific neutron energy.

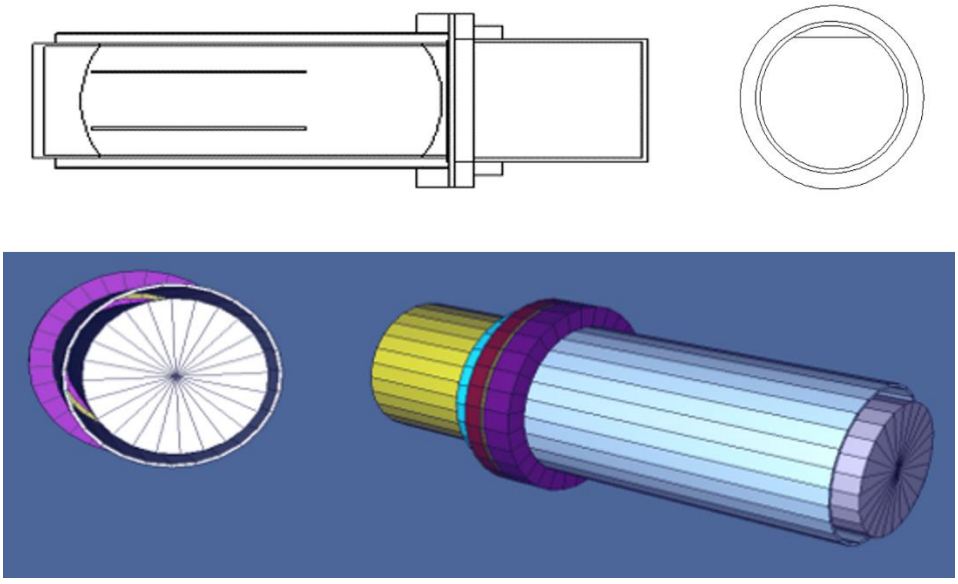

Figure 5.18 – MCNP model of the 2x2 EJ-315 detector in 2D (top) and 3D (bottom)

Measurements were again conducted at the University of Notre Dame's ISNAP laboratory using the FN Van de Graaff accelerator to produce a E_d = 16 MeV deuteron beam impinged on a 2.4 mg/cm^2 deuterated polyethylene target $[C_2D_4]_n$ prepared by an evaporation method described in Appendix F. The 2x2 EJ-315 detector was located 50 cm from the target and beam current was measured using a Faraday cup. At a high neutron energies corresponding to low recoil ^{3}He energies, the ^{3}He was unable to pass through the ΔE detector and efficiency was measured using the target thickness, beam current, and well-known d(d,n)^{3}He cross section [Die72] to determine absolute neutron flux. Efficiency is then simply calculated as the number of neutrons detected over the total number of neutrons which passed through the detector. Since the former results in

a continuous light-response spectrum, this is threshold dependent. For lower energy neutrons corresponding to higher-energy ^{3}He products, the ^{3}He had sufficient energy to pass through the ΔE detector for positive identification and tagging. In this case, efficiency is calculated for neutrons expected from the ^{3}He coincidence versus how many were detected. Recoil-peak efficiency is determined the same way for both cases but instead of the total light response above a threshold, only the recoil-peak is included.

The results were compared with a Monte Carlo (MC) calculation using the program MCNP-PoliMi [Poz03]. The MCNP model of the 2x2 EJ-315 detected used in the simulations is shown in both 2D and 3D in Figure 5.18. Also note the inclusion of the inert gas bubble in the MC model which results in a slight reduction in overall efficiency versus a true 2x2 scintillator. Results from these measurements compared to the results of [Vil11] are shown in Figure 5.19. In regards to the recoil-peak efficiency, the differences observed between the present data and [Vil11] are most likely due to differences in the cutoff point used for the recoil deuteron peak.

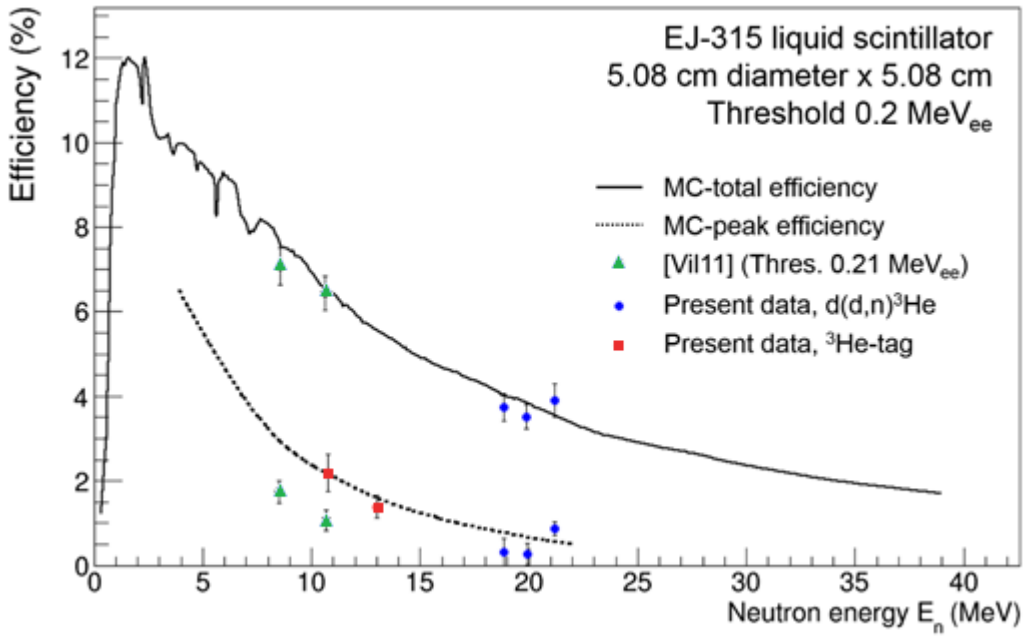

Figure 5.19 – Total and peak efficiency of the 2x2 EJ-315 detector compared to [Vil11]

Good agreement is observed between the present measurements, [Vil11], and the MC simulations. Thus one can conclude that that the use MCNP-PoliMi to model neutron efficiency over this energy range should be sufficient for most measurements.

Chapter 6

Transfer Reaction Measurements and Homeland Security Applications

I. (d,n) Reactions on Solid and Gaseous Target with Stable Ion Beams

1. Benchmark reactions

For evaluation of the spectral unfolding performance of the deuterated scintillators, a systematic study of (d,n) reactions on light nuclei was chosen at E_d = 16 MeV. This study used solid targets of deuterated polyethylene $[C_2D_4]_n$, ^{9}Be, ^{11}B, ^{nat}C, ^{13}C and gaseous targets $^{nat}N_2$, $^{15}N_2$, and ^{17}F as SF_6. Many cross sections and most level schemes of the populated nuclei from these reactions are known and thus provide an ideal set of test-case reactions for detector evaluations.

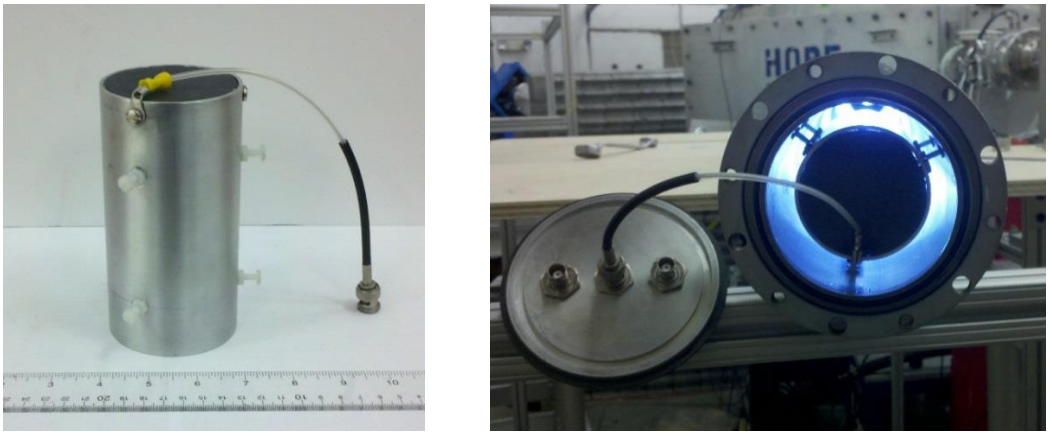

Figure 6.1 - 7.62 cm diameter Faraday cup used in the (d,n) evaluation measurements with scale (left, side view) and installed in beam line (right, head-on view).

2. Experimental setup

The (d,n) evaluation measurement campaign was conducted at the University of Notre Dame's ISNAP laboratory. The deuteron beam was accelerated by the 9 MV FN tandem Van de Graaff accelerator to E_d = 16.0 MeV.

Beam current on target was typically limited to 0.2 – 10.0 nA. To cleanly dump the beam, a 1.9 cm thick, electrically-isolated graphite beam stop which also served as Faraday cup for beam-charge integration was fabricated (as shown in Figure 6.1).

The Faraday cup was encased in a 60 cm x 60 cm x 60 cm paraffin-lined lead cave to reduce beam-induced background. Borated polyethylene pellets and plastic boron-loaded water jugs were used for additional shielding. The 25 cm diameter thin-wall stainless-steel target chamber used was equipped with a movable Si detector mount which permitted rotation of a silicon ΔE-E telescope detector in vacuum. In addition to the Faraday cup, the beam flux through the target was monitored using elastic scattering of the deuteron beam into the silicon telescope detector at a fixed angle.

Figure 6.2 - The experimental setup used in the (d,n) measurement campaign. The 4x6 EJ-315 detectors shown are positioned 1 m from the target.

Both the 4x6 and 2x2 EJ-315 detectors were used in these measurements with the 4x6 detectors is shown around the target chamber in Figure 5.2.2. The 4x6 EJ-315 detectors were located at a radius of 1.0 m and the 2x2 EJ-315 detectors at 50 cm with respect to the central target position.

3. Preparation of solid and gaseous targets

Deuterated polyethylene targets $[C_2D_4]_n$ were prepared by an evaporation method described in Appendix F. The ^{9}Be, ^{11}B, ^{nat}C, ^{13}C targets were thin foils ranging from 0.4 to 6.0 mg/cm^2 in thickness, with isotopically-enriched material used for the ^{13}C target. Most of the solid targets were self-supporting foils except for one of the two ^{13}C targets used, which were on a thin Mylar backing and had been fabricated at Indiana University. Owing to the large positive $^{13}C(d,n)$ Q value, interference from the backing elements (^{12}C in particular) was not an issue as we are mainly using the distinct, high-energy recoil-deuteron peaks for cross-section measurements. For the gaseous targets, a gas cell was fabricated by the author from free-cutting brass (Alloy 360) which was chosen for its low Q values for (d,n) reactions within the alloy and it's 6high machinability (Figure 6.3).

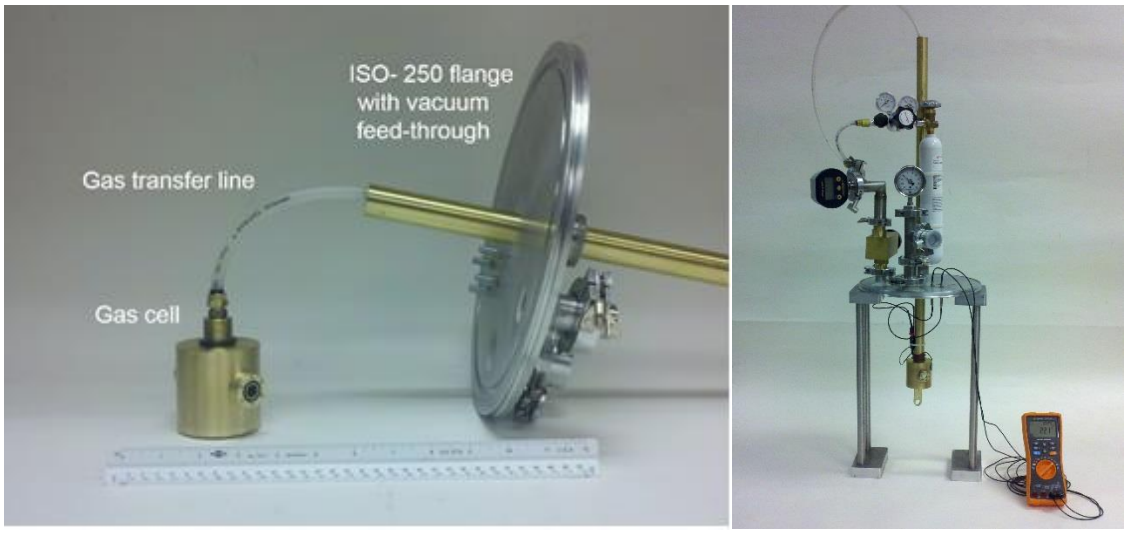

Figure 6.3 - Gas cell used in the (d,n) measurement campaign showing connection to the top of the vacuum chamber (left) and fully assembled with ^{15}N gas canister, regulator, temperature, and pressure sensors (right).

The gas cell has 1.0 cm dia. hermetically-sealed entrance and exit windows which can be easily changed in case of failure. 10 μm Havar® metal foil was used as the window material. The gas handling system was located outside of the vacuum chamber through a 2.54 cm dia. vacuum feed which allowed for easy and fast gas changes during experimental runs. Digital temperature and absolute pressure gauges monitored gas parameters throughout a run.

II. The $^{12}C(^{3}He,n)^{14}O$ Reaction

Another evaluation of the performance of the UM-DSA was conducted using the (^{3}He,n) reaction on ^{12}C, ^{26}Mg, and ^{74,76}Ge. In the case of ^{26}Mg and ^{74,76}Ge, these reactions were chosen based on previous work with a large n-ToF wall [Rob13]. The $^{12}C(^{3}He,n)^{14}O$ reaction also has been measured and thus provides another reaction for comparison. The experiments were again performed at the University of Notre Dame's ISNAP laboratory. For these experiments, the FN tandem Van de Graaff accelerator was used to accelerate a primary beam of ^{3}He to 16.0 MeV. The same experimental beam line and detector mounts used in the (d,n) measurements were used with the exception of the target chamber and beam dump. These were replaced with a smaller 20 cm diameter chamber and an isolated Au beam stop located inside the chamber. This permitted cross section measurements at 0 deg. A 200 μg/cm^2 natural carbon target (98.9% ^{12}C) was used and smaller but isotopically-enriched targets of ^{26}Mg and ^{74,76}Ge.

III. The $^{13}C(\alpha,n)^{16}O$ Reaction

With success of the (d,n) and $^{12}C(^{3}He,n)$ measurements at high neutron energies (Chapter 7.1), the decision was made to investigate the performance of the system with lower energy neutrons. An ideal reaction for this study was the astrophysically-important $^{13}C(\alpha,n)^{16}O$ reaction which serves as the main neutron source for the s-process [Hei08]. The experiment was conducted at University of Notre Dame's ISNAP laboratory as a joint experiment with the University of Michigan, the University of Notre Dame, and led by the University of Tennessee and Oak Ridge National Laboratory. Figure 6.4 shows the experimental setup for the experiment with the large 5x5 EJ-315M detector located at 35^{o} lab at a distance of 1.2 m. The array of long white bars in Figure 6.4 are the VANDLE n-ToF detector array. An excitation function was measured between

E_α = 3.275 – 7.600 MeV with the primary α beam being accelerated by the FN tandem Van de Graaff accelerator onto a 200 μg/cm^2 ^{13}C target. Beam current on target was typically limited to 15 nA. The primary beam was cleanly dumped into the setup described in §6.1 with exception of the graphite beam stop which was replaced with a thick tantalum plate.

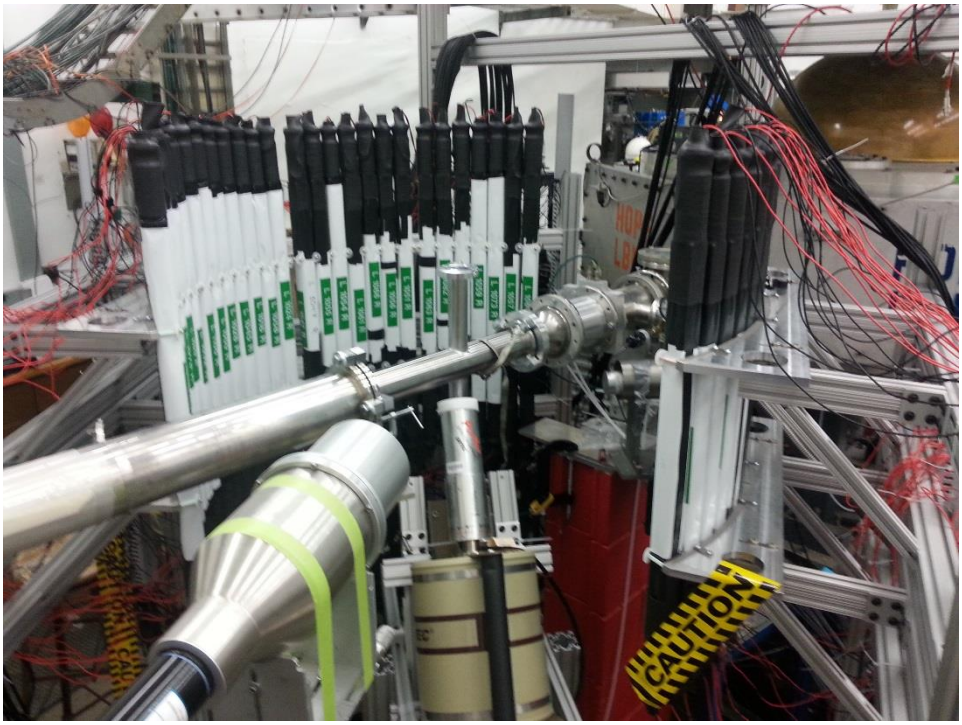

Figure 6.4 - The experimental setup used in the ^{13}C(α,n)^{16}O measurement campaign.

IV. The d(^{7}Be,n)^{8}B Reaction using a Radioactive Ion Beam

1. First RIB reaction with UM-DSA: the d(^{7}Be,n)^{8}B reaction at E(^{7}Be) = 31 MeV.

The final experiment conducted in this work was a measurement of the d(^{7}Be,n)^{8}B reaction, which involved use of a rare and radioactive ion beam ^{7}Be in inverse kinematics. For this experiment, a primary beam of ^{6}Li was supplied by the UND FN tandem Van de Graaff accelerator at E(^{6}Li) = 35 MeV. The secondary ^{7}Be RIB was produced by the ^{3}He(^{6}Li,d)^{7}Be using a gas cell of ^{3}He with 5 μm titanium entrance and exit windows. It was found that a gas pressure of ~1.5 atm ^{3}He and 700 enA (electrical nA) was sustainable to maximize RIB production and limit rupture of the cell windows. A secondary beam rate of 5x10^5 ^{7}Be per second at E(^{7}Be) = 31 MeV and FWHM of about 1 MeV was maintained throughout the experiment.

2. n - ^{8}B coincidence tagging

Due to the nature of measurements with RIBs, as indicated in §1.1 a set of additional challenges presented itself. Beam purity, low beam intensity, and neutron background from the production target (and natural sources) required that ^{8}B be detected in coincidence with the outgoing neutron to obtain a clean (d,n) neutron spectrum. From reaction kinematics, the outgoing ^{8}B ranged from $0 - 8^{0}$ in the laboratory frame for ground-state population of ^{8}B. The angular range is decreased when ^{8}B is populated at higher excitation energy. The large beam spot size of the secondary ^{7}Be RIB and the narrow ^{8}B angular range meant the recoil detector would intercept the ^{7}Be beam and have to handle the intensity of the RIB, around $5x10^{5}$ ^{7}Be per second. This rate is well above the limit for a silicon detector and attempts using an ion chamber from ORNL failed due to the time required for charge collection, which leads to signal distortion and significant pileup. What was needed was a detector which could provide energy separation of the beam contaminants at a rate of 10^{5}-10^{6} particles per second. A good solution was found and implemented by the author which utilized a fast plastic scintillator operated in vacuum.

3. In-beam, high-rate recoil detector.

The design for the high-rate recoil detector involved the use of an EJ-200 fast plastic scintillator operated in vacuum and optically coupled to a quartz vacuum view port. Optically coupled to the side of the viewport in atmospheric pressure was an ETEL 9807B PMT and Eljen –VD-9807 PMT base. This design allows for the high-voltage components to be operated at atmospheric pressure and the window material, quartz, provides minimal scintillation-light attenuation. A 5.08 cm diameter x 5.08 cm cylinder of EJ-200 plastic scintillator was machined down to a final diameter of 4.76 cm with a lip for structural support in the 5.08 cm ID beam pipe. Polishing of the machined regions was done in sequence with 400, 600, and 800 grit silicon-carbide waterproof paper with a final polish with 9 micron alumina powder, prepared as a paste with distilled water. A useful reference on the machining and polishing of plastic scintillators may be found in [Elj98].

4. ^{7}Be RIB production and characterization

The aforementioned ^{7}Be beam was produced in flight using the ^{3}He(^{6}Li,d)^{7}Be reaction with a ^{3}He gas cell. Separation of unwanted reaction products and the primary ^{6}Li ions was done by magnetic-rigidity separation using the UM-UND *TwinSol* device. *TwinSol* consists of two superconducting solenoid magnets which provides an axially symmetric magnetic field with internal field up to 6 Tesla [Lee99]. Separation of beam components is done by the differences in magnetic rigidity of the ions. The non-relativistic form of the magnetic rigidity is

$$B\rho = \frac{p}{q} \xrightarrow{classical} \frac{\sqrt{2mE}}{q}$$

Figure 6.5 shows a ray-trace calculation of the ^{7}Be secondary beam which is used for final focusing the RIB at the target position. A tantalum collimator located at the midplane position blocks the off-focus, unwanted beam components. To reduce fast neutrons from the production target from traveling down the beam pipe to the target position, a 5 cm diameter by 30 cm high-density polyethylene neutron shadow bar was fabricated and installed at the center position of first solenoid. Neutrons, unaffected by the magnetic field, scatter in the collimator while the charged ^{7}Be beam is deflected around the shadow bar (Figure 6.5).

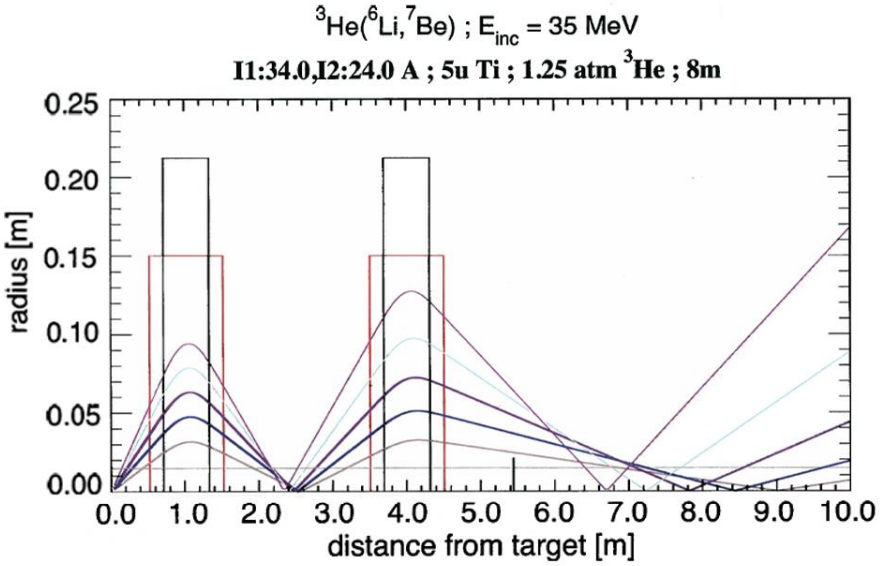

Figure 6.5 - Ray trace calculation of the ^{7}Be beam through *TwinSol* with final focusing at the target position.

Figure 6.6 shows a ΔE-E silicon telescope detector spectrum at 0° of the secondary beam at low rate showing the ^{7}Be and the beam contaminants. Beam purity was found to be 95% with ^{6}Li being the major contaminant.

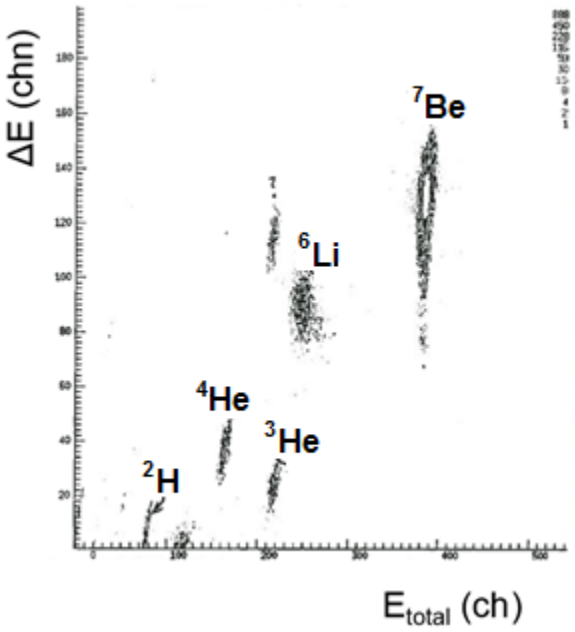

Figure 6.6 – ΔE-E_{tot} plot of ^{7}Be beam and contaminants at the target location after separation and focused in *TwinSol*

5. Experimental setup for d(^{7}Be,n)^{8}B

The experimental setup for the d(^{7}Be,n)^{8}B measurement is shown in Figure 6.7. A 1.4 mg/cm^{2} deuterated polyethylene target was prepared using the procedure described in Appendix F. The UM-DSA was setup at forward angles which corresponds to the highest energy (d,n) reaction neutrons.

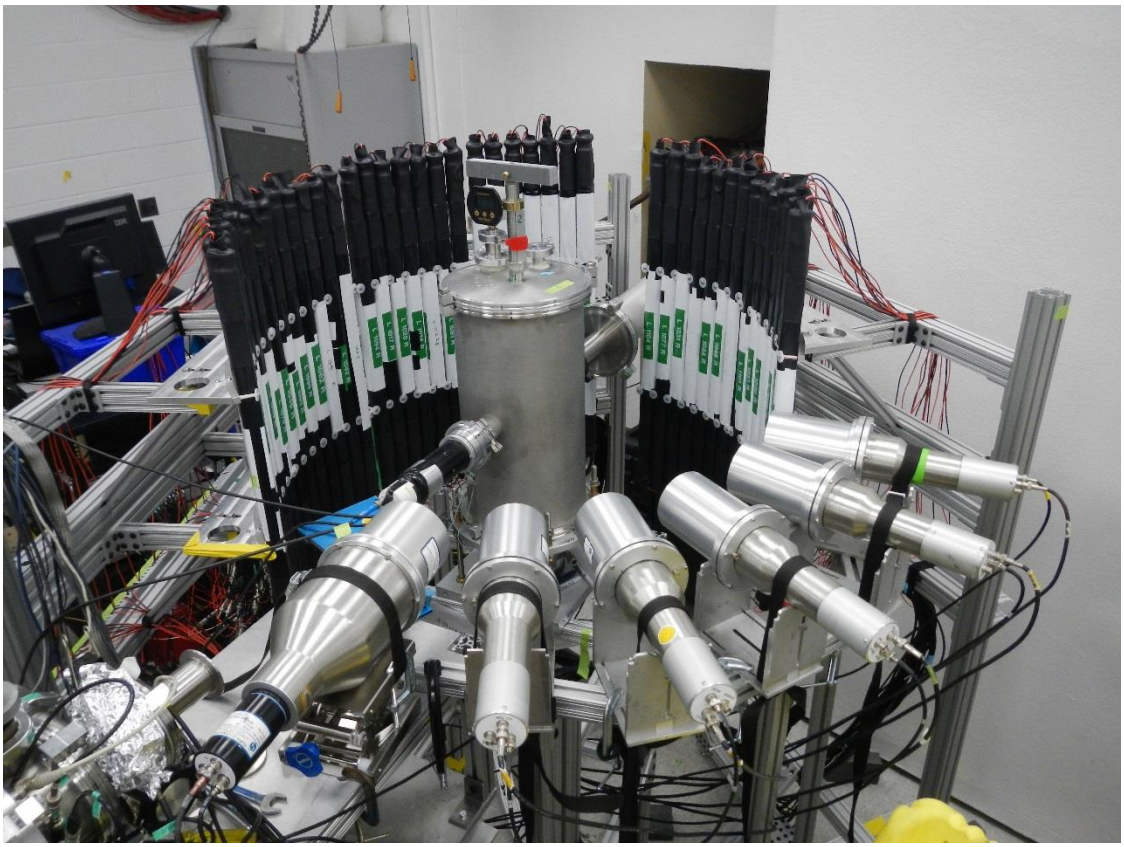

Figure 6.7 - Experimental setup for the d(^{7}Be,n)^{8}B experiment showing the UM-DSA at forward angles and the VANDLE [Pau14] array at back angles.

V. Homeland Security Applications

Measurements which are important in the field of nuclear safeguards and homeland security typically involve the measure of neutron spectra with continuous-energy distributions [Doy08]. These material are typically referred to as special nuclear material (SNM) [Doy08] such as U and Pu compounds. These materials are heavily regulated and laboratory detector characterization measurements are often performed with other neutron-producing materials with continuous-energy distributions such as ^{252}Cf and PuBe.

To investigate the performance of UM-DSA for these types of applications, a series of measurements were performed with ^{252}Cf and PuBe neutron sources. Since neutrons produced by

^{252}Cf are from spontaneous fission, n-ToF can be used to determine the incident energy spectrum. This is done by placing a detector in close proximity to the ^{252}Cf source which serves as the 'start detector' and another at some farther distance known as the 'stop detector'. A detailed study of 252Cf neutron spectrum with deuterated scintillators has been conducted by [Law14].

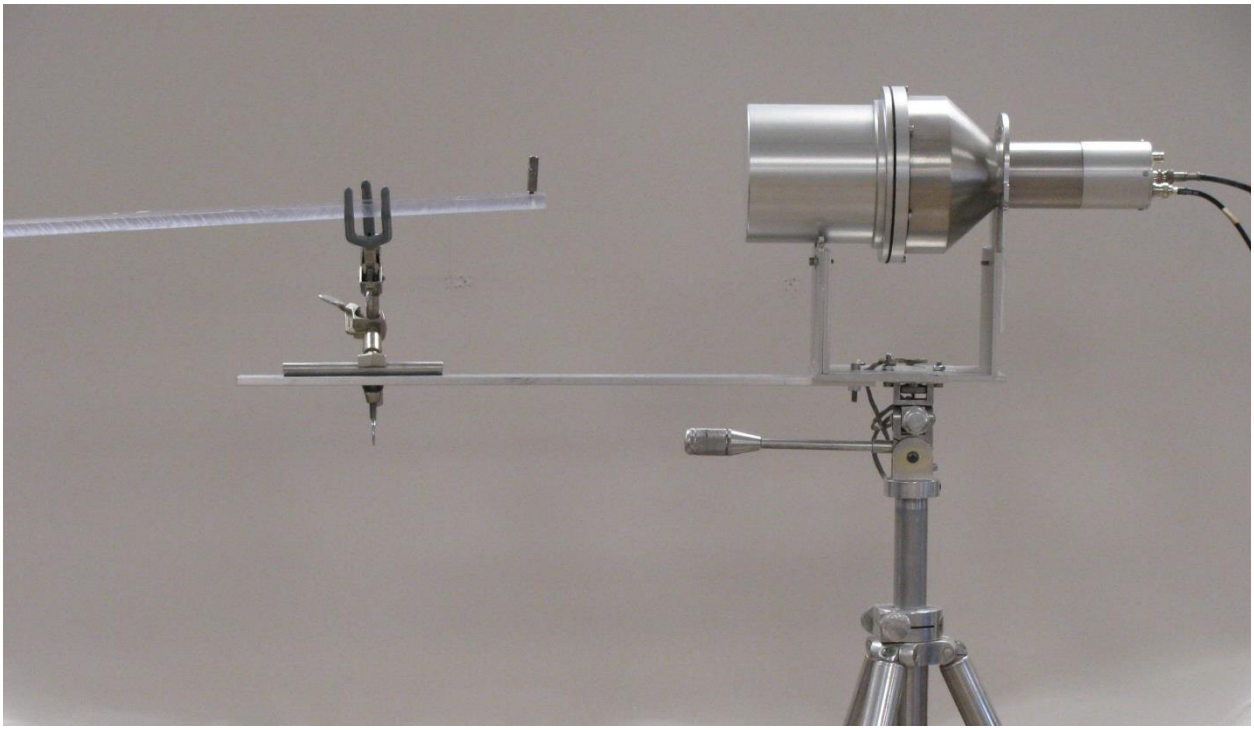

Figure 6.8 - Experimental setup for the PuBe measurement showing the 5x5 EJ315M scintillator mounted on a tripod stand. 1.27 cm lead plate not shown in figure.

The neutron spectrum from PuBe source come primarily from (α,n) reactions of Pu α's on Be. Since the start time of the alphas cannot be determined, n-ToF is not possible and thus the neutron spectrum is measured directly. For this measurement, 1.27 cm of lead was placed between the PuBe source and the 5x5 EJ-315M detector to reduce the amount of gamma rays incident on the detector. The entire setup was mounted to a low-profile tripod shown in Figure 6.8 which elevated the setup above the floor and away from surrounding walls. This reduces unwanted room return.

Chapter 7

Results and Discussion

I. The (d,n) Reaction on Light Nuclei at E_d = 16 MeV

1. Experimental details

The commissioning experiments were designed to cover a broad range of neutron energies and spectra to test the performance and spectral unfolding capability of the UM-DSA. The choice of gaseous and solid targets introduced various neutron transport scenarios from production in the target to detection by the liquid scintillators. This is especially important to understand since the neutron spectra are directly determined from unfolding the raw light-response spectra.

Table 7.1 – Experimental details and uncertainties for the (d,n) measurements

Target	Mean beam energy[1] (MeV)	Lab angular range (deg)	Detector solid angle (10^{-3} sr)	Angular acceptance (deg)	Target thickness (mg/cm^2)	Uncertainties	
						Solid angle (%)	Target thickness (%)
^{9}Be	15.85	10-170	7.73	5.82	1.85	1	1
^{11}B	15.35	10-170	7.73	5.82	23.1	1	1
^{12}C	15.99	10-170	7.73	5.82	0.40	1	1
^{13}C	15.69	10-170	7.73	5.82	8.55	1	1
^{14}N	15.43	10-170	7.73	5.82	3.2	1	10
^{15}N	15.41	10-170	7.73	5.82	3.7	1	10
^{19}F	15.55	10-170	7.73	5.82	8.0	1	10

[1]Mean beam energy is defined as beam energy at half target thickness

The ground-state properties of these nuclei are fairly well known and thus they provide useful test cases. Experimental details and uncertainties for the reactions measured are listed in Table 7.1. Each spectrum was processed using the procedure in §5.2 and recoil deuterons were gated out of the DPSD spectrum to extract neutron spectra. The mean beam energy for each reaction was taken as the energy of the projectile at half the target thickness. The solid angle of each detector was determined using Monte Carlo calculations. Solid-target thicknesses were measured with an alpha gauge, while gaseous targets used the known volume, the measured temperature, and the pressure which were recorded throughout an experimental run. Typically data acquisition time was approximately 30 minutes per set of angles.

2. Light-response spectra

Events were processed using the procedure described in §5.2. An offset parameter of 18 ns was used for the DPSD. Once the digital waveforms were processed, deuteron-recoil events were gated, and calibrations applied using the calibration procedure described in §3.4. The individual light-response spectra were parsed into histograms with 10 keVee bin width from 0.01 to 10 MeVee and stored for inputs into the MLEM code. Figure 7.1 shows a sample light-response spectrum above threshold (2 MeVee) from the d + $[C_2D_4]_n$ reaction at 10 deg. (lab) and E_d = 16 MeV. The sharp cut off at 2 MeVee is due to a software threshold applied to the data.

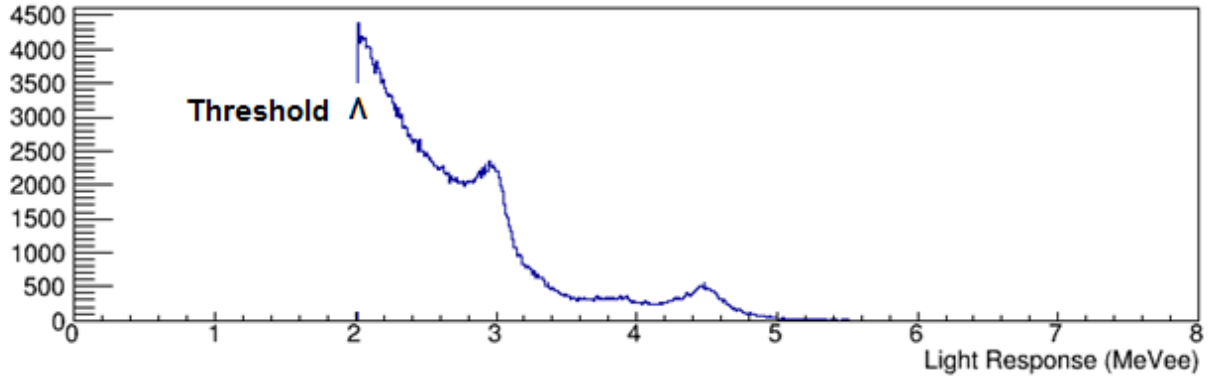

Figure 7.1 - Raw light-response spectrum from the d + $[C_2D_4]_n$ reaction at 10 deg. (lab) and E_d = 16 MeV. Software threshold indicated.

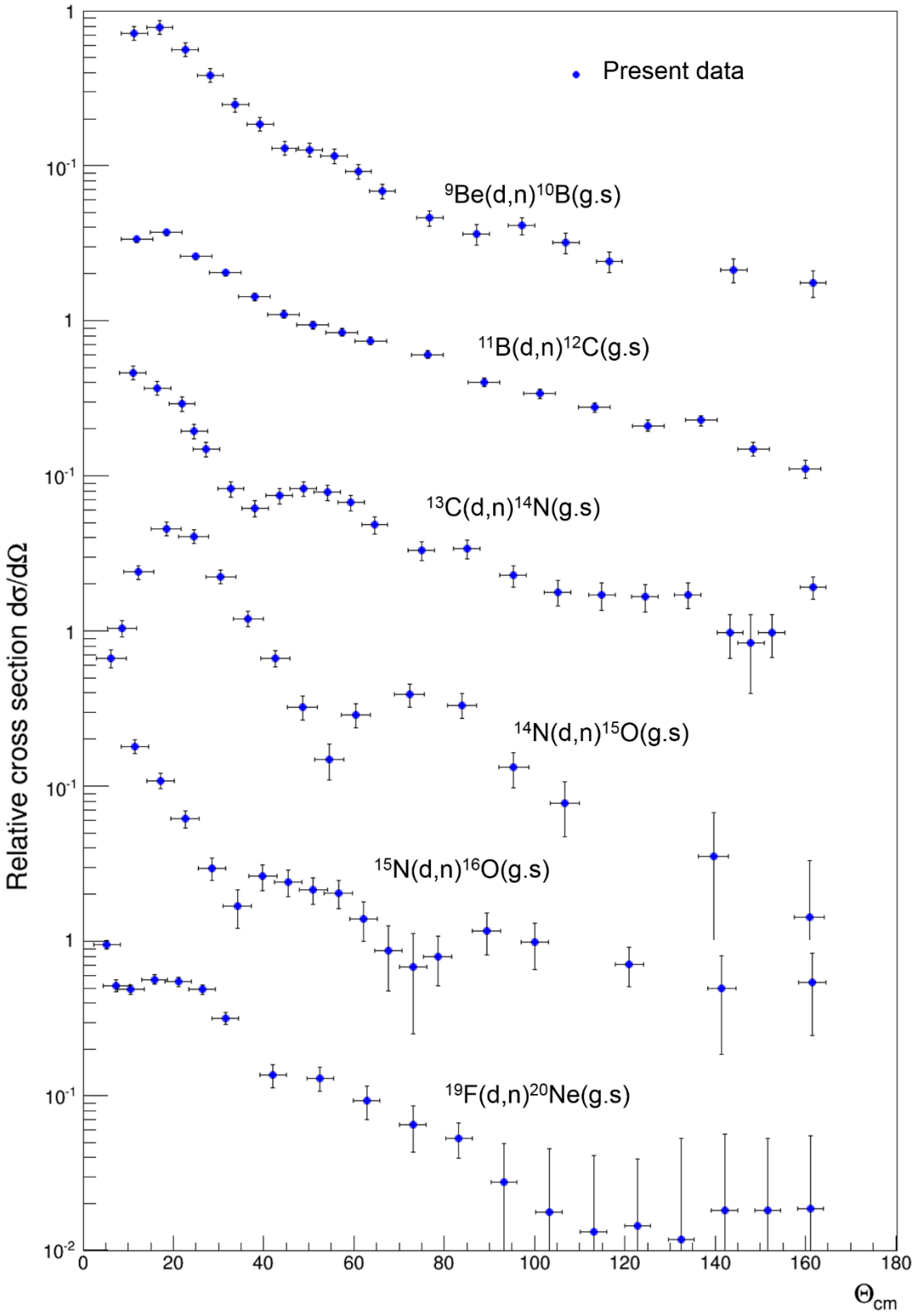

Figure 7.2 – Relative ground-state differential (d,n) cross sections to ground states.

As observed by others [Bro81, Bro88, Lis81, and Oja10], the light-response spectrum show recoil peaks at discrete neutron energies corresponding to excited levels of the populated final nucleus. The spacing of these levels in the light response is different than a traditional n-ToF plot in the sense that the level spacing is roughly proportional to the neutron energy as opposed to the peaks in n-ToF being proportional to the square root of the neutron energy. Another important feature is that lower-energy peaks are 'stacked' on top of higher-energy peaks. For example, if we have two energy groups A and B where E(A) > E(B), we cannot explicitly tell if a neutron came from energy group A or B below E(B). Inspection of each spectrum vs. angle shows clearly the reaction kinematics with a shift in the ground-state recoil peak energy with angle.

We wish to ultimately convert these spectra into differential cross sections for which we can extract properties of the final nucleus. There are two methods which we can employ: ground-state peak fitting and spectrum folding. The first being a far simpler method but only useful for ground-state peaks (i.e. the highest neutron energy group with no underlying background spectrum). The second involving full inverse problem treatment as described in §3.6. I'll start with the simpler case where we only focus on the ground-state recoil peak.

In this method the ground-state recoil peak is fitted with a Gaussian shape and integrated to obtain number of counts per recoil peak [Feb13]. This recoil peak is also then given a recoil-peak efficiency. Note that since we are treating the recoil peak as a Gaussian-like peak, the detection efficiency is threshold *independent*. The differential cross section becomes,

$$\left(\frac{d\sigma}{d\Omega}\right)_{lab} = k\frac{N}{\epsilon_p \Omega \mathrm{AI}} \tag{7.1}$$

where N is the number of observed counts, ϵ_p is the recoil-peak efficiency, Ω is the solid angle, A is the target areal density, I is the total number of incident beam particles, and k is a constant. Using Equation 7.1 and the recoil-peak efficiency from §5.4, the ground-state cross section from each target is shown in Figure 7.2 converted to the CM system [Ber04]. The main uncertainty comes from the uncertainty in the recoil-peak efficiency which is estimated at (10%). The angular cross sections shown in Figure 7.2 are arbitrary normalized. The y-axis on Figure 7.2 is meant just for scale. The important of this plot is to show the location of the first peak which determines the l-value of the reaction. This can be extracted without absolute normalization since a

comparison is only made on the relative shape compared to DWBA calculations rather than an absolute scale as needed for spectroscopic factors.

The ^{9}Be(d,n)^{10}B reaction has been previously measured at E_d = 16 MeV [Par73] and conveniently provides a direct comparison of the peak-fitting method to the traditional n-ToF method used by [Par73]. Very good agreement with the data of [Par73] is observed and demonstrates the simplicity and reliability of this method. With the exception of nuclear astrophysics, ground-state cross sections alone are not often of interest without excited states included. For this we'll need to rely on spectrum unfolding techniques to extract the neutron energy spectrum from the raw light-response spectrum.

3. Spectrum unfolding

In the previous section it was mentioned that the raw light-response spectra were gated on the recoil deuteron peak and parsed into histograms with 10 keVee bin width. Recall from §3.6 that the incident neutron spectrum can be determined by solving the inverse problem $\bar{x} = \bar{\bar{R}}^{-1}\bar{s}$. $\bar{x} = \bar{\bar{R}}^{-1}\bar{s}$ cannot be solved directly but one can use spectrum unfolding methods such as the MLEM algorithm and a numerical solver. Using the MLEM method described in §3.6, the incident neutron spectrum from each (d,n) light-response spectrum was unfolded. Recall that this technique provides a numerical solution to the ill-posed inverse problem using a Bayesian interference framework. The program works by inputting a response matrix, light response spectrum to unfold, and asks the user for the maximum number of iterations, energy threshold, and if *a priori* information can be supplied. The *a priori* information is in the form of an energy range for a given number of peaks. For the spectra presented in this dissertation, no *a priori* information was applied and the initial guess of the neutron spectra was just a unity vector. The code has the option to constrain the response matrix to only include certain values by simply setting undesired energy bin elements in the initial guess to zero. Since the MLEM algorithm is multiplicative, these elements remain zero throughout the iterations. It was found that the quality of the unfolded spectra was sufficient and this option was not needed for the data sets evaluated in this work. The threshold was typically set at 2 MeVee in software. This high threshold allowed very good gamma-neutron separation and recoil proton – deuteron separation. Below 2 MeVee, it is difficult to separate recoil protons and deuterons. Overall this is not a substantial hindrance for the

technique as the d(n,nnp) breakup cross section increases with increasing neutron energy so at low energies, breakup effects are minimal, and for higher-energy neutrons higher thresholds can be applied (and was done). Each spectrum took around 7 seconds to unfold a light-response spectrum using a 300 x 1500 bin response matrix on a Windows® computer using an Intel® Core i7-4702MQ 2.20GHz processor. The limiting factor to running near real-time processing is the time required to process the digitized waveforms, which on average took approximately 1 hour per 30 mins of acquisition time per detector for the experimental count rates used. Nearly 90% of the acquired data was due to gamma-ray events and were vetoed by the DPSD. An estimated light-response spectrum also is generated by taking the unfolded spectrum and feeding through the forward problem (Equation 7.2).

$$\bar{e}_{MLEM} = \bar{\bar{R}}\bar{x}_{MLEM} \tag{7.2}$$

It is meant to serve as a visual check of the unfolding calculation. The unfolded spectrum includes the threshold-dependent intrinsic detection efficiency. The uncertainty propagation in neutron spectrum unfolding methods is still not well understood [Reg02, Mat02]. Approximations used for the uncertainty in the unfolded result are discussed below in extraction of the spectroscopic factors (see also §7.5).

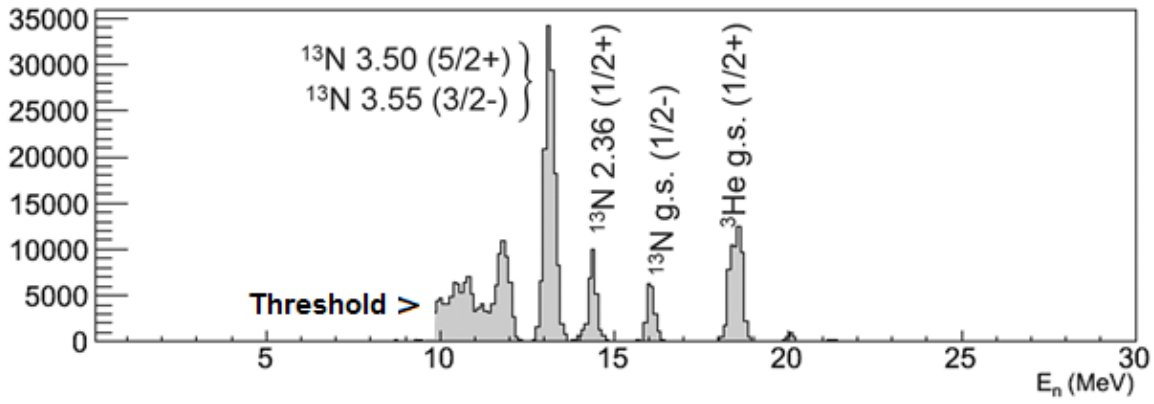

Figure 7.3 – Unfolded neutron spectrum from the d + $[C_2D_4]_n$ reaction at 10 deg. (lab) and E_d = 16 MeV. Software threshold indicated.

Unfolding results for the d + $[C_2D_4]_n$ reaction at 10 deg. (lab) is shown in Figure 7.3. The ground state of ^{3}He and of ^{13}N, and excited states of ^{13}N from the reaction of deuterons on ^{2}H and

^{12}C respectively are clearly seen. The E_x = 3.50 and 3.55 MeV states of ^{13}N are not separated but a sum peak is observed. The proton separation energy for ^{13}N is S_p = 1.943 MeV and thus the excited states in ^{13}N observed are proton unbound. This is an important result as it demonstrates the spectroscopic capability of the array for the study of very short-lived unbound states, which will become more relevant in the transition to experiments involving RIBs. The lifetimes of the states observed correspond to decay widths of Γ= 31.7, 62, and 47 keV respectively [ENDF/B-VII.0]. The d(d,n)^{3}He cross section was determined at 10, 15, 30, and 130 deg. (lab) by integration of the ^{3}He ground-state peak. Since the d(d,n)^{3}He cross section is well known, detection efficiency can be determined by comparing the ratio of the uncorrected measured cross section with the published data. Of course in this case, the threshold-dependent intrinsic detection efficiency correction option made in the MLEM code was turned off. The efficiency values are discussed in §5.4.4.

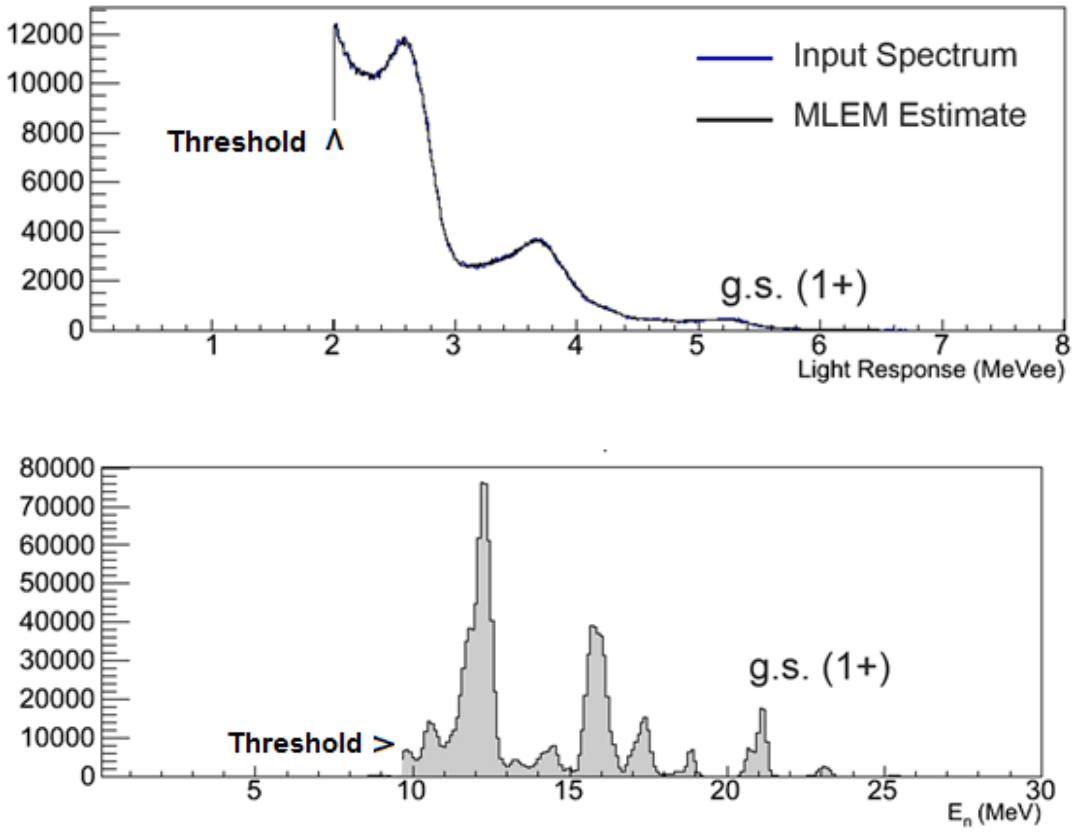

Figure 7.4 – Raw light-response spectrum (top) and unfolded neutron spectrum (bottom) from the ^{13}C(d,n)^{14}N reaction at 20 deg. (lab) and E_d = 16 MeV. Software threshold indicated.

The unfolding procedure for the other targets followed the recipe used for the d + $[C_2D_4]_n$ spectra. The threshold was typically set at 2 MeVee in software with the exception of the d + SF_6 spectra beyond 90 deg. (lab) which has slightly poorer deuteron – proton separation and required a threshold of 2.5 MeVee. Figure 7.4 shows the raw light-response spectrum and unfolded neutron spectrum from the $^{13}C(d,n)^{14}N$ reaction at 20 deg. (lab) with the ^{14}N ground state labeled. The black line in the light-response spectrum represents the raw data and the blue line corresponds to the MLEM estimate after 5000 iterations. The fit between the MLEM estimate and the raw light response spectrum is very good indicating the response matrix adequately describes the spectral response. Note a small spurious peak appears at E_n = ~23 MeV just beyond the ^{14}N ground peak. Further investigation shows that this is due to recoil protons which leak into the deuteron DPSD gate. The overall effect is small but adds to the systematic uncertainty of the measurements.

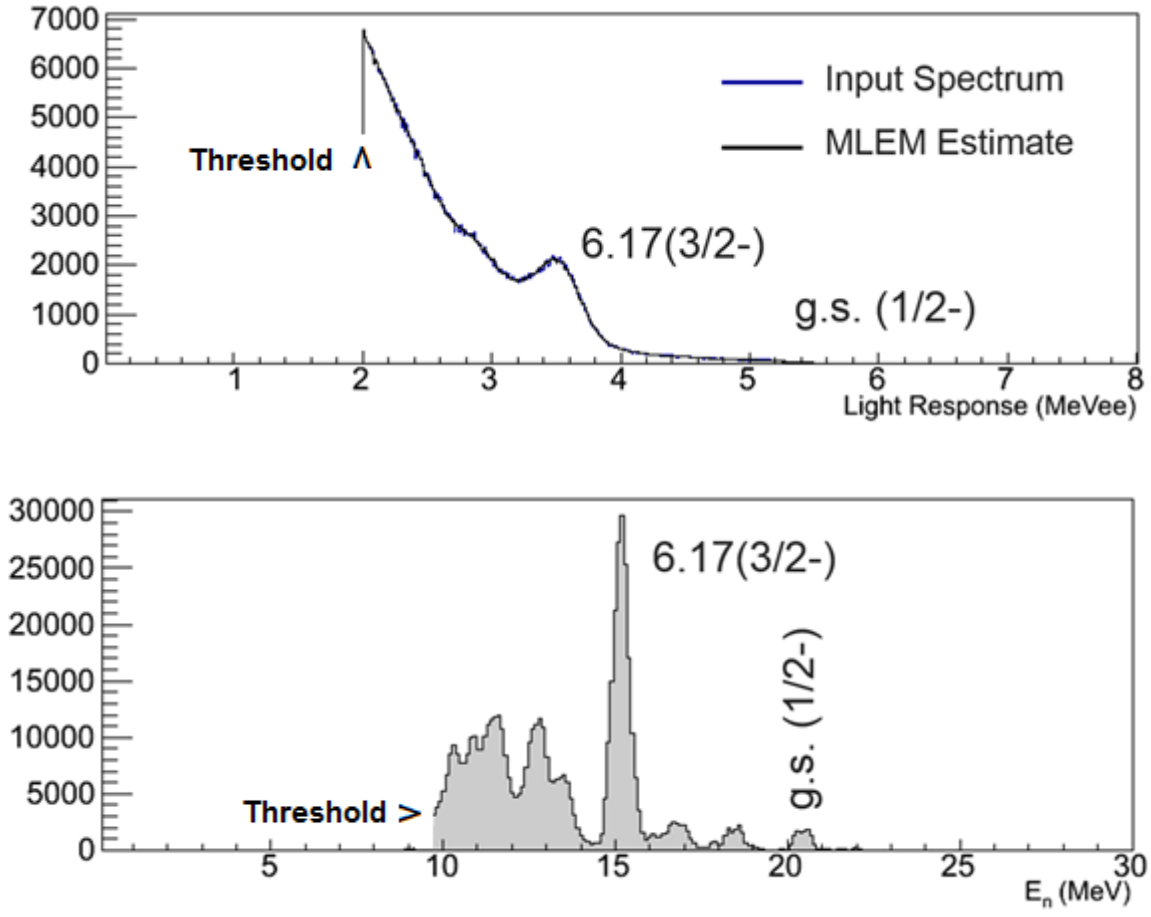

Figure 7.5 – Raw light-response spectrum (top) and unfolded neutron spectrum (bottom) from the $^{14}N(d,n)^{15}O$ reaction at 5 deg. (lab) and E_d = 16 MeV. Software threshold indicated.

Spectrum unfolding results for the $^{14}N(d,n)^{15}O$ reaction at 5 deg. (lab) are shown in Figure 7.5. The ground state and E_x = 6.17 MeV excited state are labeled. As with the $^{13}C(d,n)^{14}N$ unfolding results, the MLEM estimate adequately describes the spectral shape of the raw light-response spectrum. An interesting feature which is present in all three unfolding results shown is the rich amount of information that is extracted by the MLEM from the raw light response. By eye, one can identify only the strongly populated levels but the spectrum unfolding technique appears able to extract reliably more details in the incident neutron spectra from the raw light-response spectra.

4. Differential cross sections

Once the unfolded neutron spectra are obtained the differential cross section can be determined using Equation 7.3:

$$\left(\frac{d\sigma}{d\Omega}\right)_{lab} = k\frac{N}{\epsilon\Omega \mathrm{AI}} \tag{7.3}$$

where N is the number of observed counts in the unfolded spectrum for a given state, ϵ is the threshold-dependent efficiency, Ω is the solid angle, A is the target areal density, I is the total number of incident beam particles impinged on the target, and k is a constant. The total number of particles was calculated from the integrated beam current on the downstream Faraday cup. Recall that the threshold-dependent efficiency is included as an output of the MLEM code. This is quite convenient as one can adjust the MLEM threshold to yield convergence and the efficiency is then determined. Cross sections are calculated in the center-of-mass frame of reference by conversion using the appropriate Jacobian, Equation 7.4. The differential cross sections are shown in Figures 7.7 - 7.12.

$$\left(\frac{d\sigma}{d\Omega}\right)_{cm} = \left(\frac{d\Omega_{lab}}{d\Omega_{cm}}\right)\left(\frac{d\sigma}{d\Omega}\right)_{lab} \tag{7.4}$$

We now wish to extract nuclear information from DWBA and reaction theory. Recall from Chapter 4, that the shape of the differential cross section is related to the angular momentum transfer of the reaction. DWBA allows us to probe the single-particle nature of the populated states. To begin, we will need the optical model potential (OMP) for the incoming and outgoing particles, and valence proton – core potentials for the target and product nuclei. For extraction of spectroscopic factors it is preferable that one use global OMPs over local potentials as the former represent an average trend over a mass region rather than an individual fit to specific nuclei. Many global potentials exist for protons, neutrons, and deuterons on nuclei above ~A=27 [Bec69, Var91, Dae80] covering a broad mass and energy range. For light nuclei, these global potentials show significant deviations from measurements. Heavy nuclei contain many nucleons with relatively small level spacings which leads to an overall statistical averaging of the nucleon-nucleus potential. No single state typically dominates the absorptive potential. In light nuclei this averaging effect is not applicable. The low number of nucleons involved and the relativety large energy spacings allow individual states to strongly dominate the absorptive potential thus leading to difficulties with a global OMP. This can be thought of as a many but not too-many-body problem. There are too few bodies to use statistical treatments but too many to use single-nucleon treatments. To explicitly show this effect Figure 7.6 contains a comparison of deuteron elastic scattering data with calculations using local OMPs, and the Daehnick global OMP [Dae80] which is valid for $A \geq 27$. As predicted, significant deviations are observed when using the global potential over the entire mass range shown. After careful evaluation, it was determined that the major deviation is due to an over prediction of the absorptive (imaginary) surface potential. Figure 7.6 also contains a modified Daehnick potential where SFresco [Tho88] was used to adjust the imaginary surface term to improve the fits. A list of local deuteron optical model parameters used is tabulated in Table 7.2.

Table 7.2 – Local deuteron optical model parameters used to fit the elastic scatter data

Partition	E_d (MeV)	V_o (MeV)	r_R (fm)	a_R (fm)	W_s (MeV)	r_s (fm)	a_s (fm)	W_v (MeV)	r_v (fm)	a_v (fm)	V_{so} (MeV)	r_{so} (fm)	a_{so} (fm)	r_c (fm)	Ref.
d + ^{6}Li	14.7	153.4	1.18	0.489				3.45	2.97	0.489				1.3	[Mat69]
d + ^{7}Li	14.7	127.0	0.6	1.04				16.78	1.19	1.04				1.3	[Mat69]
d + ^{9}Be	15.8	65.0	1.25	0.79	7.2	1.25	1.025							1.3	[Cow66]
d + ^{10}B	11.8	78.0	0.921	0.943	30.0	0.867	0.731				6.0	0.921	0.943	1.3	[Fit67]
d + ^{11}B	11.8	78.0	0.981	0.989	30.0	0.759	0.901				5.91	0.981	0.989	1.3	[Fit67]
d + ^{12}C	15.8	63.0	1.25	0.82	8.0	1.25	0.93							1.3	[Cow66]
d + ^{13}C	15.0	98.9	1.05	0.88	10.7	1.76	0.44				4.0	1.0	0.81	1.3	[Bus74]
d + ^{14}N	15.0	95.6	1.05	0.85	6.5	1.76	0.5				5.0	1.0	0.81	1.3	[Bus74]
d + ^{16}O	15.8	100.0	1.25	0.765	15.0	1.225	0.605							1.3	[Cow66]
d + ^{17}O	18.0	85.14	1.15	0.74	3.7	1.55	1.04				4.5	0.9	0.74	1.3	[Li76]
d + ^{19}F	15.0	79.6	1.164	0.821	15.43	0.613	1.583							1.3	[Deh70]

The global potential does a good job reproducing the shape to about 30 degrees which is important for extraction of spectroscopic factors. Beyond 30 degrees, a strong deviation is observed. No apparent trend was easily found in the SFresco fits but on average the global imaginary surface term appears to be ~30% higher than the value determined from the individual fits.

Calculations were performed using the finite-range DWBA code Fresco [Tho88]. Due to the large number of DWBA calculations performed a user-friendly graphical user interface was written by the author to aid in this work. (For more information on the GUI see Appendix I). For the individual (d,n) reactions studied in this work, the unmodified global potential of Daeinick was

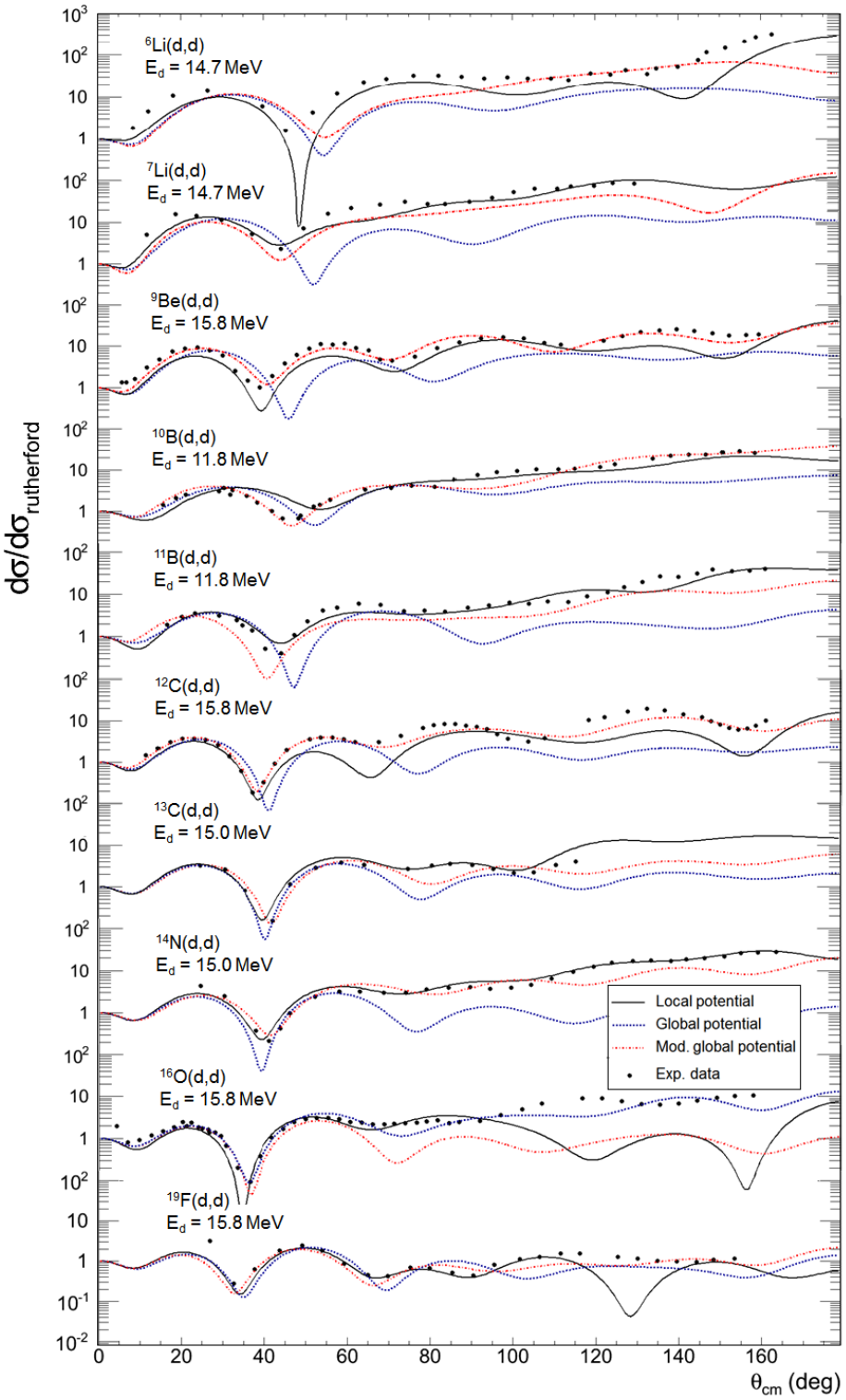

Figure 7.6 – OMP elastic scattering calculations using global, modified global, and local OMPs on various (d,d) elastic data sets (see Table 7.2 for OMPs).

used for the deuteron entrance channel and the Chapel Hill 89 (CH89) global potential [Var91] for the neutron exit channel. For the proton-core potential, a Woods-Saxon shape was used with r_o = 1.25 fm and a = 0.65 fm. The well depth was adjusted to reproduce the single-proton binding energy (S_p). A spin-orbit potential also was included with the same r_o and a_o and V_{so} = 7.0 MeV.

The measured differential cross section for ^{9}Be(d,n)^{10}B is shown in Figure 7.7. The ground state of ^{10}B is $J^{\pi} = 3^{+}$ and for ^{9}Be $J^{\pi} = \frac{3^{-}}{2}$, thus the change in parity according to Equation 4.2 constrains ℓ to odd values. Indeed from Figure 7.7, the DWBA calculation with $\ell = 1$ matches the first peak at ~20°. The ^{9}Be(d,n)^{10}B reaction has been measured by [Par73] at E_d = 16 MeV thus a direct comparison to n-ToF data can be made, as shown in Figure 7.7. Both global and local [Par73] OMP DWBA calculations are included.

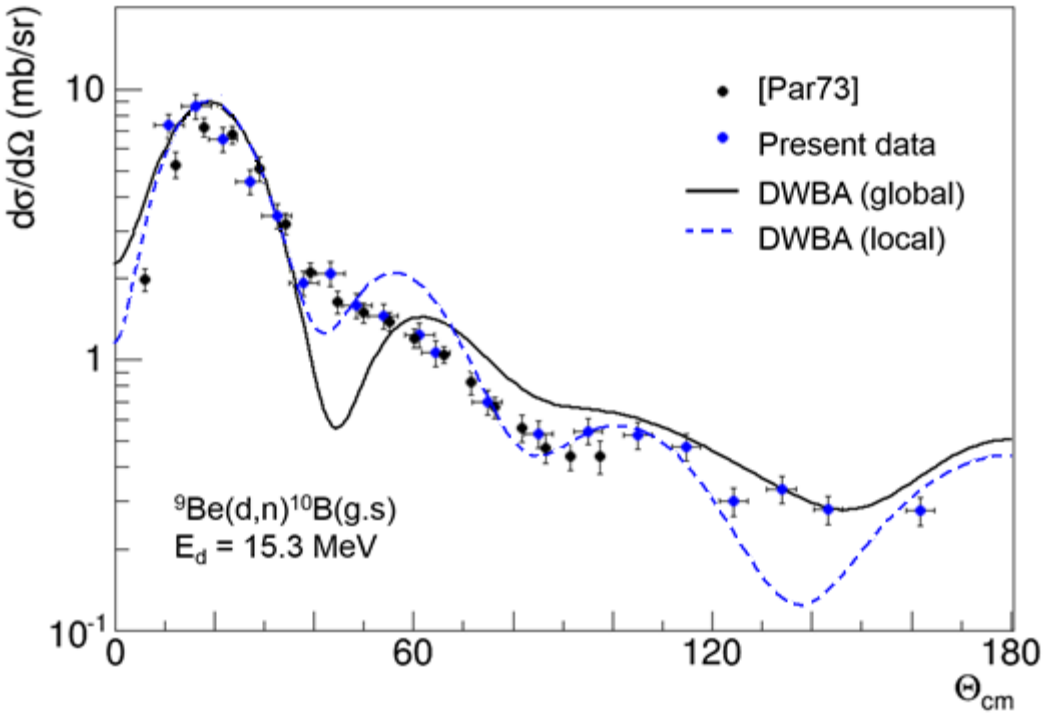

Figure 7.7 – Measured ^{9}Be(d,n)^{10}B(g.s) cross section compared to the data of [Par73] with global and local OMP DWBA calculations

The local potential better describes the overall shape of the differential cross section, which is not surprising as it is fit from specific incoming and outgoing elastic scattering data. As mentioned,

this practice is typically not useful in systematic studies as it is difficult to determine trends in the spectroscopic data between different nuclei.

The measured differential cross section for $^{11}B(d,n)^{12}C$ is shown in Figure 7.8. As with $^{9}Be(d,n)^{10}C$, the change in parity constrains possible ℓ values to odd values which agrees with the DWBA calculation with $\ell = 1$. Not surprising, the DWBA calculation does not fit the shape of the differential cross section very well but does match the overall downward trend of the differential cross section. Similar conclusions were seen in the data of [Fuc67] at E_d = 6.0 MeV. The increase in cross section at 140 degrees is most likely due to non-direct compound nuclear cross section contributions, which would then also contribute of forward angles perhaps smoothing out the differential cross section.

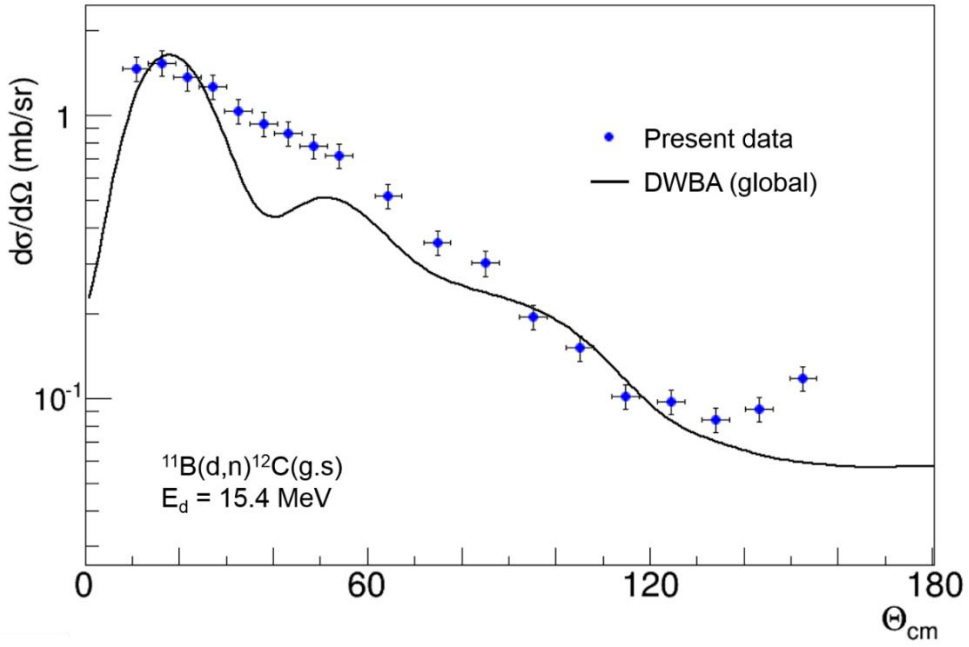

Figure 7.8 - Measured $^{11}B(d,n)^{12}C(g.s)$ cross section with global OMP DWBA calculations

The $^{13}C(d,n)^{14}N$ and $^{14}N(d,n)^{15}O$ differential cross sections are shown in Figures 7.9 and 7.10. DWBA calculations agree with data at small angles for $\ell = 1$ transfers. The DWBA calculation poorly describes the complete shape of the data for $^{14}N(d,n)^{15}O$ but is better in the case of $^{13}C(d,n)^{14}N$. In all the cases shown, improvements are possible with more advanced forms of analysis such as adiabatic deuteron breakup approximations and coupling to strongly populated states but that level of analysis is not needed to demonstrate the capabilities of the UM-DSA.

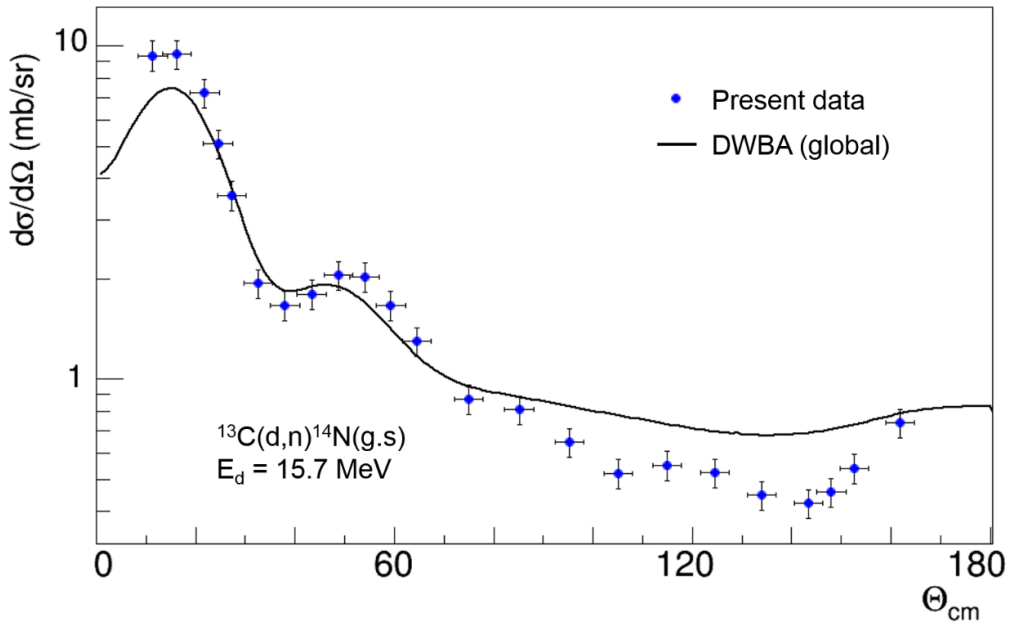

Figure 7.9 - Measured ^{13}C(d,n)^{12}N(g.s) differential cross section compared with global OMP DWBA calculations

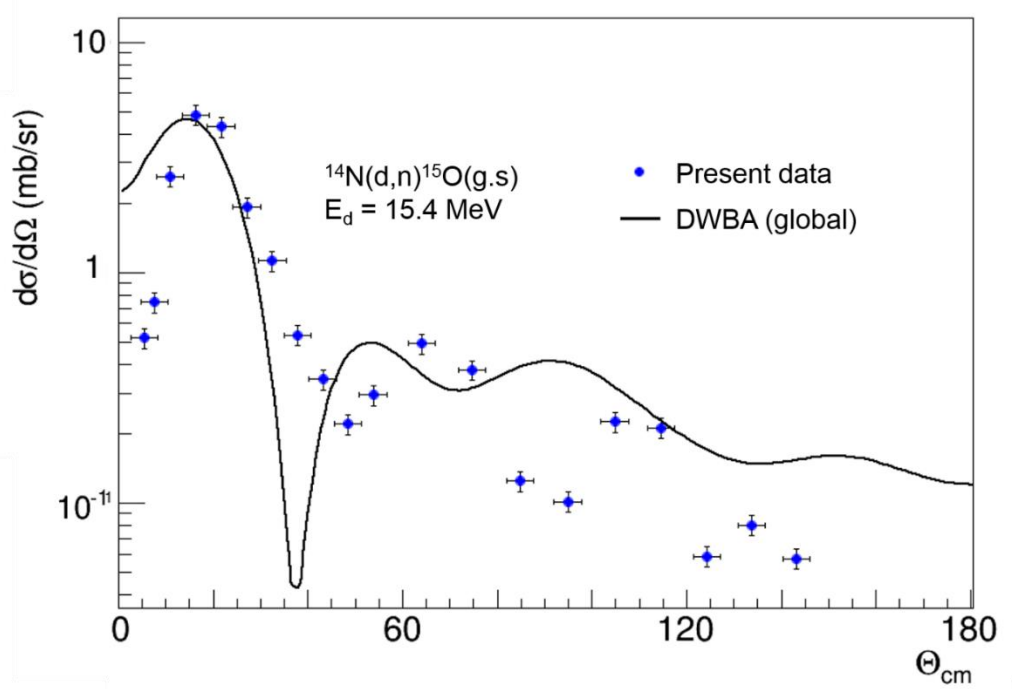

Figure 7.10 - Measured ^{14}N(d,n)^{15}O(g.s) differential cross section compared with global OMP DWBA calculations

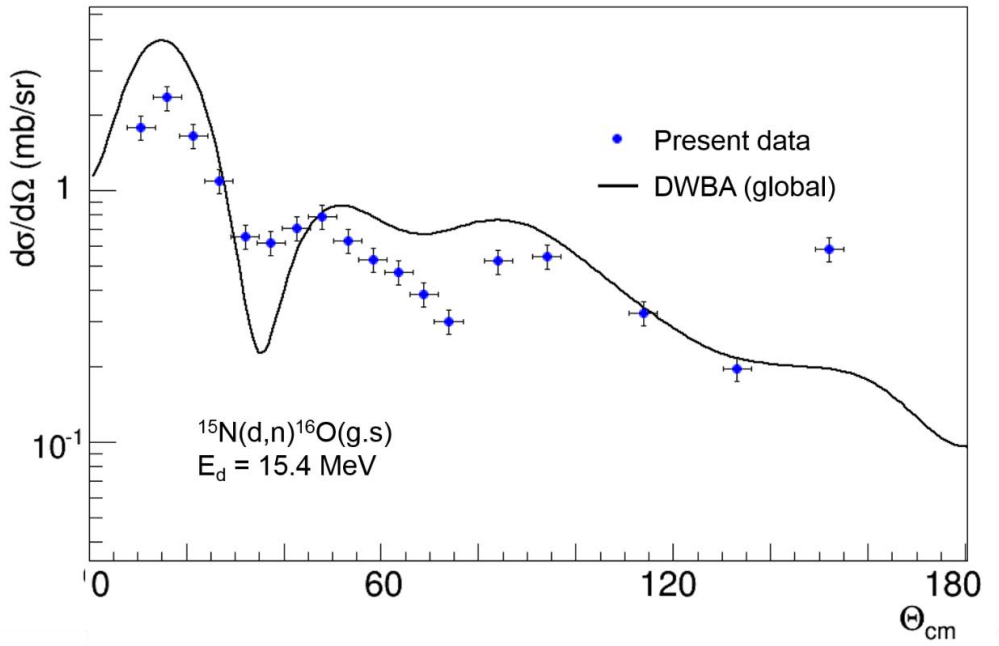

Figure 7.11 - Measured $^{15}N(d,n)^{16}O(g.s)$ differential cross section compared with global OMP DWBA calculations

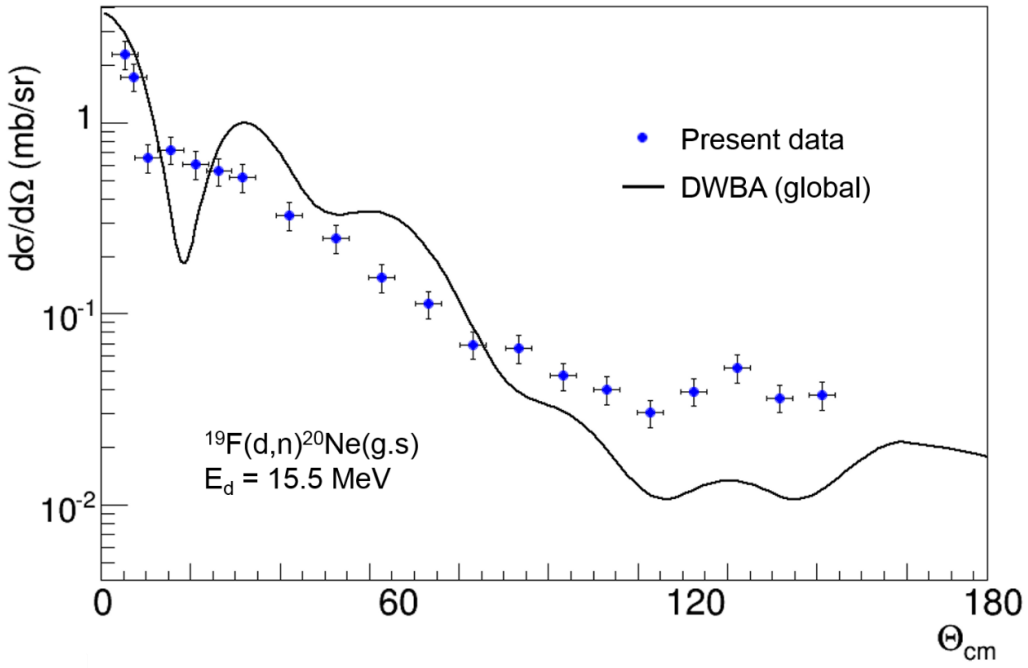

Figure 7.12 - Measured $^{19}F(d,n)^{20}Ne(g.s)$ differential cross section compared with global OMP DWBA calculations

Differential cross section for the ^{15}N(d,n)^{16}O and ^{19}F(d,n)^{20}Ne reactions are shown in Figures 7.11 and 7.12. As expected, both cross sections agree at forward angles with DWBA calculations for $\ell = 1$ and $\ell = 0$ transfers, respectively.

5. Spectroscopic factors

As shown in Chapter 4, a useful quantity which may be extracted from a measured (d,n) differential cross section is the spectroscopic factor. In the present measurements these have an uncertainty estimated to be ±15 % arising mainly from the uncertainty in neutron detection efficiency and the spectrum unfolding process.

The square root of the spectroscopic factor for single-nucleon transfer reactions, known as the spectroscopic amplitude, is directly proportional to the matrix elements of the formation of the single-particle state. The spectroscopic factors for each target were extracted using the data points from 0 – 30^0 degrees. This choice of angular range was based on the DWBA and global OMP trends shown in Figure 7.6, and the results are reported in Table 7.3. Where data exists at 16.0 MeV, the results using a local OMP are also included in addition to those using the global OMP. The ^{9}Be(d,n)^{10}B reaction again provides a test case for direct comparison with published results.

Table 7.3 – Ground-state spectroscopic factors

Final nucleus	J^π, T	nlj	ℓ_p	Present work[1]		Previous measurements		
				Global	Local	(d,n)	E_d (MeV)	Ref.
^{10}B	3^+, 0	$1p_{3/2}$	1	1.21	1.35	1.33	16.0	[Par73]
^{12}C	0^+, 0	$1p_{3/2}$	1	3.58	-	4.18	11.8	[Mut71]
^{14}N	1^+, 0	$1p_{1/2}$	1	1.17	-	2.18	11.8	[Mut71]
^{15}O	½$^-$, 0	$1p_{1/2}$	1	1.11	-	1.00	6.0	[Bom71]
^{16}O	0^+, 0	$1p_{1/2}$	1	2.63	-	3.7	6.0	[Boh72]
^{20}Ne	0^+, 0	2s	0	0.45	-	0.4	6.5	[Bar67]

[1] Estimated uncertainty is ±15 %.

The ground-state spectroscopic factor using the local potential of [Par73] shows very good agreement with the spectroscopic factor reported by [Par73], but the spectroscopic factor is

approximately 10% lower in my measurement using the global OMP. This discrepancy is not surprising since these reactions are out of the range of the global potential [Dae80]. As shown in the previous section, the difference is primarily due to an over prediction of the DWBA strength arising from the global OMP absorptive surface potential being used.

For the nuclei for which no local potentials were available, the spectroscopic factors extracted using global OMPs agreed well within the uncertainties with spectroscopic factors extracted from n-ToF data. The overall trend again shows lower values using the global OMPs vs. local OMPs. These results are quite important to the overall characterization of the array as they are a measure of the ability to measure absolute cross sections over a range of neutron energies with the proper normalization. The greatest source of uncertainly is the neutron efficiency and the uncertainties in the spectrum unfolding algorithm which were estimated to be 10% each for a total uncertainly of ±15 %.

II. The (^{3}He,n) Reaction

As mentioned, the (^{3}He,n) reaction provides another important set of test reactions for evaluation of the UM-DSA. Thus angular distributions were measured at E = 16 MeV between 10 and 170 deg. (lab) for ^{12}C(^{3}He,n) which has been previously measured at E(^{3}He)=16 MeV [Fen78]. A list of experimental details and uncertainties are tabulated in Table 7.4. The solid angle of each detector was determined using Monte Carlo calculations. Detection efficiency was again determined using MCNP-PoliMi [Poz03]. Care was taken to accurately model the reaction chamber since the gold beam stop was located inside the reaction chamber. As with the (d,n) reactions studied, typical data acquisition time was 30 minutes per angle.

Table 7.4 – Experimental details and uncertainties for the (^{3}He,n) measurements

Target	Mean beam energy[1] (MeV)	Lab angular range (deg)	Detector solid angle (10^{-3} sr)	Angular acceptance (deg)	Target thickness (mg/cm^2)	Uncertainties	
						Solid angle (%)	Target thickness (%)
^{12}C	15.89	0 - 170	49.1	14.48	0.400	1	1

[1]Mean beam energy is defined as beam energy at half target thickness

1. The $^{12}C(^{3}He,n)^{14}O$ reaction data

A detailed analysis of the $^{12}C(^{3}He,n)^{14}O$ reaction has been performed at E(^{3}He) = 10 – 22 MeV using n-ToF [Fen78] which allows for a direct comparison with my data. Spectra from the $^{12}C(^{3}He,n)^{14}O$ reaction were extracted using the procedure of §5.6 and each spectrum was unfolded using the MLEM algorithm.

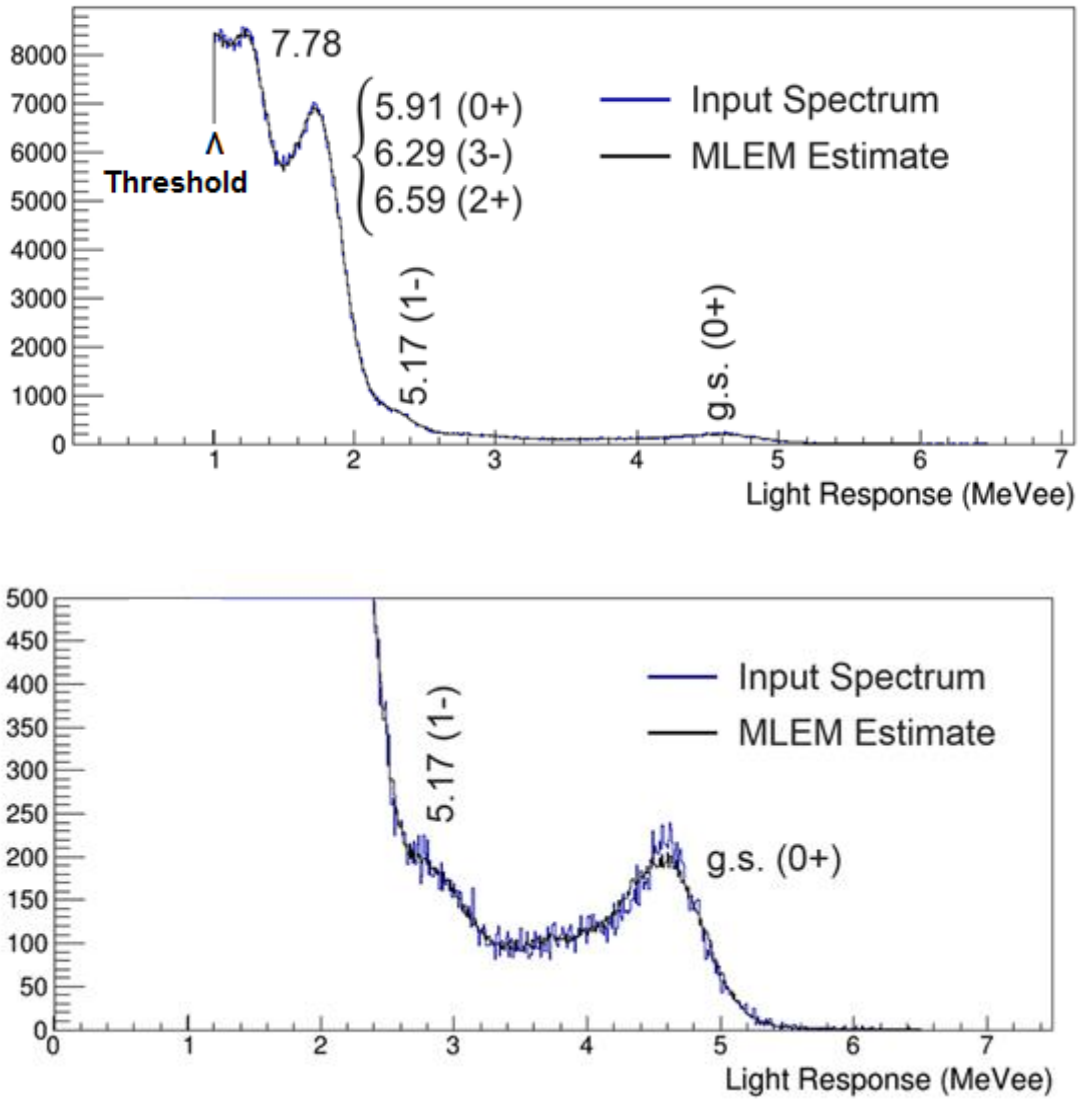

Figure 7.13 – Light-response spectrum and MLEM estimate at 5° lab for the $^{12}C(^{3}He,n)^{14}O$ reaction at E(^{3}He) = 16 MeV. Software threshold indicated.

The light-response spectrum at 5° lab is shown in Figure 7.13 and the unfolded spectrum in Figure 7.14. The MLEM estimate fits the input spectrum quite well with virtually no spurious peaks generated as was observed in the (d,n) data. Spectrum unfolding was not able to separate the triplet peak primary due to the resolution of the detector, but is clearly higher resolution than the n-ToF data of [Fen78]. Beyond 90° lab, the MLEM method was not able to reliably extract useable direct-reaction neutron spectra from the light-response data. This is most likely due to the inclusion of a strong neutron continuum from compound-nuclear reactions which predominate at backward angles.

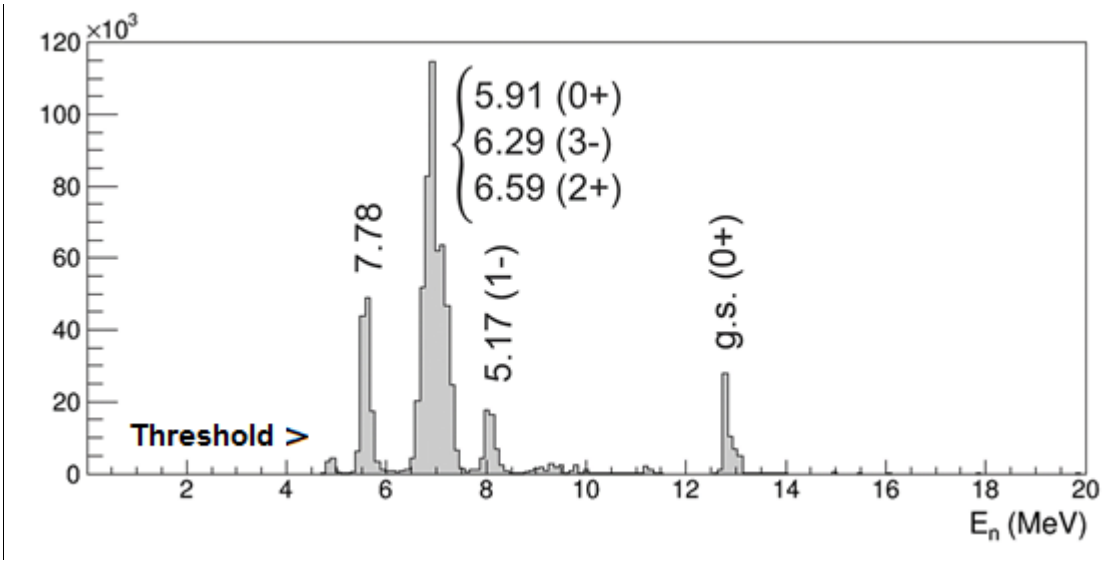

Figure 7.14 - Unfolded neutron spectrum at 5° lab for the $^{12}C(^{3}He,n)^{14}O$ reaction at E(^{3}He) = 16 MeV (software threshold at E_n ~ 5 MeV). Software threshold indicated.

This brings a potential challenge which future systems will need to address. From these unfolded spectra, the cross section for the ground state, 5.17 MeV, and 7.78 MeV excited states were extracted. A summed cross section for the triplet state was extracted by integrating over the entire peak. This also was done by [Fen78]. Differential cross sections compared to the data of [Fen78] are shown in Figure 7.15.

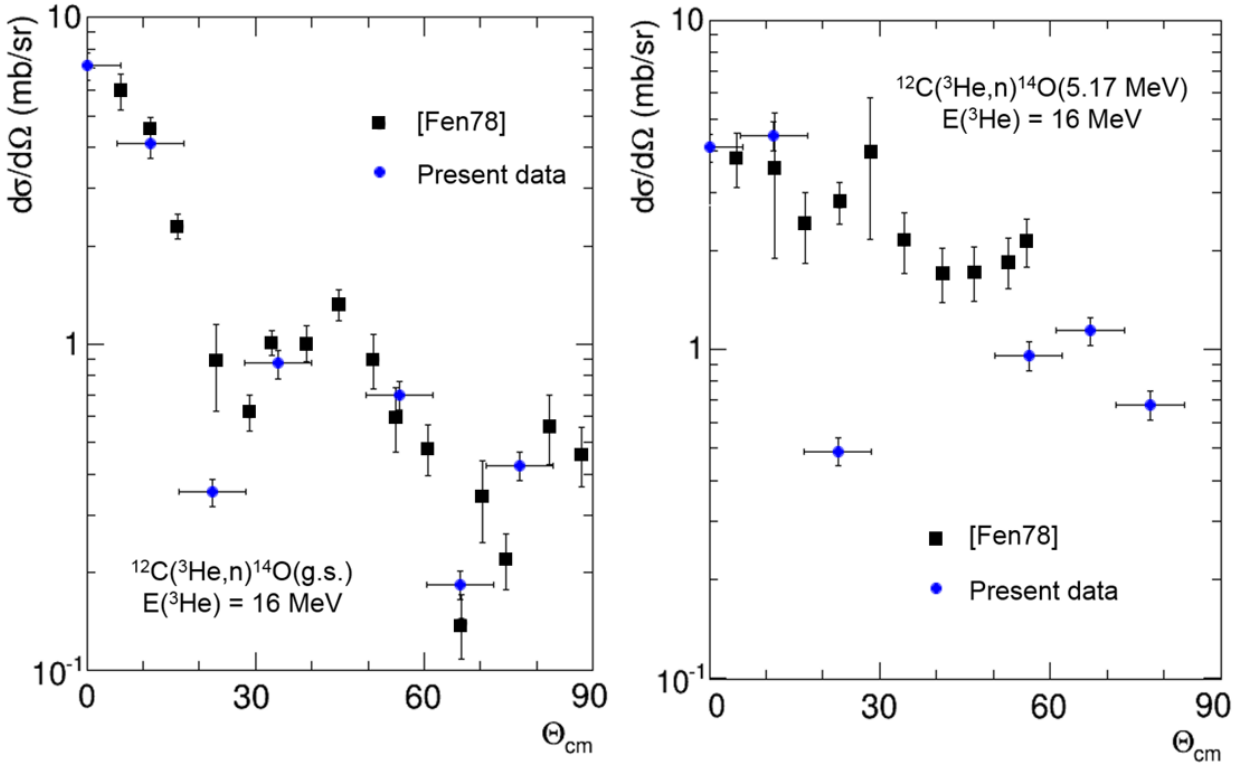

Figure 7.15 - Ground state and 5.17 MeV state differential cross sections for the $^{12}C(^{3}He,n)^{14}O$ reaction at E(^{3}He) = 16 MeV compared to the data of [Fen78] at E(^{3}He) = 16 MeV.

Good agreement is generally shown between the present data using spectrum unfolding and the n-ToF data at similar energies previously measured, agreement not only in absolute normalization but also overall shape. The large angular error bars for our data are due to the close detector-target distance chosen for the reaction. As noted, the beam was stopped inside the reaction chamber in order to obtain a measurement at 0 degrees. This resulted in a *very* high flux of gamma rays associated with the stopping of the beam, which was less than 50 cm from the detector. Even in these harsh conditions, the UM-DSA using DPSD algorithm was able to separate n/γ's, extract usable light-response spectra, and then successfully using MLEM unfolding to extract incident neutron spectrum. This demonstrates the robustness of the array for measurements in intense gamma-ray fields.

III. The $^{13}C(\alpha,n)^{16}O$ Reaction

So far all the reactions evaluated involved relativity high-energy neutrons (i.e. $E_n > 10$ MeV). In contrast, the study of nuclear astrophysics reactions require very low bombardment energies and often result in low outgoing recoil particle energies. In terms of reactions which require the measurement of an outgoing neutron, the classical example (which still has not been measured at very low bombardment energies!) is the $^{13}C(\alpha,n)^{16}O$ reaction. The reaction serves as the main neutron source for the slow neutron capture process (s-process). The positive reaction Q-value (Q = 2215 keV, [ENDF/B-VII.0]) means outgoing neutrons will have energy high enough for n/γ discrimination even at very low bombardment energies. The minimum n/γ separation energy threshold is a major limiting factor in the measurement of other outgoing neutrons in astrophysical reactions such at $^{22}Ne(\alpha,n)^{24}Mg$ which has a negative Q-value (-478 keV, [ENDF/B-VII.0]). Experimental details and uncertainties for the present measurements are given in Table 7.5. Typical data acquisition times were approximately 30 - 60 minutes per α beam energy and the γ/n ratio was ~1000:1 throughout the measurements so good DPSD was essential.

Table 7.5 – Experimental details and uncertainties for the (α,n) measurements

Target	Mean beam energy[1] (MeV)	Lab angular range (deg)	Detector solid angle (10^{-3} sr)	Angular acceptance (deg)	Target thickness (mg/cm^2)	Uncertainties	
						Solid angle (%)	Target thickness (%)
^{13}C	varied	45	1.34	2.42	0.200	1	1

[1]Mean beam energy is defined as beam energy at half target thickness

1. The $^{13}C(\alpha,n)^{16}O$ reaction spectra

As with the (d,n) and (^{3}He,n) reactions, spectra from the $^{13}C(\alpha,n)^{16}O$ reaction were extracted using the procedure of §5.6 and each spectrum was unfolded using the MLEM algorithm. In the case of reactions of astrophysics interest which are often statistics limited at low energies, as stated the MLEM algorithm provides an ideal method for unfolding since it accounts for the Poisson nature of the noise in a measurement. A sample raw light-response spectrum at E_α= 7.5 MeV is shown in Figure 7.16 with the 0^+ and 3^- states in ^{16}O labeled. An important observation from

Figure 7.16 is that states of interest are clearly identifiable form the raw light-response spectra alone. This is a huge advantage over ^{3}He, BF_3, and other neutron counters typically used for astrophysics measurements which provides little or no information on neutron energy. Here, no *a priori* information was needed to obtain reliable and repeatable unfolded neutron energy spectra. The MLEM worked well even with very low statistics per bin as the case for the high light-response region of the ground-state recoil peak shown in Figure 7.16.

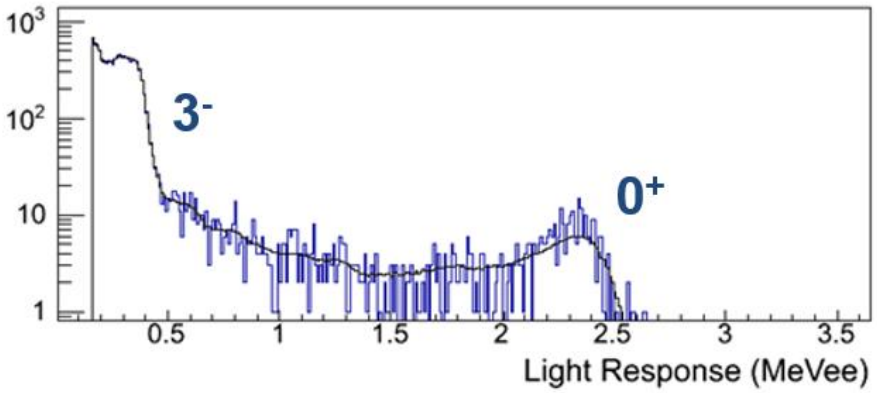

Figure 7.16 – Raw light-response spectrum from the $^{13}C(\alpha,n)^{16}O$ reaction at E_α= 7.5 MeV, θ = 45^o (lab).

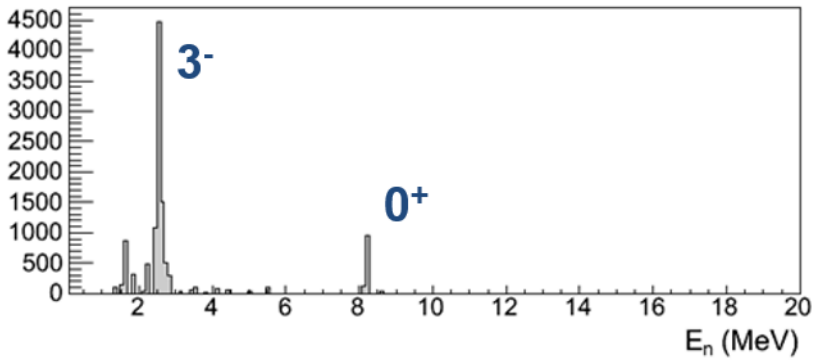

Figure 7.17 – Unfolded neutron energy spectrum from the $^{13}C(\alpha,n)^{16}O$ reaction at E_α= 7.5 MeV, θ = 45^o (lab).

The MLEM unfolded spectrum of Figure 7.16 is shown in Figure 7.17. In all, 21 spectra were unfolded and the peaks observed to shift correctly with incident alpha energy as predicted

from the reaction kinematics. The kinematic shift serves as a visual check for fictitious peaks. Above E_α = 3.9 MeV, the 3^- state can be populated and seems to dominate the cross section below. This can be partially explained by momentum matching since (α,n) reactions prefer population of higher spin states over (d,n) reactions which prefer low spin states. Above E_α = 7 MeV a third neutron peak is observed. A 3D plot of the unfolded spectra is shown in Figure 7.18.

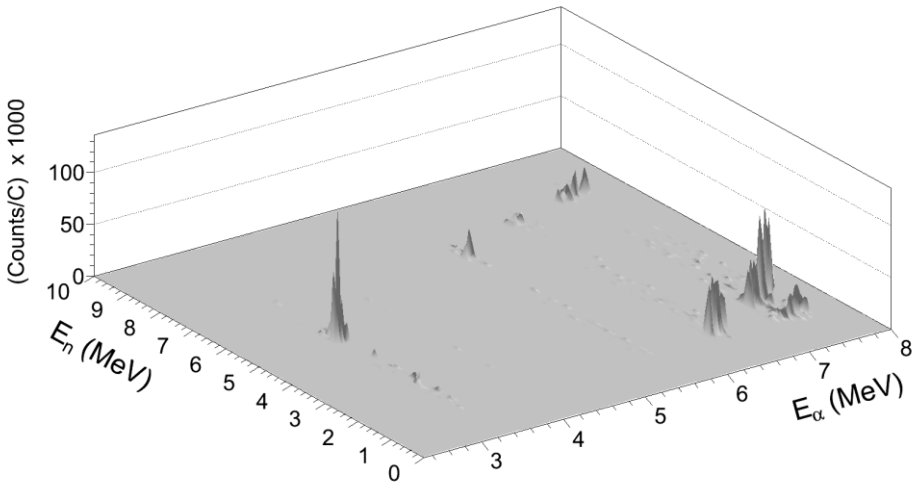

Figure 7.18 – 3D plot of the unfolded specta as function of bombardment energy for the $^{13}C(\alpha,n)^{16}O$ reaction

Integration of the ground-state peak along with the integrated beam current, target thickness, and efficiency, yields the reaction cross section vs. E_α. The measured ground-state cross section as function of energy compared to the absolute total cross section results obtained using a 4π ^{3}He counter is shown in Figure 7.19. Good agreement is observed below the threshold for the 3^- state. Above the threshold, the reaction is dominated by the 3^- state as observed in the Figure 7.18 but not determined with the ^{3}He counter which has no energy information.

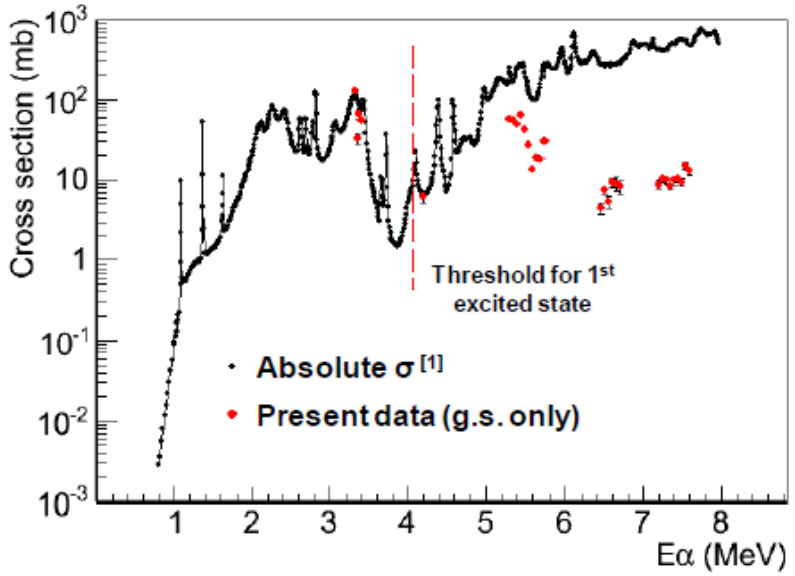

Figure 7.19 – Excitation function of the $^{13}C(\alpha,n)^{16}O$ reaction. [1][Har05]

This demonstration shows that the UM-DSA and in particular deuterated scintillators can reliably and repeatedly be used for cross section measurements without n-ToF. In the field of nuclear astrophysics. This can constrain R-Matrix calculations which in-turn reduces uncertainties in extrapolations down to the very low energy Gamow region [Hei08].

IV. The d(^{7}Be,n)^{8}B Reaction using a Radioactive Ion Beam

The first RIB measurement with the UM-DSA was carried out at the *TwinSol* facility at the University of Notre Dame ISNAP laboratory. The experimental details and uncertainties are listed in Table 7.6. Several 4x6 EJ-315 liquid scinitllators were setup at 6.8, 29.4, 44.0, 59.5, 75.8, and 92.3 degrees (lab). Approximately 120 hours of data was collected over 6 days. As stated in §6.4, signals were taken in triple coincidence with the ^{8}B recoil detector, the beam buncher, and each individual 4x6 EJ-315 scintillator using the VANDLE DAQ and waveform digitizers [Pau14].

A preliminary short-path n-ToF plot is shown in Figure 7.20, and shows all events in blue and the DPSD-gated deuteron recoil events in red. It becomes immediately obvious that this experiment is not possible without the use of effective PSD/DPSD to separate gamma rays and neutrons.

Table 7.6 – Experimental details and uncertainties for the d(^{7}Be,n)^{8}B measurement

Target	Mean beam energy[1] (MeV)	Lab angular range (deg)	Detector solid angle (10^{-3} sr)	Angular acceptance (deg)	Target thickness (mg/cm^2)	Uncertainties	
						Solid angle (%)	Target thickness (%)
C_2D_4	29.8	7-93	8.05	11.60	1.40	1	1

[1]Mean beam energy is defined as beam energy at half target thickness

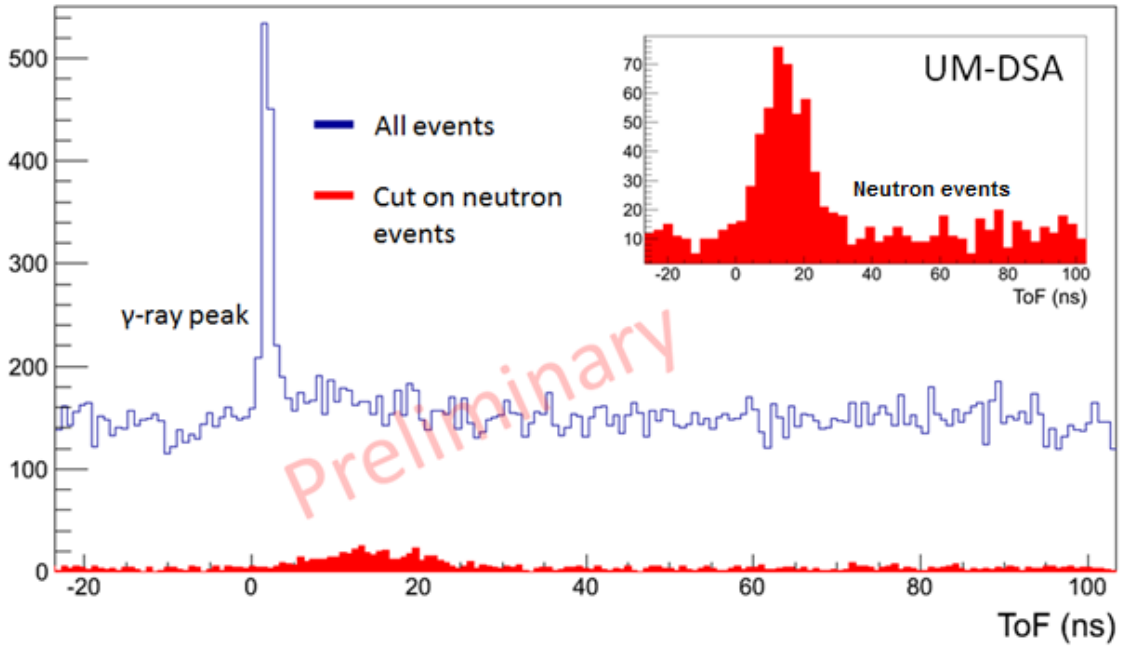

Figure 7.20 – UM-DSA d(^{7}Be,n)^{8}B n-ToF plot showing the effects of DPSD gating

Figure 7.21 shows a DPSD plot for one of the detectors with the ground state peak observed as the higher intensity group of events in the upper neutron band. A deuteron-gated light-response spectrum in coincidence with recoil ^{8}B ions is shown in Figure 7.22. The ground state peak is clearly visible and possibly the first excited state. These results show that neutron spectroscopy using RIBs can be performed without full n-ToF using deuterated scintillators to extract useful information.

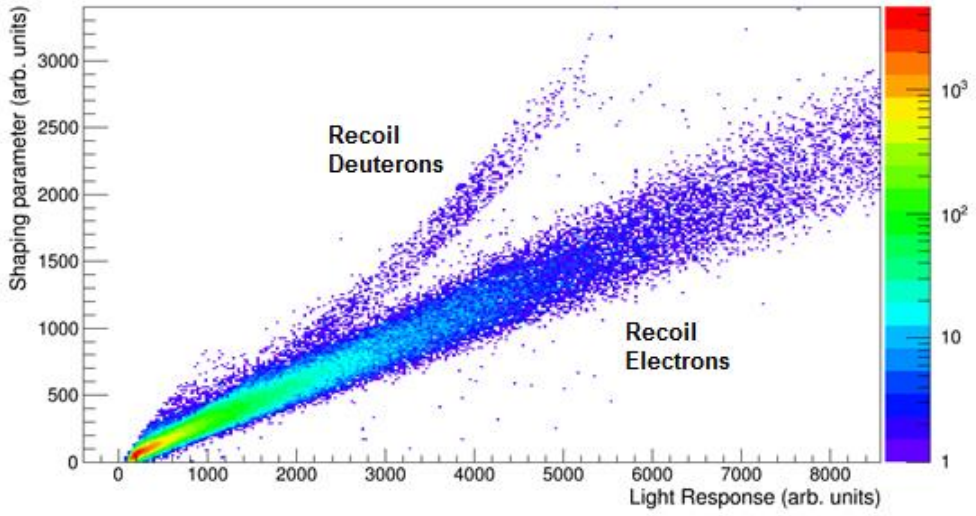

Figure 7.21 – UM-DSA d(^{7}Be,n)^{8}B DPSD plot showing neutron/gamma discrimination.

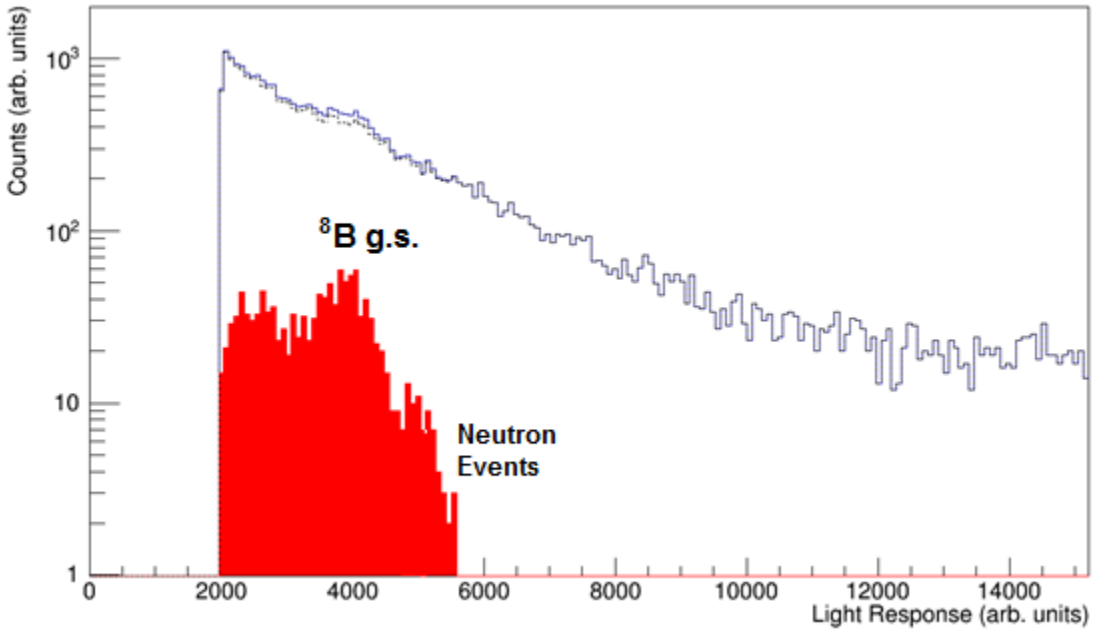

Figure 7.22 – UM-DSA d(^{7}Be,n)^{8}B light-response spectra gated on all events and only coincident deuteron recoils.

This study is currently in the planning stages to measure the full angular distribution using the UM-DSA at forward and back angles. The results shown in this dissertation demostrates that the technique does work with RIBs, which justifies further experiments.

V. Homeland Security Applications

As stated in §6.5, measurements of importance to nuclear safeguards and homeland security typically involve the measurement of continuous neutron spectra like those from spontaneous (SF) and induced fission [Ber04]. As a stand in for special nuclear materials (SNM), a PuBe source was used that produces a similar spectrum to those observed in other SNM measurements. The light-response spectrum from the PuBe measurement is shown in Figure 7.23. From the light-response spectrum alone there are no real signatures of mono-energetic neutron groups as observed in other measurements. This is the first indication that the spectrum is at least somewhat continuous. After processing with the MLEM code, the unfolded result obtained is shown in Figure 2.4. The unfolded result indicates that there is some structure to the neutron spectrum making it distinguishable from a ^{252}Cf SF spectrum [Law14]. This is an interesting and useful result as it demonstrates that spectrum unfolding with deuterated scintillators is capable of distinguishing a neutron spectrum from ^{252}Cf from PuBe for example. Since the PuBe spectrum is the primary the result of (α,n) reactions [Leh68], it is a reasonable prediction that this trend will continue for other (α,n) type sources.

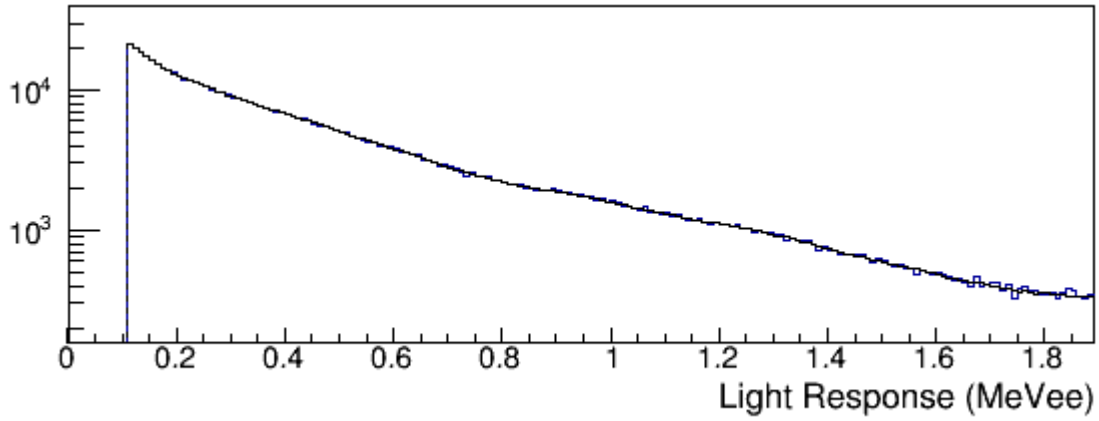

Figure 7.23 – Light-response spectrum from the PuBe measurement using the 5x5 Ej-315M liquid scintillator detector.

Results from [Tom71] and [Jon68] are shown in Figure 7.24 which was adapted from [Tom71]. The y-axis of Figure 7.24 was arbitrary normalized. Good agreement is observed

between the relative positon of the unfolded peaks and the peaks observed by [Tom71] and [Jon68]. Again, the spectrum is distinguishable from the unfolded SF neutron spectrum of [Law14] allowing for possible identification of specific SNM sources. This demonstrates the potential for nuclear safeguard applications of deuterated scintillators as also confirmed by [Law14].

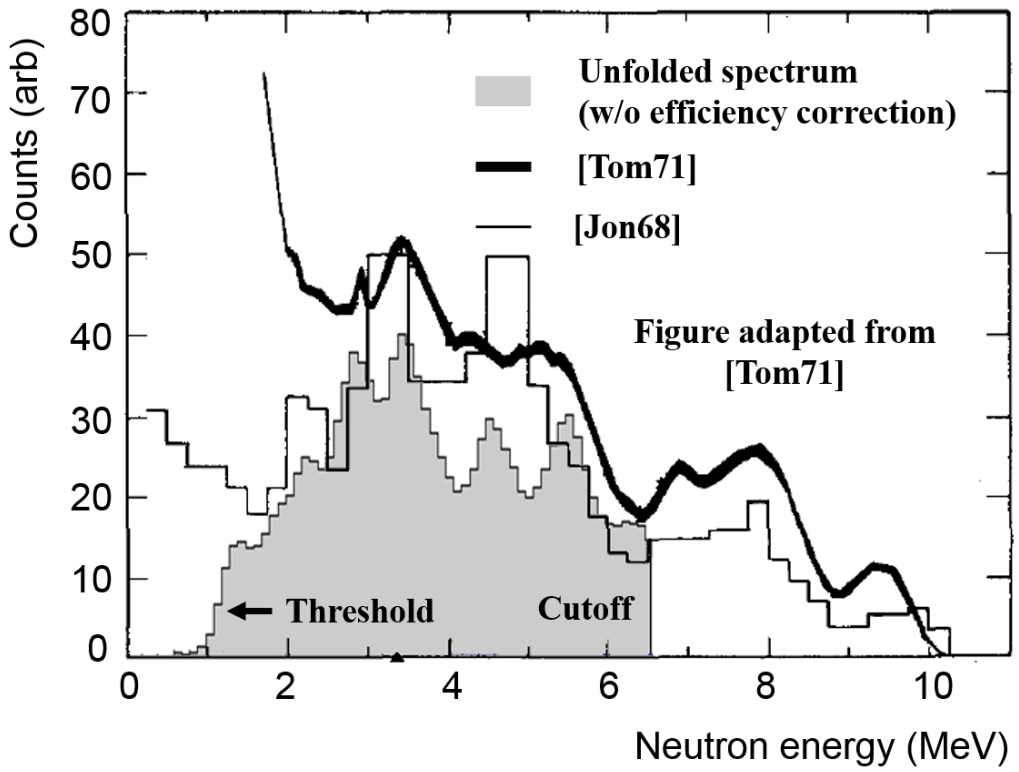

Figure 7.24 – Unfolded PuBe neutron spectrum compared with the results from [Tom71] and [Jon68]. Figure was adapted from [Tom71].

Future nuclear safeguards measurements with other (α,n) sources, measurements of the $^{13}C(\alpha,n)$ reaction, and measurements of the $^{19}F(\alpha,n)$ cross section at a E_α 1 - 8 MeV are planned and the latter experiment has been scheduled. The measured $^{19}F(\alpha,n)$ cross sections can be used to test Monte Carlo calculations to simulate neutron spectra in various geometries and scenarios.

Chapter 8

Conclusion

I. Summary

The use of deuterated scintillators for neutron spectroscopy measurements without the use of n-ToF has been demonstrated for several important applications. All aspects of the UM-DSA neutron spectroscopic system were developed by the author as part of this thesis and the system has been proven to provide a reliable and accurate tool for neutron measurements. ^{9}Be,^{11}B, ^{13}C, ^{14}N, ^{15}N,^{19}F(d,n) cross sections and spectroscopic factors have been determined for various solid and gas targets at E_d = 16 MeV. In the case of ^{9}Be which was previously measured with n-ToF, excellent agreement has been shown between the two techniques in extraction of the cross sections and spectroscopic factors. Spectroscopic factors obtained using the UM-DSA agree well with previous measurements using n-ToF which demonstrates the ability to measure of absolute cross sections. In addition, ^{12}C(^{3}He,n)^{14}O and ^{13}C(α,n)^{14}N cross sections have been measured and again the results agree with previous n-ToF measurements. The MLEM method provides a reliable tool for neutron spectrum unfolding as demonstrated with over 100 unfolded neutron spectra.

Improved organic deuterated scintillators and possibly other scintillating materials with higher resolution would be required for future study of nuclei with higher level densities. These materials of course will require similar unique structures in their light-response spectra for accurate spectrum unfolding. For radioactive beams, the main area of improvement required will be in DPSD down to approximately E_n = 200 keV. As mentioned in the dissertation, this is due to the fact that most RIB reactions must be run in inverse kinematics which results in low-energy neutrons at back angles (forward angles in CM frame of reference). Also, future arrays should use

high-speed parallel processing for DSP as this becomes one of the major limiting factors in real-time data processing during an experiment.

Material in this thesis has been presented in 3 peer-reviewed journal articles on the development and implementation of the UM-DSA system. [Institute of Electrical and Electronic Engineers Transactions of Nuclear Science (IEEE-TNS), European Journal of Physics (EJP), and Nuclear Instruments and Methods (NIMA) (latter currently under review)]. In addition to the journal articles, parts of this work have been presented at the APS Division of Nuclear Physics Fall Meeting (DNP 2011 – 2013), SORMA West (2012), the International Nuclear Physics Conference (INPC 2013), the US Exotic Beam Summer School (EBSS 2013), the APS Spring Meeting *Mini-Symposium on Nuclear Physics: Sensitive Input for Understanding Nucleosynthesis* (APS 2014), and in three invited talks at the University of Notre Dame's Institute for Structure and Nuclear Astrophysics (ISNAP), GSI in Darmstadt, Germany, and Oak Ridge National Laboratory (ORNL).

II. Future work

Future experiments for the UM-DSA have been scheduled at the University of Notre Dame and Oak Ridge National Laboratory. Based on the successful measurements of $^{13}C(\alpha,n)^{16}O$, an experiment is planned to continue the $^{13}C(\alpha,n)^{16}O$ differential cross section measurements down to low E ~300-400 keV energy using the new 5U 100-150 μA high-beam intensity DC accelerator at UND. Since n-ToF will not be possible, the experiment is a perfect match for the UM-DSA. Results will be used to constrain R-Matrix calculations and hopefully reduce uncertainties in extrapolation of the astrophysics S-factor for this reaction down to the Gamow low-energy region [Hei08]. Likewise an experiment to extend the initial measurement of $d(^{7}Be,n)^{8}B$ done here is planned.

At ORNL, the UM-DSA will be used along with the VANDLE array [Pau14] for a $^{19}F(\alpha,n)^{22}Na$ measurement using a ^{4}He gas target. The two independent measurements will be compared and used for determination of the excitation function for the $^{19}F(\alpha,n)^{22}Na$ reaction, which is of importance to nuclear safeguards applications.

APPENDICES

Appendix A – Detector Diagrams

I. 5x5 EJ-315MOD

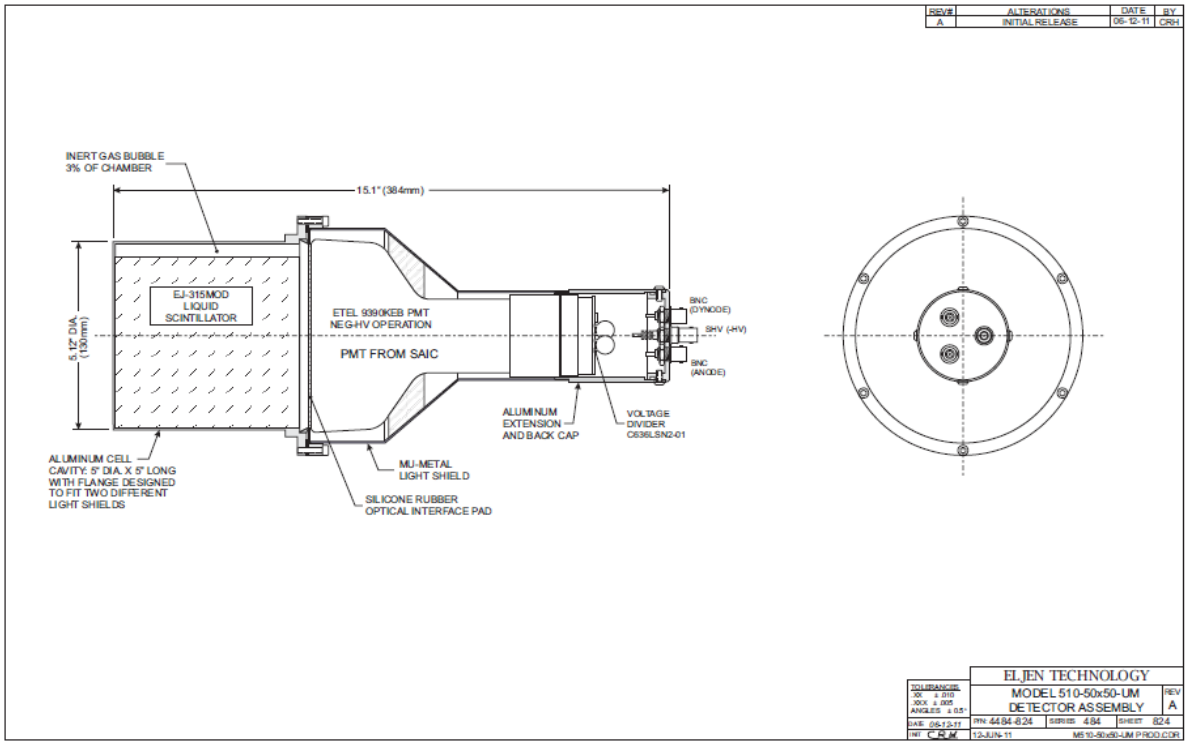

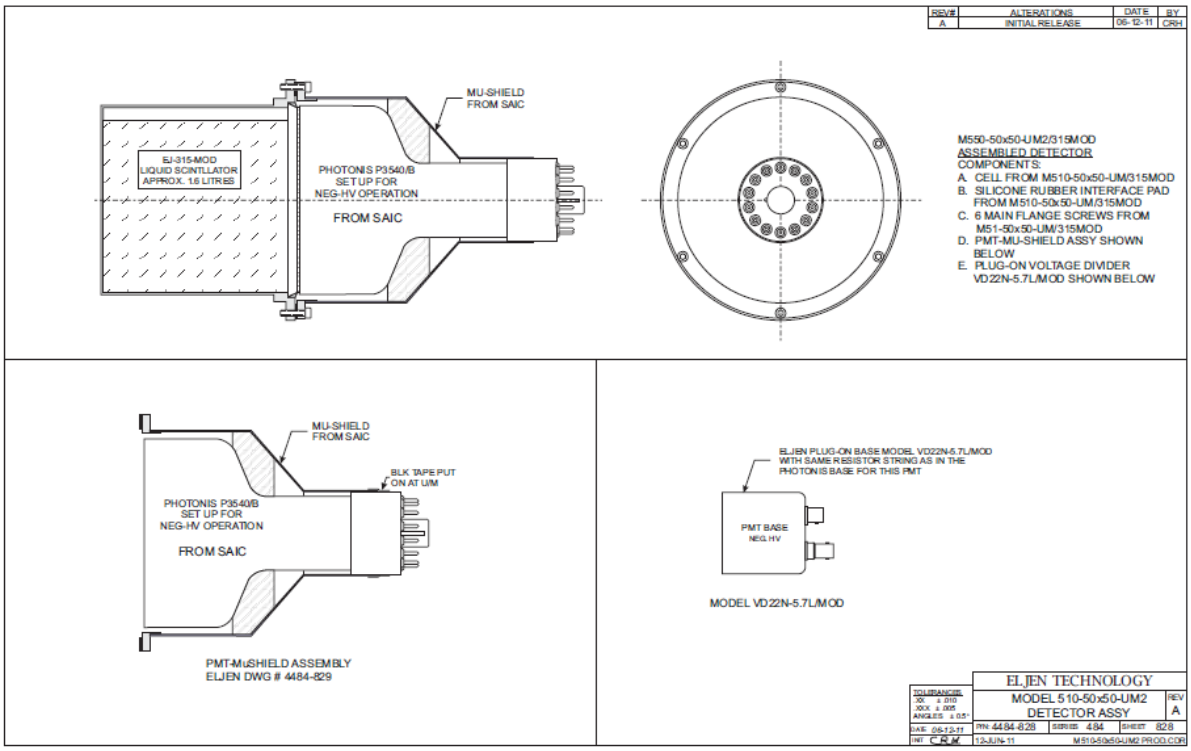

II. 4x6 EJ-315 / EJ-315H / EJ-315MOD

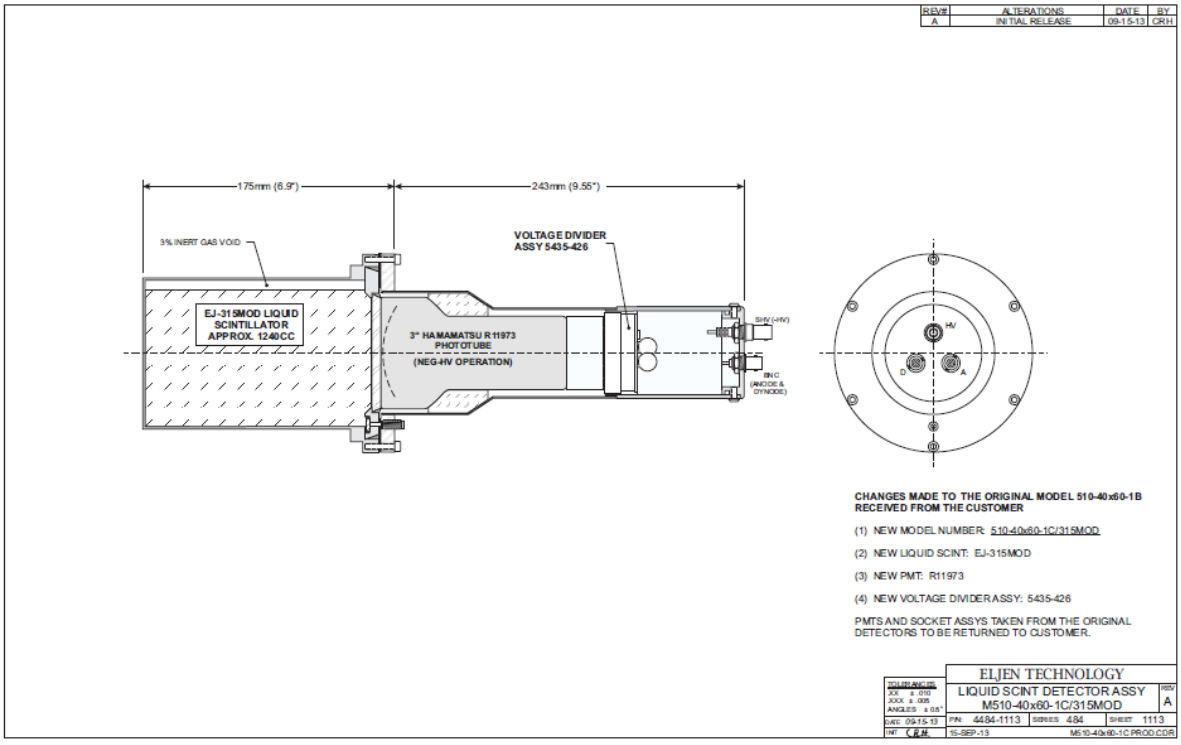

III. 2x2 EJ-315 / EJ-315H

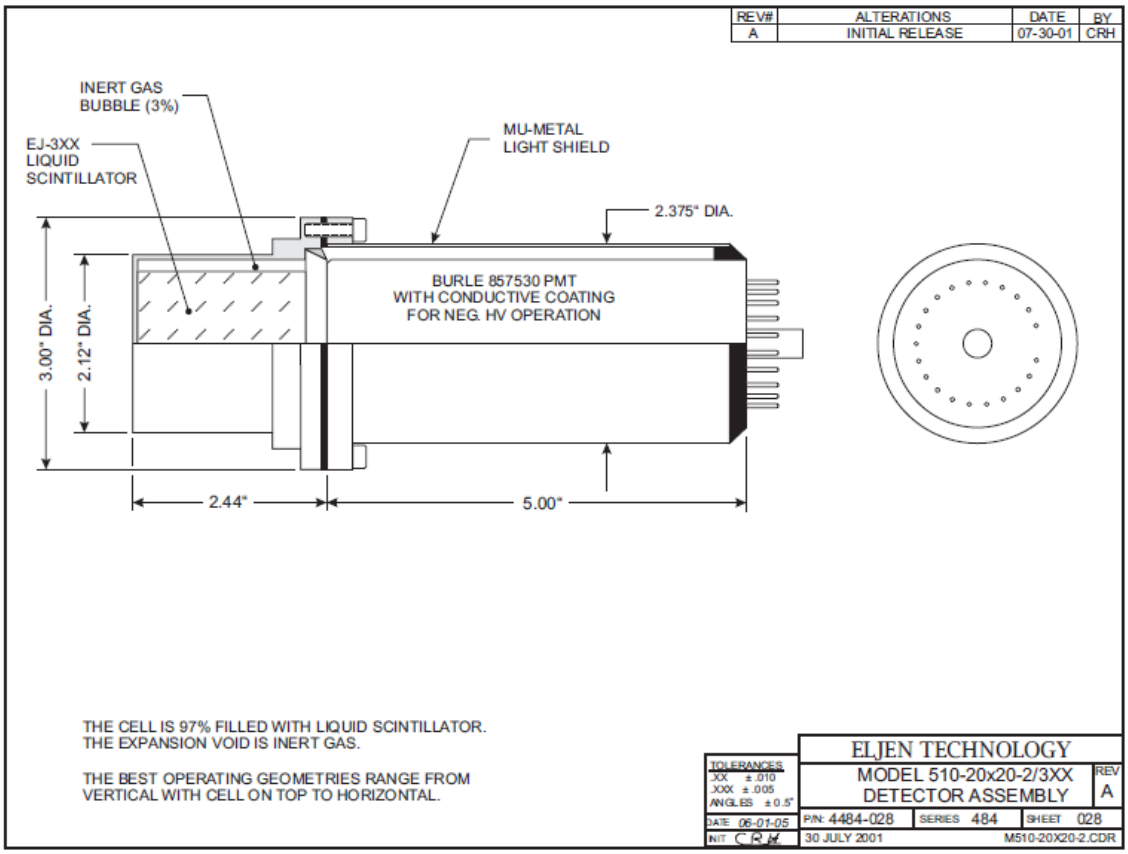

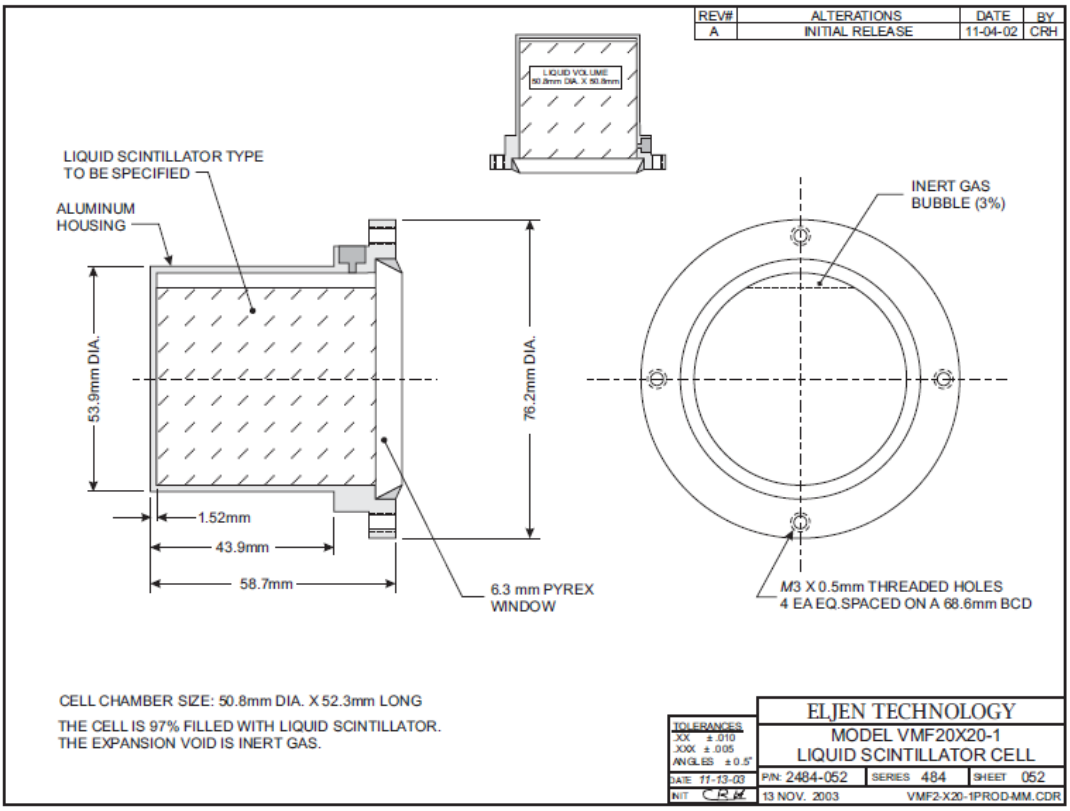

IV. EJ-315 Two-sided

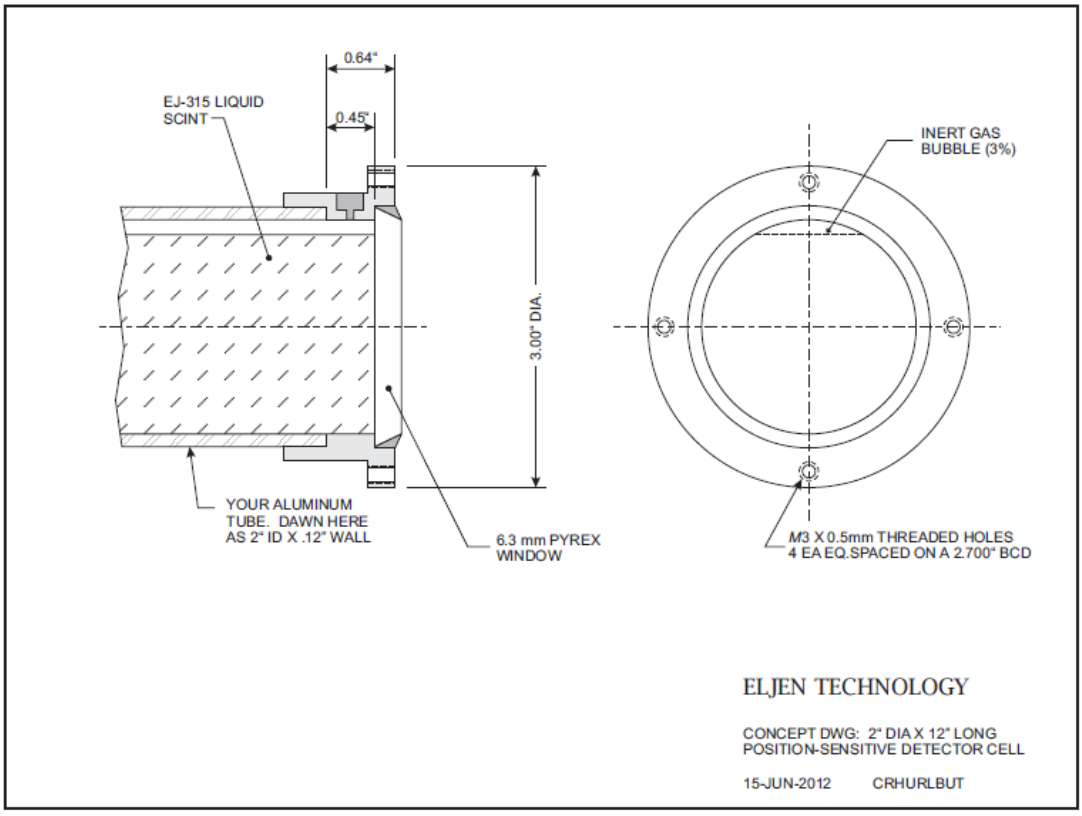

Appendix B – Eljen Scintillation Table

TABLE OF PHYSICAL CONSTANTS OF SCINTILLATORS

	Scintillator Material	Type	Light Output Percent Anthracene	Wavelength of Maximum Emission nm	Decay Constant Main Component ns	Loading loading Element (% by wt.)	Typical Light Attenuation Length cm	H : C Atomic Ratio	Refractive Index	Softening or Flash Point °C	Density	Principal Applications	Commercial Equivalents	
													Saint Gobain	NE
PLASTIC	EJ-200	Plastic	64	425	2.1	.....	380	1.104	1.58	75	1.02	Best overall general properties, TOF Counters, Large Area	BC-408	Pilot F
	EJ-204	Plastic	68	408	1.8	.....	160	1.107	1.58	75	1.02	Good general properties, Use with green WLS	BC-404	NE-104
	EJ-208	Plastic	60	434	3.3	.....	400	1.104	1.58	75	1.02	Good general Properties, Large area, protons, electrons.	BC-412	NE-110
	EJ-212	Plastic	65	423	2.4	.....	250	1.103	1.58	75	1.02	General Purpose, Thin Films, alpha, beta, gamma, and fast neutrons	BC-400	NE-102A
	EJ-228	Plastic	67	391	1.4	.....	N/A	1.107	1.58	75	1.02	Ultra fast timing, High pulse pair resolution	BC-418	Pilot U
	EJ-230	Plastic	64	391	1.5	.....	120	1.104	1.58	75	1.02	Variant EJ-228, optimized for detector dimensions≥10cm	BC-420	Pilot U2
	EJ-232	Plastic	55	370	1.4	.....	N/A	1.102	1.58	75	1.02	Ultra fast timing, use with blue WLS	BC-422	NE-111A
	EJ-240	Plastic	41	435	~230	.....	240	1.109	1.58	75	1.02	Long decay time, Phoswich detectors	BC-444	NE-115
	EJ-244	Plastic	56	435	3.3	.....	270	1.104	1.58	99	1.02	Elevated temperatures, Analog to EJ-208, General purpose	BC-440	
	EJ-248	Plastic	60	425	2.1	.....	250	1.104	1.59	99	1.049	Elevated temperatures, Analog to EJ-200, General purpose	BC-448	
	EJ-252	Plastic	46	423	2.4	.....	N/A	1.098	1.58	75	1.037	Dosimetry, Water-equivalent	BC-470	NE-105
	EJ-260	Plastic	60	490	9.2	.....	350	1.109	1.58	75	1.02	Green Emitting Scintillator	BC-428	NE-103
	EJ-280	Plastic	.....	490	9.2	.....	350	1.11	1.58	75	1.02	Green Wave Length Shifter	BC-482A	
	EJ-284	Plastic	.....	608	14	.....	N/A	1.11	1.58	75	1.02	Red Wave Length Shifter	BC-482A	
	EJ-290	Resin	60	423	2.4	.....	N/A	1.103	1.58	75	1.02	Scintillator Casting Resin, General Purpose, beta, gamma, and fast neutrons	BC-490	NE-120
LIQUID	EJ-301	Liquid	78	425	3.2 [3]	.....	.....	1.212	1.505	26	0.874	PSD Liquid, Fast neutron-gamma discrimination	BC-501A	NE-213
	EJ-305	Liquid	80	424	2.5	.....	.....	1.331	1.505	47	0.877	High light output, Fast neutron and gamma rays, Cosmics	BC-505	NE-224
	EJ-309	Liquid	75	424	3.5 [3]	.....	.....	1.25	1.57	144	0.964	PSD Liquid, Fast neutron-gamma discrimination, High Flash Point, Low Chemical Toxicity, compatibility with acrylic plastics.		
	EJ-313	Liquid	20	424	3.1	F	.....	0.0035	1.377	10	1.61	Hydrogen-free, Neutron studies, Fast neutron and gamma rays	BC-509	NE-226
	EJ-315	Liquid	60	425	3.5	D	.....	0.99 (D:C)	1.498	-11	0.954	Deuterated benzene, Neutron studies	BC-537	NE-230
	EJ-321L	Liquid	39	424	2	.....	>5 meters	2.01	1.47	102	0.86	Mineral oil based, Standard efficiency, Large tanks, Fast neutron and gamma rays, Cosmic rays	BC-517L	NE-235L
	EJ-321H	Liquid	52 [2]	424	2	.....	>5 meters	1.89	1.48	81	0.86	Mineral oil based, High light output, Fast neutron and gamma rays, Cosmic rays, Large tanks	BC-517H	NE-235H
	EJ-325	Liquid	60	424	4	.....	.....	1.73	1.49	74	0.875	Mineral oil based, Pulse shape discrimination, Fast neutron and gamma discrimination, Large tanks	BC-519	NE-235C
LOADED	EJ-254	Loaded Plastic	32	425	2.2	B (5%)	120	1.169	1.58	60	1.026	Boron Loaded	BC-454	
	EJ-256	Loaded Plastic	32	425	2.1	.....	N/A	1.134	1.58	75	1.08	Lead loaded (≤5% standard), X-rays, Dosimetry	BC-452	NE-142
	EJ-331	Loaded Liquid	60	424	4	Gd (to 1%)	.....	1.31	1.5	44	0.89	Highest light output Gd loaded, Neutron spectrometry, Neutrinos	BC-521	NE-323
	EJ-335	Loaded Liquid	56	424	3.8	Gd (to .5%)	.....	1.57	1.49	64	0.88	Mineral oil base,Gd loaded for large tanks, Neutron spectrometry Neutrinos	BC-525	
	EJ-339A	Loaded Liquid	65	424	3.7	^{10}B (5%)	.....	1.67	1.411	8	0.98	^{10}B loaded, Pulse shape discrimination, Neutron spectrometry, Thermal neutrons	BC-523A	NE-321A
	EJ-351	Dioxane Based	65	425	3.8	.....	.....	1.65	1.44	12	1.036	Dioxane based cocktail for Aquaous samples	BC-220	NE-220

[1] **Plastics**- 1 MeV of energy deposited in EJ-200 from an energetic electron produces approximately 10,000 blue photons

[1] **Liquid**- 1 MeV of energy deposited in EJ-301 from an energetic electron produces approximately 12,000 blue photons

[3] The mean decay times of the first 3 components are 3.16, 32.3, and 270 ns.

Rev. 5/13/08

Appendix C – Photomultiplier Data Sheets

HAMAMATSU
PHOTON IS OUR BUSINESS

PHOTOMULTIPLIER TUBE R1250

For High Energy Physics, Fast Time Response, High Pulse Linearity 127 mm (5 Inch) Diameter, Bialkali Photocathode, 14-Stage, Head-on Type

GENERAL

Parameter		Description	Unit
Spectral Response		300 to 650	nm
Wavelength of Maximum Response		420	nm
Photocathode	Material	Bialkali	—
	Minimum Effective Area	φ120	mm
Window Material		Borosilicate glass	—
Dynode	Structure	Linear focused	—
	Number of Stages	14	—
Operating Ambient Temperature		-30 to +50	°C
Storage Temperature		-30 to +50	°C
Base		20-pin base	—
Suitable Socket		E678-20B (supplied)	—

MAXIMUM RATINGS (Absolute Maximum Values)

Parameter		Value	Unit
Supply Voltage	Between Anode and Cathode	3000	V
	Between Anode and Last Dynode	500	V
Average Anode Current		0.2	mA

CHARACTERISTICS (at 25 °C)

Parameter		Min.	Typ.	Max.	Unit
Cathode Sensitivity	Luminous (2856 K)	55	70	—	μA/lm
	Blue Sensitivity Index (CS 5-58)	7.0	9.0	—	—
	Quantum Efficiency at 390 nm	—	22	—	%
Anode Sensitivity	Luminous (2856 K)	300	1000	—	A/lm
	Blue Sensitivity Index (CS 5-58)	—	130	—	—
Gain		—	1.4×10^7	—	—
Anode Dark Current (after 30 min storage in darkness)		—	50	300	nA
Time Response	Anode Pulse Rise Time	—	2.5	—	ns
	Electron Transit Time	—	54	—	ns
	Transit Time Spread	—	1.2	—	ns
Pulse Height Resolution with ^{137}Cs		—	8.3	—	%
Gain Deviation	Long Term	—	1.0	—	%
	Short Term	—	1.0	—	%
Pulse Linearity *	2 % Deviation	—	160	—	mA
	5 % Deviation	—	250	—	mA

NOTE: Measured with special voltage distribution ratios shown in the Table 2.

Table 1: VOLTAGE DISTRIBUTION RATIO AND SUPPLY VOLTAGE

Electrode	K	G1	G2	Dy1	Dy2	Dy3	Dy4	Dy5	Dy6	Dy7	Dy8	Dy9	Dy10	Dy11	Dy12	Dy13	Dy14	P
Ratio	2.5	7.5	0	1.2	1.8	1	1	1	1	1	1	1	1	1.5	1.5	3	2.5	

Supply Voltage: 2000 Vdc, K: Cathode, Dy: Dynode, P: Anode, G: Grid

Table 2: SPECIAL VOLTAGE DISTRIBUTION RATIO AND SUPPLY VOLTAGE FOR PULSE LINEARITY MEASUREMENT

Electrode	K	G1	G2	Dy1	Dy2	Dy3	Dy4	Dy5	Dy6	Dy7	Dy8	Dy9	Dy10	Dy11	Dy12	Dy13	Dy14	P
Ratio	2.5	7.5	0	1.2	1.8	1	1	1	1	1.2	1.5	2	2.8	4	5.7	8	5	
Capacitors in μF											0.01	0.01	0.02	0.02	0.02	0.04	0.06	

Supply Voltage: 2500 Vdc, K: Cathode, Dy: Dynode, P: Anode, G: Grid

PHOTOMULTIPLIER TUBE R1250

Figure 1: Typical Spectral Response

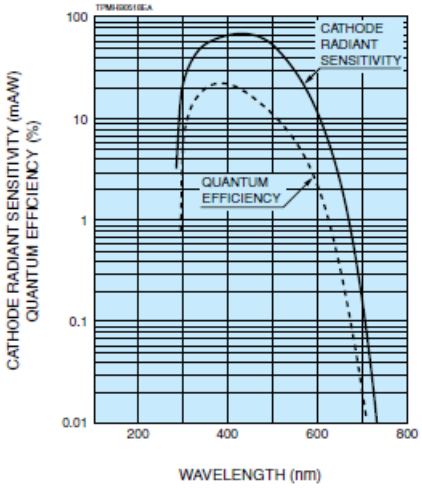

Figure 2: Typical Gain Characteristics

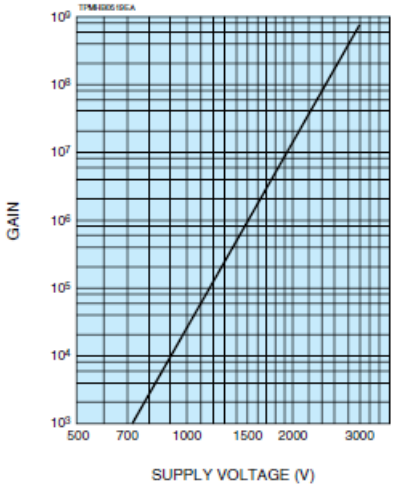

Figure 3: Dimensional Outline and Basing Diagram (Unit: mm)

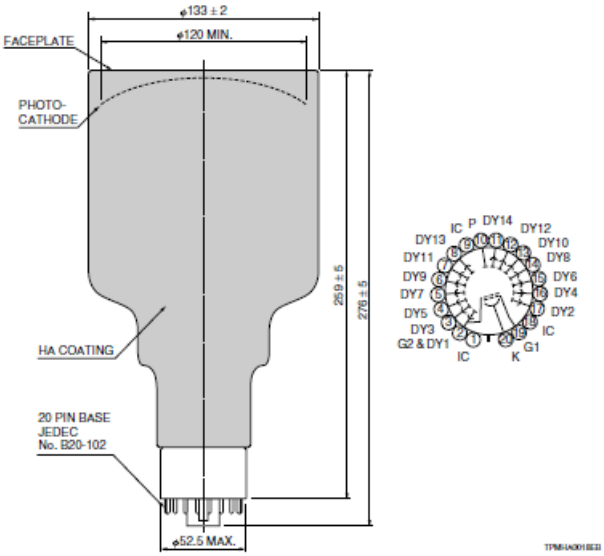

Socket E678-20B (Supplied)

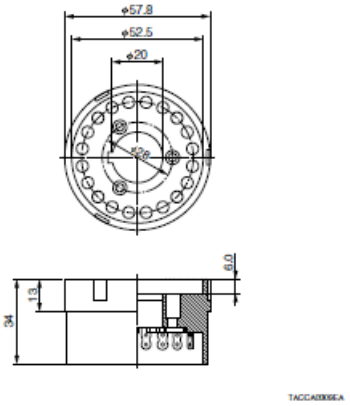

HAMAMATSU PHOTONICS K.K. www.hamamatsu.com

HAMAMATSU PHOTONICS K.K., Electron Tube Division
314-5, Shimokanzo, Iwata City, Shizuoka Pref., 438-0193, Japan, Telephone: (81)539/62-5248, Fax: (81)539/62-2205
U.S.A.: Hamamatsu Corporation: 360 Foothill Road, P. O. Box 6910, Bridgewater, N.J. 08807-0910, U.S.A., Telephone: (1)908-231-0960, Fax: (1)908-231-1218 E-mail: usa@hamamatsu.com
Germany: Hamamatsu Photonics Deutschland GmbH: Arzbergerstr. 10, D-82211 Herrsching am Ammersee, Germany, Telephone: (49)8152-375-0, Fax: (49)8152-2658 E-mail: info@hamamatsu.de
France: Hamamatsu Photonics France S.A.R.L.: 19, Rue du Saule Trapu, Parc du Moulin de Massy, 91882 Massy Cedex, France, Telephone: (33)1 69 53 71 00, Fax: (33)1 69 53 71 10 E-mail: infos@hamamatsu.fr
United Kingdom: Hamamatsu Photonics UK Limited: 2 Howard Court, 10 Tewin Road Welwyn Garden City Hertfordshire AL7 1BW, United Kingdom, Telephone: 44-(0)1707-294888, Fax: 44(0)1707-325777 E-mail: info@hamamatsu.co.uk
North Europe: Hamamatsu Photonics Nordan AB: Smidesvägen 12, SE-171-41 SOLNA, Sweden, Telephone: (46)8-509-031-00, Fax: (46)8-509-031-01 E-mail: info@hamamatsu.se
Italy: Hamamatsu Photonics Italia: S.R.L.: Strada della Moia, 1/E, 20020 Arese, (Milano), Italy, Telephone: (39)02-935 81 733, Fax: (39)02-935 81 741 E-mail: info@hamamatsu.it

TPMH1213E03
DEC. 2010 IP

51 mm (2") photomultiplier
9807B series data sheet

ET Enterprises electron tubes

1 description

The 9807B is a 51 mm (2") diameter, end window photomultiplier with blue-green sensitive bialkali photocathode and 12 high gain, high stability, BeCu dynodes of linear focused design for good linearity and timing. It is a plug-in replacement for the RCA 8575 and has a 21 pin base.

2 applications

- high energy physics studies

3 features

- good SER
- high pulsed linearity

4 window characteristics

	9807B borosilicate
spectral range** (nm)	290 - 630
refractive index (n_d)	1.49
K (ppm)	300
Th (ppb)	250
U (ppb)	100

*note that the sidewall of the envelope contains graded seals of high K content
** wavelength range over which quantum efficiency exceeds 1 % of peak

5 typical spectral response curves

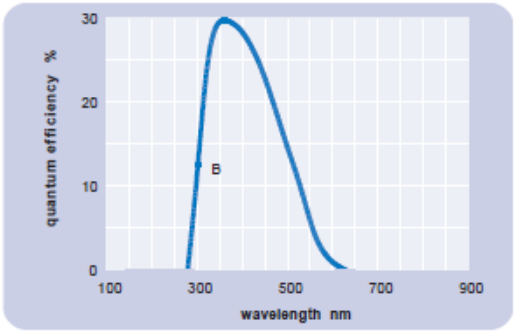

6 characteristics

	unit	min	typ	max
photocathode: bialkali				
active diameter	mm		46	
quantum efficiency at peak	%		30	
luminous sensitivity	µA/lm		70	
with CB filter		8	11.5	
with CR filter			2	
dynodes: 12LFBeCu				
anode sensitivity in divider A:				
nominal anode sensitivity	A/lm		500	
max. rated anode sensitivity	A/lm		2000	
overall V for nominal A/lm	V		1650	2300
overall V for max. rated A/lm	V		1900	
gain at nominal A/lm	x 10^6		7	
dark current at 20 °C:				
dc at nominal A/lm	nA		3	20
dc at max. rated A/lm	nA		20	
dark count rate	s^{-1}		300	
pulsed linearity (-5% deviation):				
divider A	mA		50	
divider B	mA		150	
pulse height resolution:				
single electron peak to valley	ratio		2	
rate effect (I_a for Δg/g=1%):	µA		1	
magnetic field sensitivity: the field for which the output decreases by 50 %				
most sensitive direction	T x 10^{-4}		1	
temperature coefficient:	% $°C^{-1}$		± 0.5	
timing:				
single electron rise time	ns		2	
single electron fwhm	ns		3	
single electron jitter (fwhm)	ns		2.2	
multi electron rise time	ns		3.2	
multi electron fwhm	ns		4.5	
transit time	ns		41	
weight:	g		150	
maximum ratings:				
anode current	µA			100
cathode current	nA			100
gain	x 10^6			30
sensitivity	A/lm			2000
temperature	°C	-30		60
V (k-a)[1]	V			2800
V (k-d1)	V			500
V (d-d)[2]	V			450
ambient pressure (absolute)	kPa			202

[1] subject to not exceeding max. rated sensitivity [2] subject to not exceeding max rated V(k-a)

7 typical voltage gain characteristics

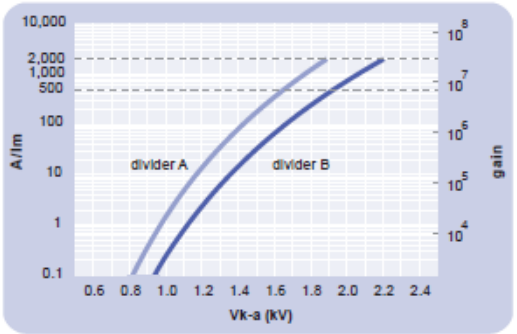

8 voltage divider distribution

	k	d_1	d_2	.....	d_9	d_{10}	d_{11}	d_{12}	a	
A	300V	R		.....	R	R	R	R	R	Standard
B	300V	R		.....	R	1.25R	1.5R	2R	3R	High Pulsed Linearity

note: focus connected to d_1.

Characteristics contained in this data sheet refer to divider A unless stated otherwise.

9 external dimensions mm

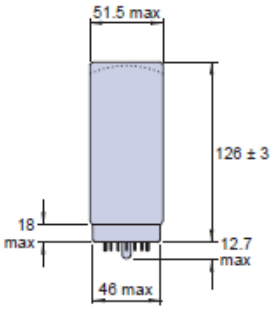

10 base configuration (viewed from below)

'ic' indicates an internal connection

note: connect f to d_1

Our range of B21 sockets, available for this series, includes versions with or without a mounting flange, and versions with contacts for mounting directly onto printed circuit boards.

11 ordering information

The 9807B meets the specification given in this data sheet. You may order **variants** by adding a suffix to the type number. You may also order **options** by adding a suffix to the type number. You may order product with **specification options** by discussing your requirements with us. If your selection option is for one-off order, then the product will be referred to as 9807A. For a repeat order, **ET Enterprises** will give the product a two digit suffix after the letter B, for example B21. This identifies your specific requirement.

9807 □ □

options

E	electrostatic shielding see drawing below
S	electromagnetic shielding see drawing below
M	supplied with spectral response calibration

specification options

B	as given in data sheet
A	single order to selected specification
Bnn	repeat order to selected specification

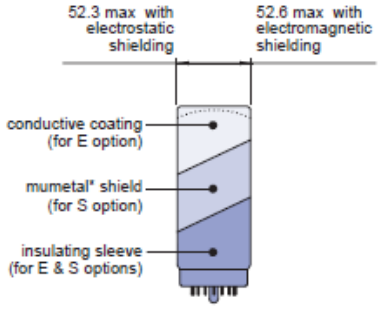

12 voltage dividers

The standard voltage dividers available for these pmts are tabulated below:

	k	d_1	d_2	d_3	.....	d_8	d_9	d_{10}	d_{11}	d_{12}	a
C628A	3R	R	R		.....	R	R	R	R	R	
C628B	3R	R	R		.....	R	1.25R	1.5R	2R	3R	
C628C	300 V	R	R		.....	R	R	R	R	R	
C628D	300 V	R	R		.....	R	1.25R	1.5R	2R	3R	

note: focus connected to d_1

R = 330 kΩ

*mumetal is a registered trademark of Magnetic Shield Corporation

ET Enterprises Limited
45 Riverside Way
Uxbridge UB8 2YF
United Kingdom
tel: +44 (0) 1895 200880
fax: +44 (0) 1895 270873
e-mail: sales@et-enterprises.com
web site: www.et-enterprises.com

ADIT Electron Tubes
300 Crane Street
Sweetwater TX 79556 USA
tel: (325) 235 1418
toll free: (800) 399 4557
fax: (325) 235 2872
e-mail: sales@electrontubes.com
web site: www.electrontubes.com

choose accessories for this pmt on our website

an ISO 9001 registered company

DS_ 9807B Issue 6 (23/01/12)

78 mm (3") photomultiplier
9821B series data sheet

ET Enterprises electron tubes

1 description

The 9821B is a 78mm (3") diameter, end window photomultiplier with blue-green sensitive bialkali photocathode on a plano-concave window, and 12 BeCu dynodes of linear focused design for good linearity and timing.

2 applications

- high energy physics studies
- scintillation spectroscopy

3 features

- good SER
- high pulsed linearity
- fast time response

4 window characteristics

	9821B borosilicate
spectral range *(nm)	285 - 630
refractive index (n_d)	1.47
K (ppm)	300
Th (ppb)	550
U (ppb)	450

* wavelength range over which quantum efficiency exceeds 1 % of peak

5 typical spectral response curves

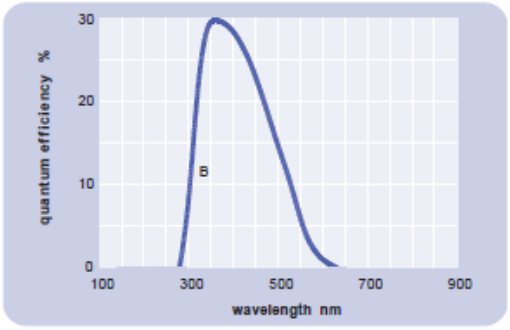

6 characteristics

	unit	min	typ	max
photocathode: bialkali				
active diameter	mm		67	
quantum efficiency at peak	%		30	
luminous sensitivity	µA/lm		75	
with CB filter		8	12	
with CR filter			2	
dynodes: 12LFBeCu				
anode sensitivity in divider B:				
nominal anode sensitivity	A/lm		500	
max. rated anode sensitivity	A/lm		2000	
overall V for nominal A/lm	V		2000	2600
overall V for max. rated A/lm	V		2250	
gain at nominal A/lm	x 10^6		7	
dark current at 20 °C:				
dc at nominal A/lm	nA		10	50
dc at max. rated A/lm	nA		40	
dark count	s^{-1}		500	
pulsed linearity (-5% deviation):				
divider A	mA		50	
divider B	mA		150	
pulse height resolution:				
single electron peak to valley	ratio		2	
rate effect (I_a for $\Delta g/g$=1%):	µA		1	
magnetic field sensitivity: the field for which the output decreases by 50 %				
most sensitive direction	T x 10^{-4}			
temperature coefficient:	% $°C^{-1}$		± 0.5	
timing:				
single electron rise time	ns		2.1	
single electron fwhm	ns		3.2	
single electron jitter (fwhm)	ns		2.2	
transit time	ns		42	
weight:	g		260	
maximum ratings:				
anode current	µA			100
cathode current	nA			200
gain	x 10^6			27
sensitivity	A/lm			2000
temperature	°C	-30		60
V (k-a)[1]	V			2900
V (k-d1)	V			600
V (d-d)[2]	V			450
ambient pressure (absolute)	kPa			202

[1] subject to not exceeding max. rated sensitivity [2] subject to not exceeding max rated V(k-a)

7 typical voltage gain characteristics

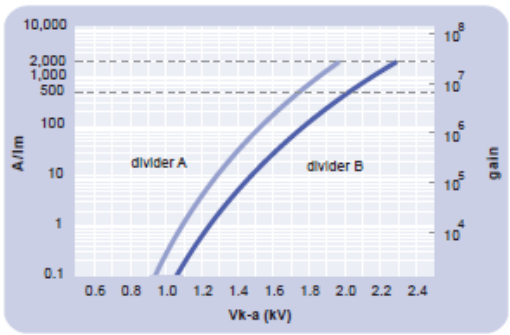

8 voltage divider distribution

	k	d_1	d_2	d_9	d_{10}	d_{11}	d_{12}	a	
A	450V	R		R	R	R	R	R	Standard
B	450V	R		R	1.25R	1.5R	2R	3R	High Pulsed linearity

note: focus connected to d_1

Characteristics contained in this data sheet refer to divider B unless stated otherwise.

9 external dimensions mm

The drawings below show the 9821B in hardpin format and the 9821KB with the B20 cap fitted.

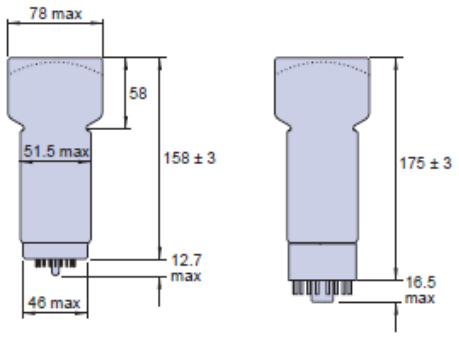

10 base configuration (viewed from below)

B19A hardpin base
(for 9821B)
'ic' indicates an internal connection

note: connect f to d_1

B20 cap
(for 9821KB)
'ic' indicates an internal connection

note: connect f to d_1

Our range of B19A sockets is available to suit the hardpin base. Our range of B20 sockets is available to suit the B20 cap. Both socket ranges include versions with or without a mounting flange, and versions with contacts for mounting directly onto printed circuit boards.

11 ordering information

The 9821B meets the specification given in this data sheet. You may order **variants** by adding a suffix to the type number. You may also order **options** by adding a suffix to the type number. You may order product with **specification options** by discussing your requirements with us. If your selection option is for one-off order, then the product will be referred to as 9816A. For a repeat order, ET Enterprises will give the product a two digit suffix after the letter B, for example B21. This identifies your specific requirement.

9821

base options
K capped

options
E electrostatic shielding see drawing below
M supplied with spectral response calibration

specification options
B as given in data sheet
A single order to selected specification
Bnn repeat order to selected specification

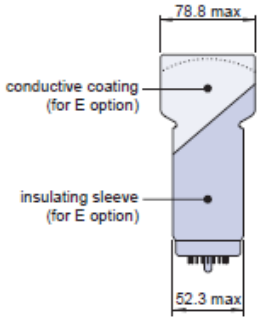

12 voltage dividers

The standard voltage dividers available for these pmts are tabulated below:

9821B	9821KB	k	d_1	d_2	d_9	d_9	d_{10}	d_{11}	d_{12}	a
C638P	C640P	3R	R	.....	R	R	R	R	R	
C638R	C640R	3R	R	.....	R	1.25R	1.5R	2R	3R	
C638S	C640S	450 V	R	.....	R	R	R	R	R	
C638T	C640T	450 V	R	.....	R	1.25R	1.5R	2R	3R	

R = 330 kΩ note: focus connected to d_1

*mumetal is a registered trademark of Magnetic Shield Corporation

ET Enterprises Limited
45 Riverside Way
Uxbridge UB8 2YF
United Kingdom
tel: +44 (0) 1895 200880
fax: +44 (0) 1895 270873
e-mail: sales@et-enterprises.com
web site: www.et-enterprises.com

ADIT Electron Tubes
300 Crane Street
Sweetwater TX 79556 USA
tel: (325) 235 1418
toll free: (800) 399 4557
fax: (325) 235 2672
e-mail: sales@electrontubes.com
web site: www.electrontubes.com

choose accessories for this pmt on our website

an ISO 9001 registered company

DS_ 9821B Issue 9 (23/01/12)

Appendix D– Photomultiplier Bases

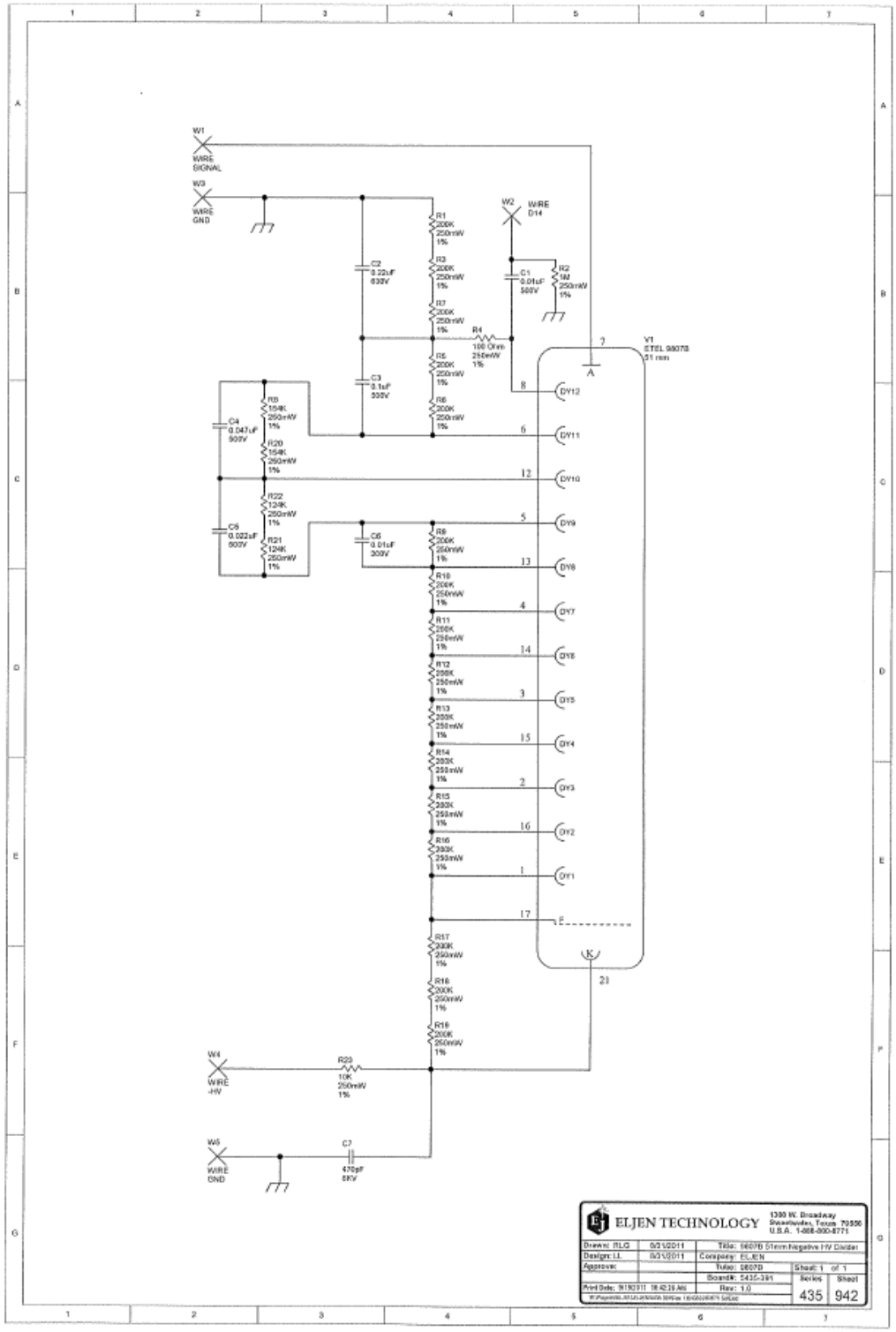
W1
WIRE
SIGNAL
W3
WIRE
GND
W2
WIRE
D14
R1
200K
250mW
1%
R3
200K
250mW
1%
R7
200K
250mW
1%
R4
100 Ohm
250mW
1%
R5
200K
250mW
1%
R6
200K
250mW
1%
C2
0.22uF
630V
C1
0.01uF
500V
R2
1M
250mW
1%
C3
0.1uF
300V
V1
ETEL 9807B
51 mm
7
A
8
DY12
6
DY11
12
DY10
5
DY9
13
DY8
4
DY7
14
DY6
3
DY5
15
DY4
2
DY3
16
DY2
1
DY1
17
K
21
R9
154K
250mW
1%
C4
0.047uF
500V
R20
154K
250mW
1%
R22
124K
250mW
1%
C5
0.022uF
500V
R21
124K
250mW
1%
C6
0.01uF
300V
R8
200K
250mW
1%
R10
200K
250mW
1%
R11
200K
250mW
1%
R12
200K
250mW
1%
R13
200K
250mW
1%
R14
200K
250mW
1%
R15
200K
250mW
1%
R16
200K
250mW
1%
R17
200K
250mW
1%
R18
200K
250mW
1%
R19
200K
250mW
1%
W4
WIRE
-HV
R23
10K
250mW
1%
W5
WIRE
GND
C7
470pF
6KV
ELJEN TECHNOLOGY
1300 W. Broadway
Sweetwater, Texas 79556
U.S.A. 1-888-800-8771
Drawn: RLG
9/31/2011
Design: LL
9/31/2011
Approved:
Title: 9807B 51mm Negative HV Divider
Company: ELJEN
Tube: 9807B
Board#: 5435-391
Rev: 1.0
Sheet: 1 of 1
Series
435
Sheet
942

Appendix E – Sample event scanner code

The current architecture of the software is that of a multi-threaded single-process application with dynamic memory allocation of data-collection buffers. The compiler's thread pool package is used to schedule and execute all working threads. Thread-safe dynamically-allocated queues are used to pass data among threads. A writer thread polls for data and stores them in a queue, while a reader thread performs data parsing, DPSD and data display. Data rates with full point-by-point digitization (typically 1 ns/point) over a 400 ns window with event-mode recording of the entire pulse for each event is on the order of several thousand events/s. This allows post-experiment replay of the data stream with optimization of the DPSD and other derived signals if needed.

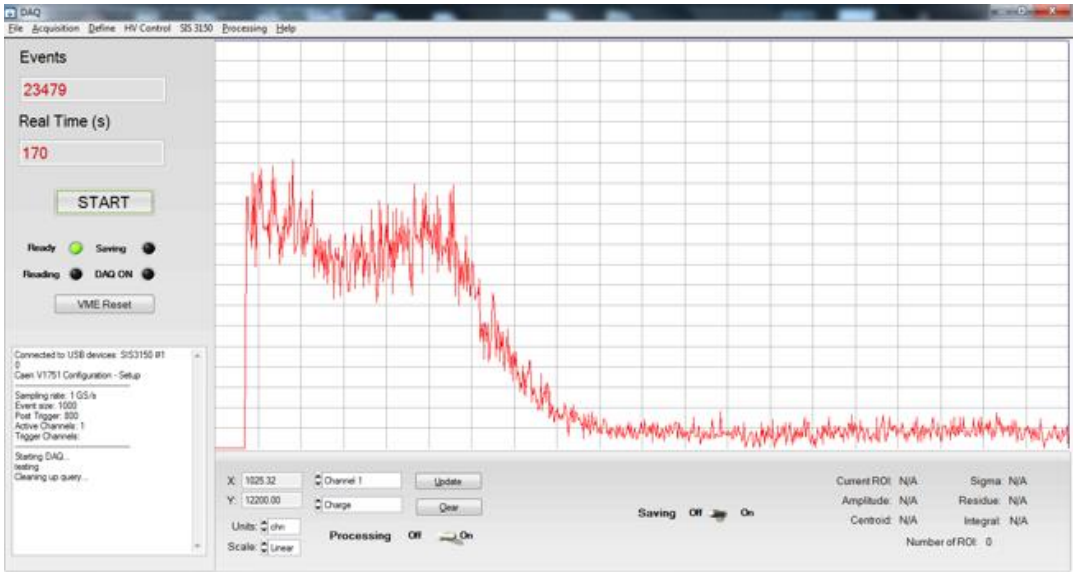

Figure E.1 - A snapshot of the author's user-friendly GUI for the UM-DSA DAQ software.

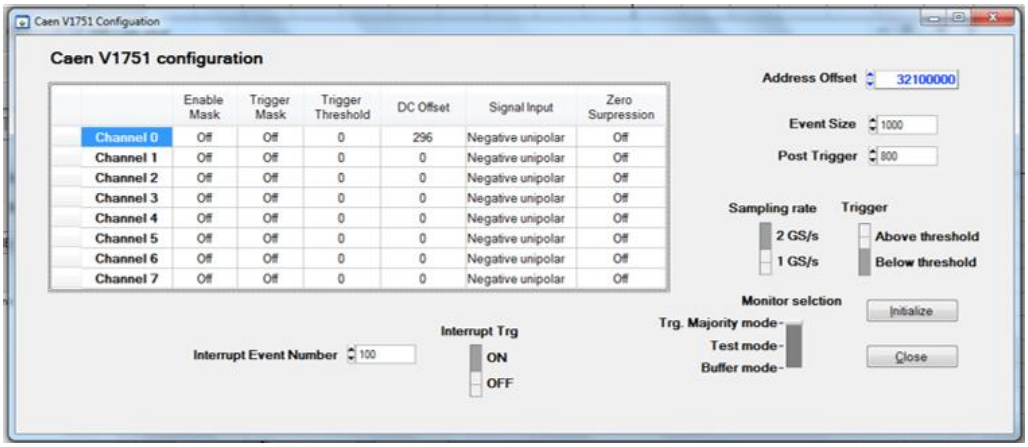

Figure E.2 - A snapshot of GUI for configuration of the CAEN V1751 waveform digitizer.

```
/*****************************************************************************
 *
 *  Filename: Scanner.cpp
 *
 *  Description:
 *
 *          Author(s):
 *     Michael T. Febbraro
 *
 *  Creation Date: 11/25/2012
 *  Last modified: 5/9/2013
 *
 * ----------------------------------------------------
 * Nuclear Reaction Group
 *  University of Michigan, Ann Arbor, MI, USA
 *  (c) All Rights Reserved.
 *
 */

#include <iostream>
#include <fstream>
#include <iomanip>
#include <cstdlib>
#include <cmath>
#include <ctime>
#include <signal.h>
#include "CaenEvent.h"
#include "PulseAnalysis.h"
#include "Physics.h"

using namespace std;

/** ----------------------------------------------------
```

```
*           Variable declaration
*   ----------------------------------------------------
*/
char      filename[250], prompt[10], interrputPrompt;

ofstream fid;

long      TEvt = 0;

float     pulse [2000],
          baseline[2000],
          paraL, paraS,
          CFD, amplitude,
          risetime, falltime,
          width, result,
          T1, T2, KE;

int       return_code,
          length = 0,
          events,
          query_limit,
          numPeaks,
          locPeaks,
          i, j, k,
          event_stats[3] = {0, 0, 0};

bool flag, eof = 1;

clock_t Stop, Start;


void interrupt (int param)
{
          cout << endl << "Interrupt..." << endl;
          cout << "Continue (C), Abort (A), Status (S) : ";
          cin >> interrputPrompt;

          if (interrputPrompt == 'A')
          {
                    cout << "Aborting..." << endl;
                    exit(EXIT_SUCCESS);
          }
          if (interrputPrompt == 'S')
          {
                    Stop = clock();
                    cout << "--------------------------------------------------" << endl;
                    cout << "Elapsed time(s): " << (float)(Stop - Start)/CLOCKS_PER_SEC << endl;
                    cout << "\nEvent stats:\n";
                    cout << " - Total Events: " << (event_stats[0] + event_stats[1]) << endl;
                    cout << " - Bad Events: " << event_stats[1] << endl;
                    cout << "--------------------------------------------------" << endl;
          }

}

int main()
```

```
{
        signal (SIGINT,interrupt);

        /** ------------------------------------------------
        *       Get functions
        *   ------------------------------------------------
        */

        CaenEvent *Events = new CaenEvent();
        PulseAnalysis *Analysis = new PulseAnalysis();
        Physics *Phys = new Physics();

        /** ------------------------------------------------
        *       Program start...
        *   ------------------------------------------------
        */

        cout << "Binary file to read: ";
        cin >> filename;

        Events->LoadFile(filename);

        cout << "Number of events to process (# or -1 for all): ";
        cin >> query_limit;

        cout << "Processed name to be created: ";
        cin >> filename;

        fid.open(filename);

        Start = clock();

        while(eof)
        {

        /** ------------------------------------------------
        *       Read next event...
        *   ------------------------------------------------
        */

        return_code = Events->NextEvent();

        /** ------------------------------------------------
        *       Get scintillation pulse
        *   ------------------------------------------------
        */

        if (return_code == 0) { return_code = Events->GetNextChannel(pulse, &length);}

        /** ------------------------------------------------
        *       Process in order..
        *       1 - Time pickoff
        *       2 - Find number of peaks
        *       3 - Restore baseline
        *       4 - Pulse parameters
        *       5 - PSD integration
```

```
*   ------------------------------------------------
*/

if (return_code == 0) { return_code = Analysis->PeakFinder(pulse, length, 8, 50, 2, &numPeaks,
&locPeaks); }

if (return_code == 0) { return_code = Analysis->Baseline_restore(pulse, baseline, length, 50, 3); }

if (return_code == 0) { return_code = Analysis->Time_Pickoff(pulse, length, 3, 0, 950, 1, &T1); }

if (return_code == 0) { return_code = Analysis->Parameters(pulse, length, 3, &CFD, &amplitude,
&risetime, &falltime, &width);  }

if (return_code == 0) { return_code = Analysis->PSD_Integration(pulse, length, 50, 600, 43, 3,
&paraL, &paraS);  }


/** ------------------------------------------------
*           Print results for this event...
*   ------------------------------------------------
*/

if (return_code == 0) {fid << amplitude << " " << numPeaks << " " << CFD << " " << paraL << " "
<< paraS << endl;}

/** ------------------------------------------------
*           Get status updates during processing
*   ------------------------------------------------
*/

if (return_code == 0) { return_code = Events->GetEventNumber(&events); }

if (return_code == -2) { break;}
if (return_code == -3) { cout << "\n\nStart of new event not found, possible end of file\nStopping
processing...\n" << endl; break;}

if (return_code != 0) { event_stats[1]++;}
else {event_stats[0]++;}

if (TEvt%100==0)
{
        cout << "Events: " << TEvt << "   Record: " << events;
        cout << "   Bad Events: " << event_stats[1] << "\r" << flush;
}
else    if (TEvt >= query_limit && query_limit != -1)
{ cout << "\n-- Query limit --\n\nProcessed events: " << TEvt << endl; eof = 0;}
TEvt++;

}

Stop = clock();
cout << "Elapsed time(s): " << (float)(Stop - Start)/CLOCKS_PER_SEC << endl;
cout << "\nEvent stats:\n";
cout << " - Total Events: " << (event_stats[0] + event_stats[1]) << endl;
cout << " - Bad Events: " << event_stats[1] << endl;
```

```
        fid.close();

        Events->CloseFile();

        cout << "Finished... Enter any key to exit: " << endl;
        cin >> prompt;

return 0;
}
```

Appendix F – Preparation of Deuterated Polyethylene Targets

Deuterated targets are an essential part of (d,d), (d,n), (d,p), (d,^{3}He) and many other reactions involving deuterons thus it is important to be able produce such targets with high reliability and repeatability. The standard choice for deuterium targets is the use of deuterated polyethylene $[C_2D_4]_n$ which is typically prepared is via evaporation from a heated solution of deuterated polyethylene in xylene [Bar77]. This method works quite well and I will introduce the technique with a few improvements were found which aids in the process.

Figure F.1 – Preparation of a glass slide coated with releasing agent

Target can be prepared on clean glass slides (microscope slides work quite nicely). For very thin targets, a releasing agent can be precoated on the slides prior to use which aids in the removal of the finished target. It should be noted that it is best to avoid releasing agents if possible as they can contaminate the finish target. Typical releasing agents are common alkali salts which have a high solubility as well as powdered detergents such as Boraxo® powdered hand soap (90% $NaB_4O_7 \cdot 10H_2O$, 10% Lye soap). To apply a releasing agent, one can prepare a concentrated solution of the agent and place the in a large glass with the glass slide on the bottom such that liquid completely covers the slide. A petri dish works well for this application. The solution is then let to evaporate via slow evaporation or with the aid of a heat lamp as shown in Figure F.1.

Figure F.2 – A finished large-area deuterated polyethylene target

To prepare the target itself, 100 mg of $[C_2D_4]_n$ is added to a beaker of 20 mL of xylene. Note that xylene is available in the ortho (o-xylene), meta (m-xylene), para (p-xylene)), or mixed configurations. For our studies, mixed xylene worked fine and has a lower cost than the others. The mixture is than heated on a hot plate ~140-150^oC till the $[C_2D_4]_n$ completely dissolves. Next

the solution is then transferred to an evaporation disk (small watch glass also works) which is placed on top of a beaker of boiling xylene. It was found that heating the disk by the boiling xylene provides a simple way of providing fairly uniform heating at the desire temperature (~Bp of xylene) without the use of a heating bath. This solution is then heated and allowed to evaporate till the viscosity is high enough to produce a uniform layer which does not run off when poured onto the glass slide. Without the use of instrumentations, the point at which the solution is 'ideal' I must say is known by experience and trial and error. Once poured onto a slide, the solution is then allowed to evaporate. To obtain thicker targets, layers can be added to the evaporated slide till the desire is achieved.

Once the target is prepared and evaporated onto the glass slide the next step is removal. It was found that freezing the freshly prepared target after evaporation aids in the removal process as the area of the target shrinks in the freezer thus loosening it from the glass. After freezing and warming back up to room temperatures, small wrinkles should be visible, a sign of contraction and loosening from freezing process. The glass slides are then placed directly on the heated hot plate. They are kept there till they are just about to blister then cooled off by immersion in deionized water. This process promotes polymerization and strengthens the targets and has been noted by others [Bar77]. After a few cycles of heat / cool, the target can be removed from the slides carefully using large area tweezers or other tools. It should be noted that slides coated with releasing agents may come off the slide when immersed in deionized water, thus a single heat /cool cycle may only be possible. A finished large area target is shown in Figure F.2.

Appendix G – Preparation of Tantalum Oxide Targets

The anodization of the Ta foils was conducted using a high density polyethylene (HDPE) cell constructed to produce single-sided targets with an active area of 25 mm or 50 mm in diameter. To restrain the electrolyte to a desired region of the foil, a specially designed flange on the HDPE sleeve was machined to allow a standard aluminum KF50 blank vacuum stub to be tightly attached using a KF50 clamp. This design was chosen because the Ta foil could be placed on the blank stub and pressed tightly against the HDPE sleeve with the use of the KF clamp. This allowed the creation of a water-tight seal while preventing tearing of the foil during the compression process. A 304 stainless steel cathode, positioned above the cell, was mounted in a Heidolph Type RZR50 variable speed overhead stirrer and rotated at 500 rpm throughout the anodization process. Current was supplied to the anode through an electrical connection screw located on the side of the KF50 blank stub and to the cathode with the use of a copper strap, which provided constant electrical conductivity during rotation. An Electronics Measurements Model C612 Constant Current power supply was used to obtain the required current density and the current was measured using a Fluke 179 Multi-meter in series. Ramping and rapid voltage fluctuations were monitored during the with the use of a Fluke 80K-6 1000x reduction HV probe and a Tektronix TDS 2022 digital oscilloscope connected in parallel with the cell.

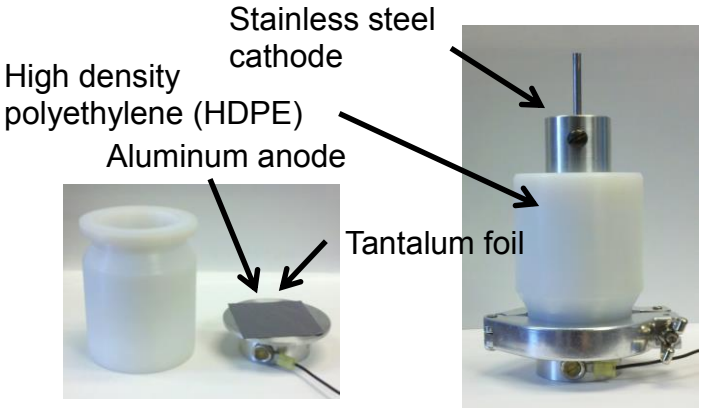

Figure G.1 - Anodization cell

Figure G.1 – Anodizing cell used to produce tantalum oxide targets

Ta targets were cut from 0.0003" high-purity Ta foils purchased from A.D Mackay INC. Each target was degreased using acetone (99.6% ACS reagent grade, Mallinckrodt AR) and chemically etched to a desired thickness of 5μm using a solution of 25% H_2SO_4 (96.9% ACS reagent grade, Baker Chemical Company), 10% HNO_3 (64-66% ACS reagent grade, Sigma Aldrich), and 7% HF (48% ACS reagent grade, Sigma Aldrich) in 8μS/cm deionized water. To determine the time required to achieve a desired foil thickness, Ta foils of known area were weighed, immersed in the etching solution for 2-minute intervals, washed with deionzied water, dried and reweighed. The area of the foil did not change appreciably during the etching process so changes in mass were primarily associated with changes in thickness. Thus, the percent mass loss could be directly related to a percent decrease in thickness within the error of our measurements. Figure G.2 shows the relationship between areal mass and time in the chemical etching solution.

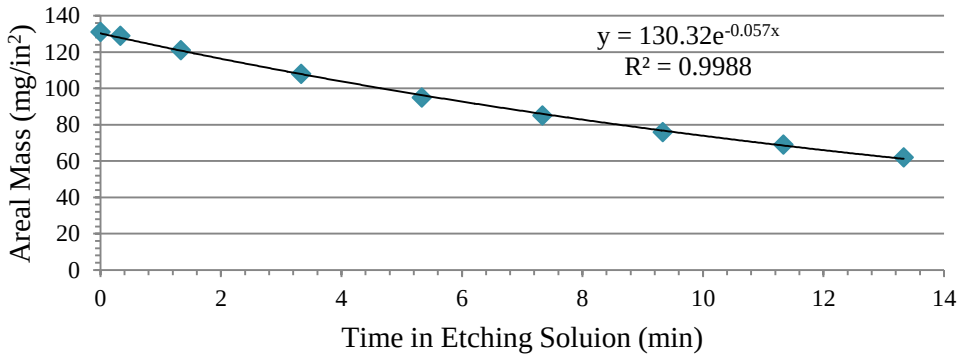

Figure G.2 - Etch rate of Tantalum foil in a 25% H_2SO_4 : 10% HNO_3 : 7% HF chemical etching solution at room temperature

Surface roughness and deflects of the chemically etched foils were determined via Atomic Force Microscopy (AFM) and Scanning Electron Microscopy (SEM) using an AFM and SEM. The AFM analysis shows surface roughness of the foil remained constant and might have been reduced from the etching process. This conclusion agrees with the non-linear nature of the etch rate curve because the reduction of surface area should reduce the reaction rate.

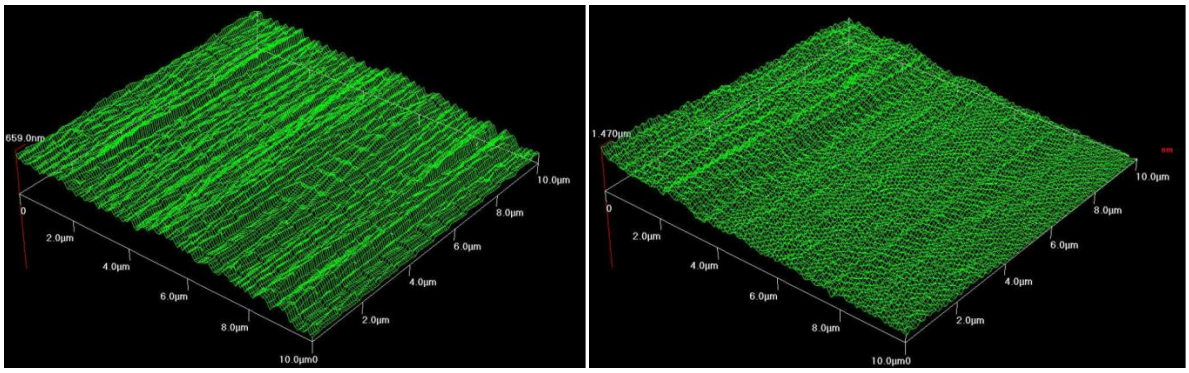

Figure G.3 - AFM images of before (left) and after (right) at 50% reduction in foil thickness from a 25% H_2SO_4 : 10% HNO_3 : 7% HF chemical etching solution at room temperature

X-ray fluorescence (XRF) analysis was conducted with an EDAX Li drifted Si detector during the SEM analysis at an accelerating voltage of 15.0 kV. The spectrums confirmed that oxidation of surface Ta to Ta_2O_5 by the oxidizing acids was minimal, presumably from the presence of the HF_2^- ion.

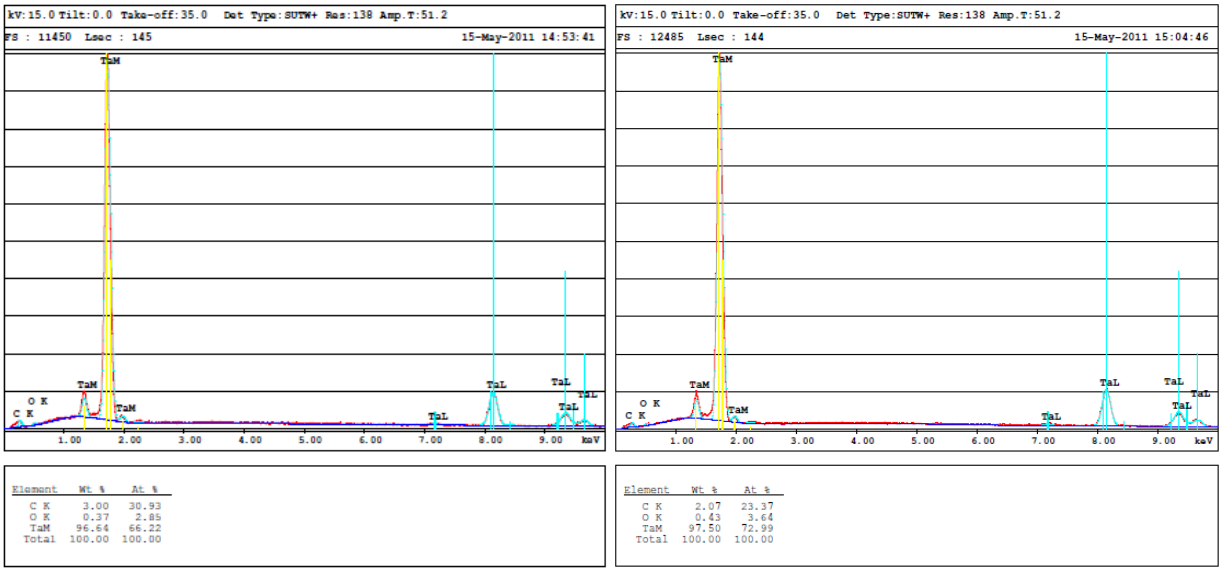

Figure G.4 - X-ray fluorescence spectroscope of the Ta foils of before (left) and after (right) at 50% reduction in foil thickness from a 25% H_2SO_4 : 10% HNO_3 : 7% HF chemical etching solution at room temperature

Anodization was conducted by placing the targets on the aluminum KF blank stub and fastening it to the cell using a KF vacuum clamp. The electrolyte consisted of 0.1% KI (99% ACS reagent grade, Sigma Aldrich) in 8µS/cm deionized water. Analysis of the electrolyte solution

yielded a conductivity of -1.18mS/cm and a pH of 6.39 prior to use. A volume of 50 ml of the electrolyte was poured into the cell and degassed for 1 hour by bubbling nitrogen gas through the solution. The cathode was cleaned with 91% USP isopropyl alcohol and placed 1 ¾" above the anode.

An attempt was made to determine the areal density of oxygen in the form Ta_2O_5 on the Ta foil using Rutherford Backscatter Analysis (RBS). The analysis was conducted at The Michigan Ion Beam Laboratory (MIBL) using their 1.7-MV Tandem accelerator. A foil with an active area of 25 mm in diameter was position orthogonally to the beam-line with a thick Si detector located at 160^{o}. A deuterium beam at 0.970 MeV was generated using a terminal voltage of 470 kV and an additional 30 kV from the duoplasmatron ion source. A standard sample of Au on Si and plain Si was run prior to the foil for channel-energy calibration.

Appendix H – Preparation of ^{13}C Targets

Carbon targets are widely used in nuclear physics as ether the primary target, as backing support for a sputtered target, or as stripper foils in tandem accelerators, in addition to other uses. Typical preparation technique is by cracking of methane or enriched Iodo-methane (CH_3I) on a heated surface [Ram83] or by evaporation using an electron gun [Cha83]. In order to study the $^{13}C(\alpha,n)^{16}O$ reaction a ^{13}C target was desired which must withstand high primary beam currents (50-100 µA) at low beam energies (0.2 – 1.0 MeV). Reactions of nuclear astrophysics importance such as the $^{13}C(\alpha,n)^{16}O$, typically are at low incident projectile energy and thus require ultra-thin targets to obtain reasonable energy resolution. This in combination with the high primary beam current as mentioned required that a liquid-cooled target be prepared on a high-Z backing material to limit unwanted secondary nuclear reactions. Due to these limitations the method of [Ram83] was well suited for this work.

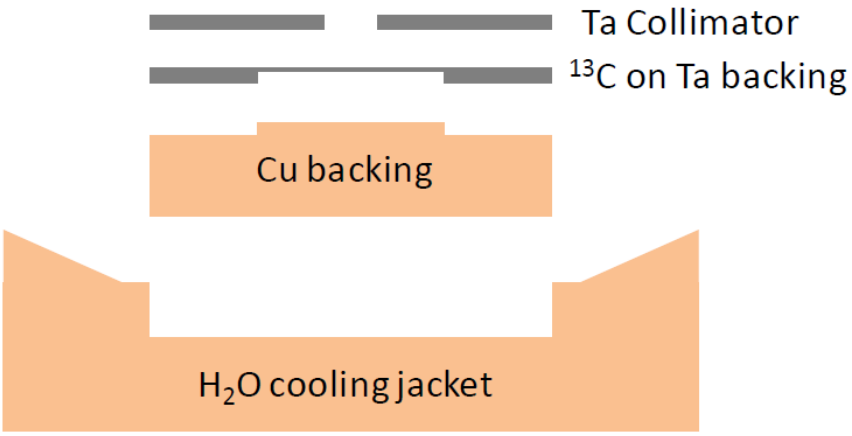

Figure H.1 – Illustration of enriched ^{13}C target assembly

Experimental constraints required that the target withstand beam currents of 50-100 µA at incident energies of 0.2 – 1.0 MeV resulting in an overall beam power of 10 – 100 watts. This is

on the order of a standard incandescent bulb. The experimental goal is to determine the neutron cross section thus the target, housing, and water-cooling system should be as this as possible and make with material which will not significantly alter the outgoing neutron spectra. The material of choice was oxygen-free high thermal conductivity (OFHC) copper which is an excellent material for thermal transport and strong enough to withstand the pressures associated with operation as a vacuum chamber. 1g of $^{13}CH_3I$ liquid with copper stabilizer enriched to 99% was purchased through Sigma Alrich in a glass vial with etched seal . The target holder and chamber was designed in 5 main pieces; the vacuum chamber, water cooled jacket, Cu backing, Tantalum boat with enriched ^{13}C target layer cracked on the front, and tantalum collimator as illustrated in Figure H.1. The following cleaning procedure was used for the tantalum components:

Procedure used for cleaning of tantalum components

1. Degrease in boiling methanol for >15 mins
2. Acid etch in aqueous 25% H_2SO_4, 10% HNO_3, 7% HF (v/v) for 5 Mins
3. Rinse with triple distilled H_2O
4. Dry with dry nitrogen

It should be noted that the importance of the etching step is under debate [Gör13] but was used in this work. The copper components were cleaned with a slightly different procedure primarily due the highly corrosive nature of the etching solution required for tantalum.

Procedure used for cleaning of copper components

1. Degrease in boiling methanol for >15 mins
2. Acid etch in aqueous solution of 10% HCl
3. Rinse with triple distilled H_2O
4. Dry with dry nitrogen

The target was prepared on a tantalum boat 200 μm thick which was resistively heated in vacuum to a glowing white temperature by a 100 amp d.c. power supply. A side chamber contained a glass vial of $^{13}CH_3I$ liquid which was opened by shaking the chamber with a copper

slug inside to break the etched glass seal all while under vacuum as shown in Figure H.3. Once at temperature, a valve separating the $^{13}CH_3I$ liquid and heated tantalum boat was open to allow the high vapor pressure $^{13}CH_3I$ gas to fill the chamber a pressure of approx. 75 torr. The thickness of the ^{13}C target is controlled by exposure time of the $^{13}CH_3I$ vapor with the heated Tantalum boat.

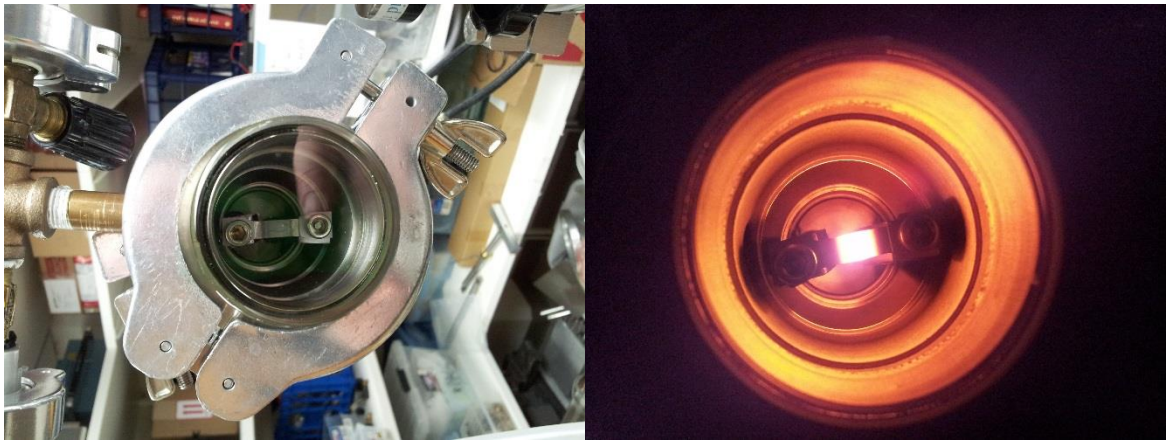

Figure H.2 – The tantalum boat fastened inside the vacuum chamber before (left) and during resistive heating (right)

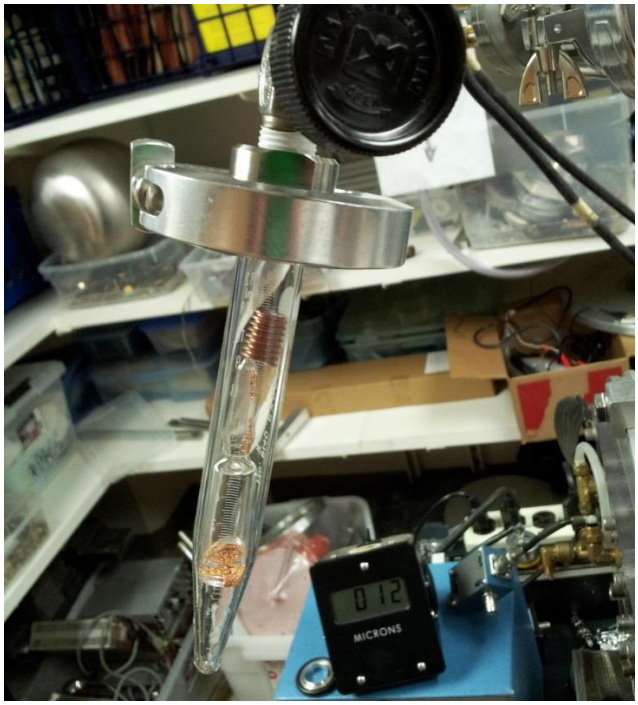

Figure H.3 – Side vacuum chamber contain a glass vial of $^{13}CH_3I$ with an etched seal and copper slug for breaking the seal once under vacuum

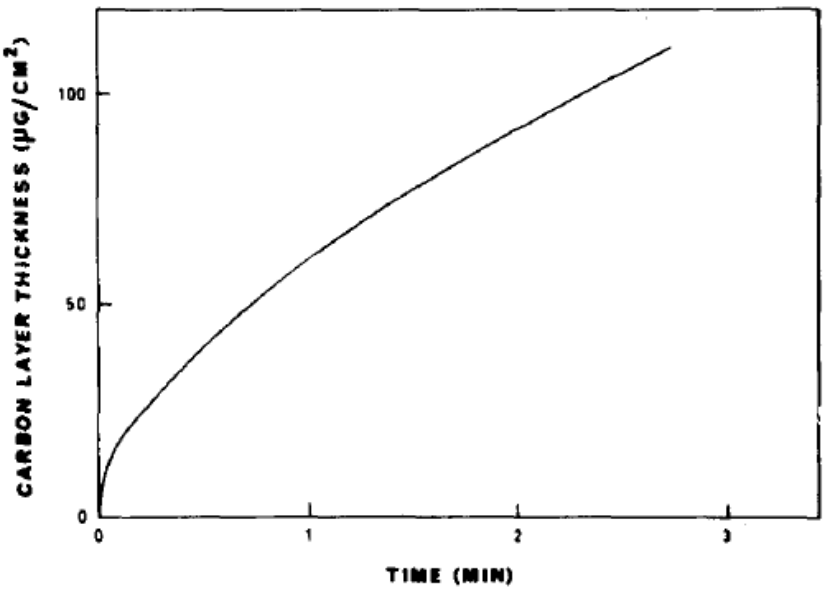

Figure H.4 – Plot of target thickness versus exposure time at a pressure of 0.01 MPa $^{13}CH_3I$ vapor (from [Ram83)

45 sec exposure time was used for the targets prepared in this study. A plot of exposure time versus ^{13}C thickness by [Ram83] is shown in Figure H.4. The assembled target is shown in Figure H.5

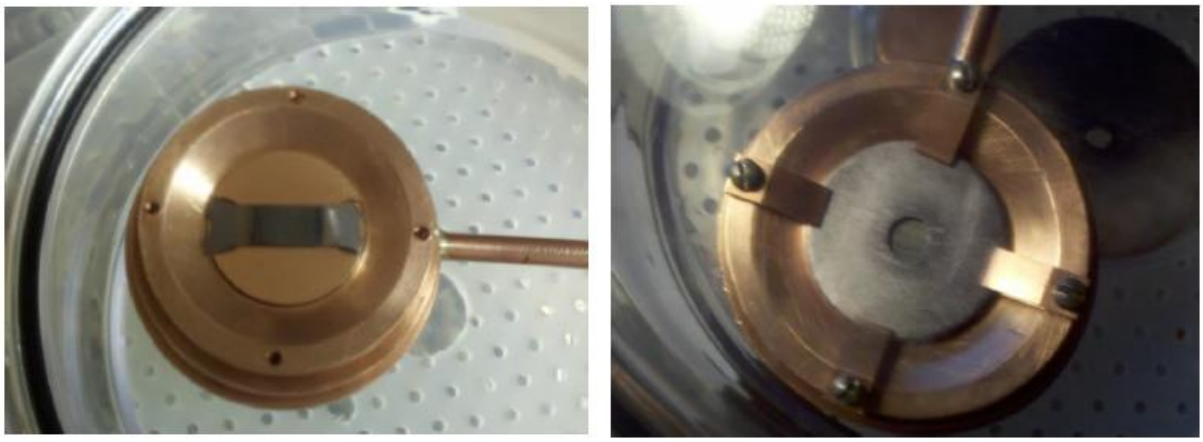

Figure H.5 – The ^{13}C water-cooled target showing the dark ^{13}C layer (left) and assembled with tantalum collimator and copper finger clamps (right)

Appendix I – Fresco Graphical Interface

A graphical interface for the nuclear reactions code Fresco [Tho88] was written in C++ by the author. The program is meant to serve a user-friendly graphical interface which can be used to generate input files or run Fresco directly. The program contain many useful features such as mass libraries and global OMPs all displayed on a friendly interface.

The reaction to be calculated is input in the 'Partition' tab shown in Figure I.1. The user selects the reaction and product isotopes, spin and parity, and excitation energy. The program then calculates the reaction Q-value from mass tables. The user then selects to use either the entrance, exit, or both entrance and exit partitions in the calculation.

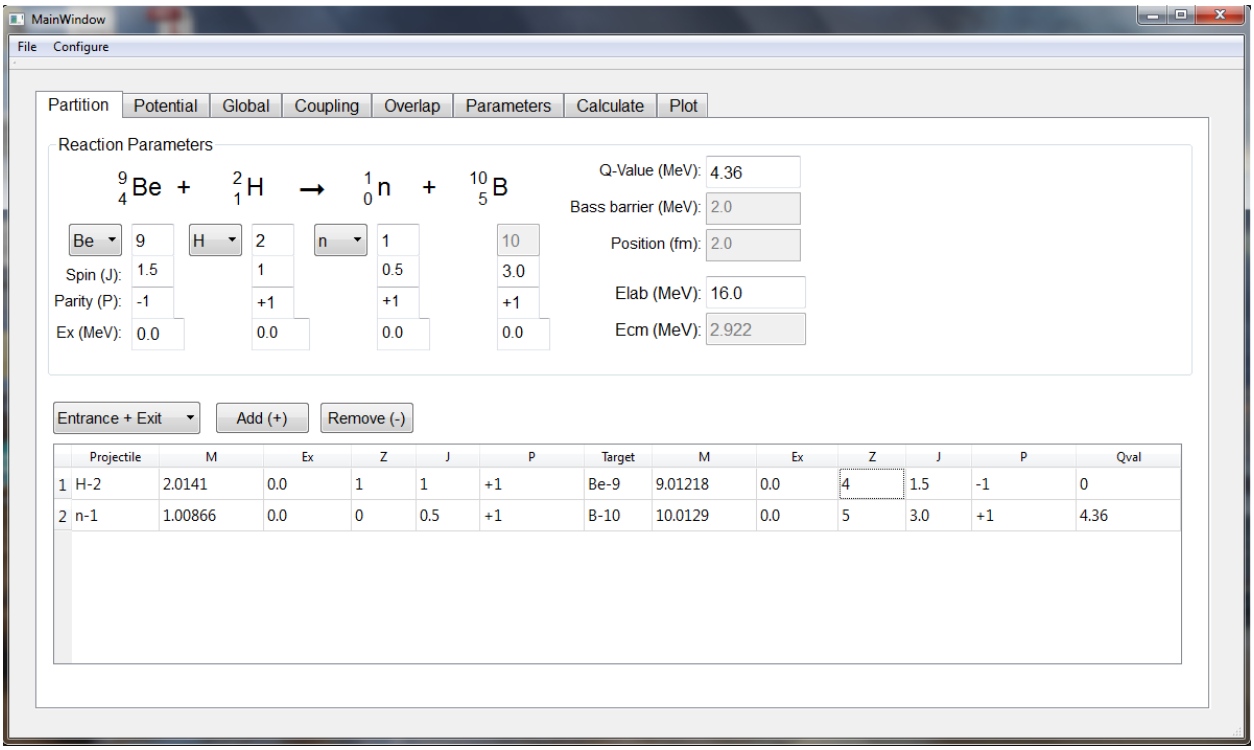

Figure I.1 – Partition tab used to input the reaction to be calculated.

Next the user selects the potentials to be used in the reaction in the 'Potential' tab, shown in Figure I.2. Once a potential has been selected, a plot of the potential can be generated by simply clicking on the potential in the table. Blue is for the real part of the potential, red for the imaginary part.

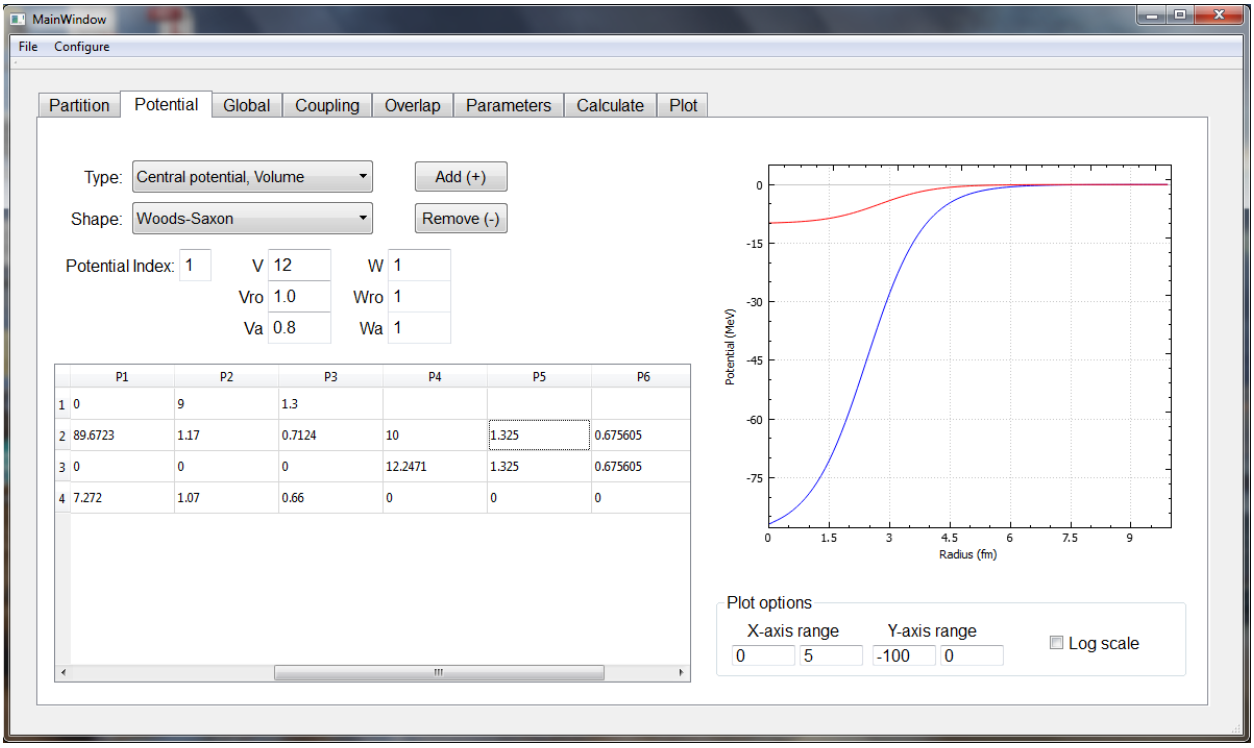

Figure I.2 – Potential tab used to input the potentials used in the calculated. Once a potential has been selected, a plot of the potential can be generated by simply clicking on the potential in the table.

If global OMPs are desired, the user can select the 'Global' tab and select the entrance or exit channel of the reaction, shown in Figure I.3. Once selected, a list of possible global potentials is generated with reaction parameters extracted from the 'Partition' tab. By clicking the 'Add (+)' button the global potential is added to the 'Potential' tab.

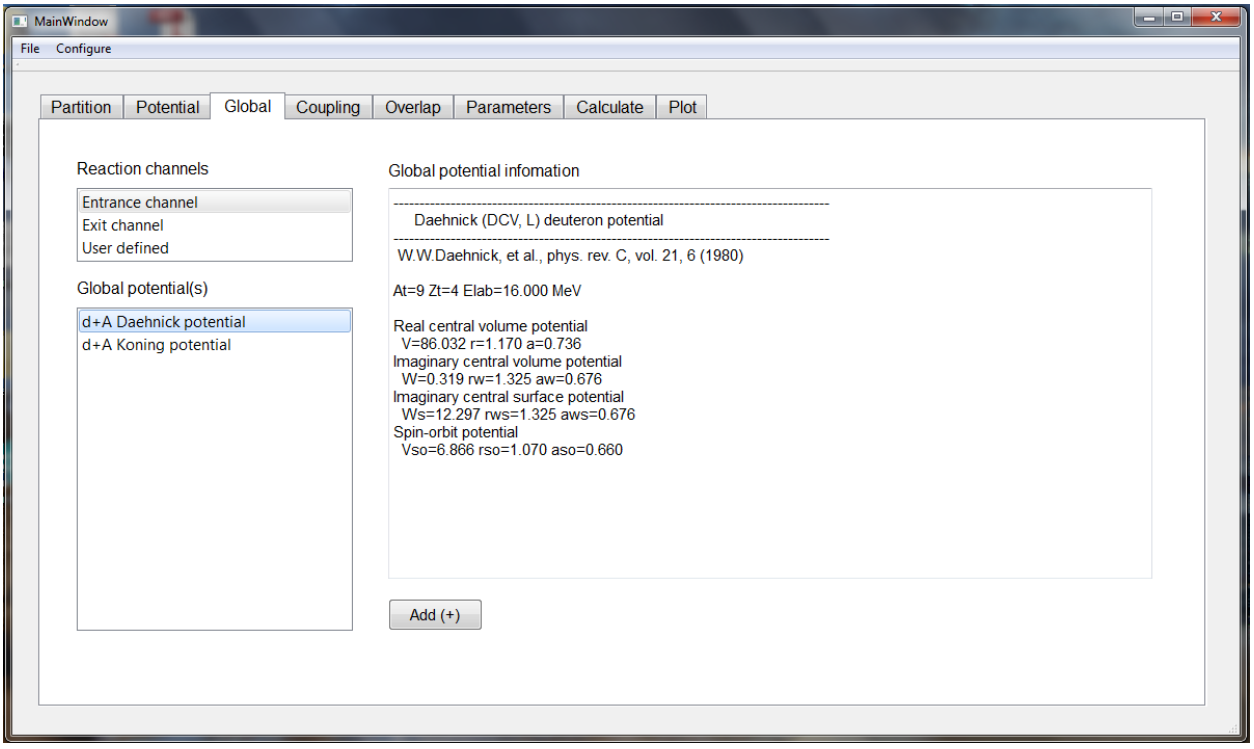

Figure I.3 – The Global tab used to select global OMPs used in the calculated. Once a global potential has been selected, clicking the 'Add (+)' button inputs the global OMP into the 'Potential' tab.

The other tabs in control various aspects of the calculation including coupling, the overlap integrals, and calculation parameters. Fresco can be started by selecting the 'Run' button in the 'Calculate' tab. Once the calculation is complete, the cross section can be plotted using the 'Plot' tab as shown in Figure I.4. The program is at an early stage and additional features will be added. Currently, enough interest from the low-energy nuclear physics community has been generated by this work that a crowd-source project has been setup to not only evaluate the program but also work on development of additional features such as adiabatic potentials, coupled channels, and others.

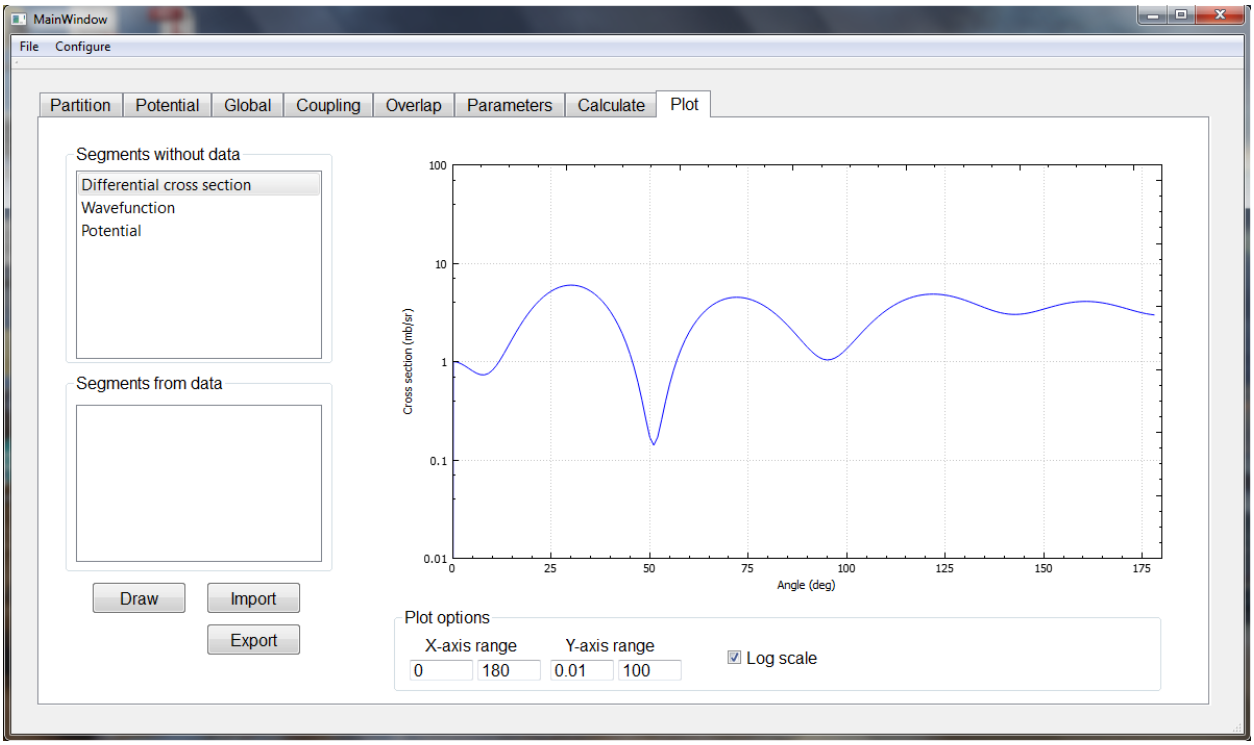

Figure I.4 – The Plot tab used to plot the calculation cross section. The cross section can then be exported to a standard ASCII text file.

REFERENCES

[9807B] ET Enterprises, Model 9807B 51 mm photomultiplier data sheet

[9821B] ET Enterprises, Model 9821B 78 mm photomultiplier data sheet

[R1250] Hamamatsu, Model R1250 127 mm photomultiplier data sheet

[Ale61] T.K Alexander and F.S. Goulding, "An Amplitude-Insensitive System that Distinguishes Pulses of Different Shapes", Nucl. Instrum. and Meth. **13** (1961) 244-246

[Asp07] M. D. Aspinall, B.D'Mellow, R.O. Mackin, et al., "The empirical characterization of organic liquid scintillator detectors by normalized averages of digitized pulse shapes", Nucl. Instrum. and Meth. **A578** (2007) 261-266.

[Bar77] C.M. Bartle, "Improved technique for the preparation of deuterated-polyethylene targets", Nucl. Instrum. Meth. **144** (1977) 599

[Bec69] F.D. Becchetti Jr, G.W. Greenlees, "Nucleon-nucleus optical-model parameters, A>40, E<50 MeV", Phys. Rev. **182** (1969) 1190-1209

[Bec76] F.D. Becchetti, C.E. Thorn, and M.J. Levine, "Response of Plastic Scintillator detectors to Heavy Ions, $Z \leq 35$, $E \leq 170$ MeV", Nucl. Instrum. and Meth. **136** (1976) 93-104.

[Bec03] F.D. Becchetti, M.Y.Lee, T.W.O'Donnell, D.A.Roberts, J.J. Kolata, L.O. Lamm, G. Rogachev, V. Guimaraes, P.A. DeYong, S.Vincent, "The TwinSol low-energy radioactive nuclear beam apparatus: status and recent results", Nucl. Instrum. and Meth. **A505** (2003) 377-380

[Ber04] C.A. Bertulani and P. Danelewicz, "Introduction to Nuclear Reactions", IOP Publishing, (2004).

[Ber07] C.A. Bertulani, "Nuclear physics in a nutshell", Princeton University Press, (2007).

[Bil13] V. Bildstein, P.E.Garrett, J.Wong, et al., "Comparison of deuterated and normal liquid scintillators for fast-neutron detection", Nucl. Instrum. Meth. **A 729** (2013) 188-197

[Boh72] W. Bohne, J. Bommer, H. Fuchs, K. Grabisch, H. Kluge, and G. Röschert, "Study of the (d,n) and (d,p) reactions on ^{15}N", Nucl. Phys. **A196** (1972) 41-57

[Bom71] J. Bommer, H. Fuchs, K. Grabisch, U. Janetzki, and G. Röschert, "Study of 15O states by the 14N(d,n) reaction", Nucl. Phys. **A172** (1971) 618-624

[Bor07] A. Borella, G. Aerts, F. Gunsing, M. Moxon, P. Schillebeeckx, R. Wynants, "The use of C6D6 for neutron induced capture cross-section measurement in the resonance region", Nucl. Instrum. and Meth. **A577** (2007) 626-640

[Bro58] F.B. Brooks, R.W. Pringle, and B.L. Funt, "Pulse shape discrimination in a plastic scintillator", IRE Trans. Nucl. Sci. NS-5 (1959) 35-38

[Bro79] F.D. Brooks, "Development of Organic Scintillators", Nucl. Instrum. Meth. **162** (1979) 477-505

[Bro81] F.D. Brooks, P.M. Lister, J.M. Nelson, and K.S. Dhuga, "Vector analyzing powers for the ^{12}C(d,n)^{13}N, ^{9}Be(d,n)^{10}B, and ^{28}Si(d,n)^{29}P reactions', AIP Conf. Proced. **69** (1981) 656-658

[Bro88] F.D. Brooks, W.A. Cilliers, B.R.S. Simson, F.D. Smit, M.S. Allie, D.T.L. Jones, W.R. McMurray, and J.V. Pilcher, "Deuterated Anthracene Spectrometer for 5-30 MeV Neutrons", Nucl. Instrum. and Meth. **A270** (1988) 149-156

[Bus74] C.E. Busch, T.B. Clegg, S.K. Datta, and E.J. Ludwig, "The cross section and vector analyzing power for the elastic scattering of 15.0 MeV deuterons from ^{10}B, ^{12}C, ^{13}C, ^{14}N, and ^{16}O", Nucl. Phys**. A223** (1974) 183-194

[CAN51] Model V1751, 4/8 Channel 10 bit 2/1 GS/s Digitizer, http://www.caen.it/csite/CaenProd.jsp?idmod=602&parent=11

[CAN42] Model V1742, 32+2 Channel 12bit 5 GS/s Switched Capacitor Digitizer, http://www.caen.it/csite/CaenProd.jsp?parent=11&idmod=661

[CAN56] Model SP5601, LED Driver, http://www.caen.it/jsp/Template2/CaenProd.jsp?parent=61&idmod=719

[Cow66] A.A. Cowley, G. Heymann, and R.L. Keizer, "Elastic and inelastic scattering of 15.8 MeV deuterons", Nucl. Phys. **86** (1966) 363-377

[Cro92] S. Croft, J.M. Adams, D.S.Bond, N.P. Hawkes, and N. Watkins, "A measurement of the light output function of the deuterated liquid scintillator NE-230 to recoil deuterons with energies between 0.62 and 14.5 MeV", Nucl. Instrum. and Meth. **A316** (1992) 324-332

[Cha83] M.B. Chatterjee, C. Pruneau, C. Rangacharyulu, and C. St-Pierre, "Self-supporting carbon targets by e-gun evaporation", Nucl. Instrum. and Meth**. 227** (1984) 15-18

[Dae80] W.W. Daehnick, J.D. Childs, and Z. Vrcelj, "Global optical model potential for elastic deuteron scattering from 12 to 90 MeV", Phys. Rev. **C21** (1980) 2253-2274

[Den70] D. Dehnhard and N. M. Hintz, "Octopole and quadrupole transition rates in 19F from scattering of 15-MeV deuterons", Phys. Rev. C **1** (1970) 460-467

[Die72] F.S. Dietrich, E.G. Adelberger, and W.E. Meyerhof, "Study of the ^{2}H(d,n)^{3}He reaction between 12 and 19 MeV", Nucl. Phys. **A184** (1972) 449-457

[Die82] G. Dietze and H. Klein, "Gamma-calibration of NE 213 scintillator counters", Nucl. Instrum. and Meth.**193** (1982) 549–556

[Doy08] James Doyle, "Nuclear Safeguards, Security, and Nonproliferation: Achieving Security with Technology and Policy", Elsevier Inc. (2008)

[Eljen] Eljen Technology, 1300 W. Broadway, Sweetwater, TX, 79556, USA

[Elj98] "MACHINING AND POLISHING OF PLASTIC SCINTILLATORS", Technical Library, Eljen Technology, 1300 W Broadway, Sweetwater, TX, 79556, USA.

[EJ309] "EJ309 Data Sheet", Eljen technology, 1300 W Broadway, Sweetwater, TX, 79556, USA.

[EJ315] "EJ315 Data Sheet", Eljen technology, 1300 W Broadway, Sweetwater, TX, 79556, USA.

[EJ315H] "EJ315 Data Sheet", Eljen technology, 1300 W Broadway, Sweetwater, TX, 79556, USA.

[EJ315M] C.Hurlbut, Private communication.

[Feb13] M. Febbraro, F.D. Becchetti, R.O. Torres-Isea, M. Ojaruega, A.M. Howard, J.J. Kolata, A. Roberts, A.N. Villano, "Neutron Spectroscopy Without Time-of-Flight Measurement: A DSP-Based Deuterated Scintillator Array", IEEE Trans. on Nucl. Sci. 60-2 (2013) 890-896.

[Feb14] M. Febbraro, F.D. Becchetti, R.O. Torres-Isea, A.M. Howard, A. Riggins, C. Lawrence, J.J. Kolata, "Systematic Study of (d,n) Reactions at E_d = 16 MeV Using a Deuterated Scintillator Array", EPJ Web of Conf. 66 (2014)

[Fen78] Da Hsuan Feng, K.N. Geller, and N. Klein, "Exact finite-range analysis of $^{12}C(^3He,n)^{14}N$ reaction", Phys. Rev. **C18** (1978) 33-40

[Fit67] W. Fitz, R. Jahr, and R. Santo, "Scattering and pickup reactions with deuterons on Be, B, C, N, and O at 11.8 MeV", Nucl. Phys. **A101** (1967) 449-459

[Fuc67] H. Fuchs, K. Grabisch, P. Kraaz, and G. Röschert, "States in ^{12}C and ^{16}O investigated by the $^{11}B(d,n)$ and $^{15}N(d,n)$ reactions", Nucl. Physics **A105** (1967) 590-600

[Gar13] P.E. Garrett, "DESCANT – the deuterated scintillator array for neutron tagging", Hyperfine Interact, 2013.

[Gle83] N.K. Glendenning, "Direct Nuclear Reactions", World Scientific Publishing Co., Toh Tuck Link, Singapore, (2004)

[Gör13] J. Görres, University of Notre Dame, private communication

[Har05] S. Harissopulos, H.W. Becker, J.W. Hammer, A. Lagoyannis, C. Rolfs, and F. Strider, "Cross section of the $^{13}C(\alpha,n)^{16}O$ reaction: A background for the measurement of geo-neutrinos", Phys. Rev. **C72** (2005)

[Hei08] M. Heil, R. Detwiler, R. E. Azuma, A. Couture, J. Daly, J. Görres, F. Kappeler, R. Reifarth, P. Tischhauser, C. Ugalde, and M. Wiescher, "The $^{13}C(\alpha, n)$ reaction and its role as a neutron source for the s process", Phys. Rev. **C78**, 025803 (2008)

[Hod94] P.E. Hodgson, "The Nucleon Optical Model", World Scientific Publishing (1994)

[Hor70] D.L. Horrocks, "Pulse Shape Discriminaiton with Organic Liquid Scnitllator Solutions", Applied Spectroscopy (1970), vol.24, no.4, pp.397-404.

[Hur14] C. Hurlbut, Eljen technologies, private communication

[Jon68] D.W. Jones, "A new circuit for pulse shape discrimination", IEEE Trans. Nuclear Sci. (1968) 491-499

[Kle02] H. Klein and S. Neumann, "Neutron and photon spectroscopy with liquid scintillation detectors in mixed fields", Nucl. Instrum. and Meth. **A476** (2002) 132-142

[Kno00] G.F. Knoll, "Radiation Detection and Measurement", 3rd edition, (John Wiley & Sons, 2000).

[Kor03] N. V. Kornilov, V. A. Khriatchkov, M. Duraev, et al., "Neutron spectroscopy with a fast waveform digitizer", Nucl. Instrum. and Meth. **A497** (2003) 467-478

[Law13] C.C. Lawrence, A. Enqvist, M. Flaska, S.A. Pozzi, A.M. Howard, J.J. Kolata, F.D. Becchetti, "Response characterization for an EJ315 deuterated organic-liquid scintillation detector for neutron spectroscopy", Nucl. Instrum. and Meth. **A727** (2013) 21-28.

[Law132] C.C. Lawrence, A. Enqvist, M. Flaska, S.A. Pozzi, F.D. Becchetti, "Comparision of spectrum-unfolding performance of (EJ315) and (EJ309) liquid scintillators on measured ^{252}Cf pulse-height spectra", Nucl. Instrum. and Meth. **A729** (2013) 924-929.

[Law14] C.C. Lawrence, Ph.D. Dissertation, University of Michigan, Ann Arbor (2014)

[Lee64] L.L.Lee Jr, J.P. Schiffer, B. Zeidman, G.R. Satchler, R.M. Drisko, and R.H. Bassel, "^{10}Ca(d,p)^{41}Ca, a test of the validity of the distorted-wave born approximation", Phys. Rev. **136** (1964) 971-993

[Lee99] M.Y. Lee, F.D. Becchetti, T.W. O'Donnell, D.A. Roberts, J.A. Zimmerman, V.Guimaraes, J.J Kolata, D. Peterson, P.Santi, P.A. DeYoung, G.F. Peaslee, J.D. Hinnefeld, "Study of nuclear reactions with intense, high-purity, low-energy radioactive ion beams using a versatile multi-congiuration dual superconducting-solenoid system", Nucl. Instrum. and Meth. **A422** (1999) 536-540

[Leh68] R.L. Lehman, "The orgin of neutron groups in Be(α,n) sources", Nucl. Instrum. and Meth. **60** (1968) 253-260

[Li76] T.K. Li, D. Dehnhard, R. E. Brown, and P.J. Ellis, "Investiagation of the $(d_{5/2})^2$ and $(d_{5/2}s_{1/2})$ two-particle configurations in ^{18}O using the ^{17}O(d,p)^{18}O reaction at 18 MeV"

[Lis81] P.M. Lister, "Experimental reactions studies with polarized ion beams", PhD dissertation, Univ. of Birmingham, Dept. of Phys. (1981)

[Liu09] G. Liu, M. D. Aspinall, X. Ma, et al., "An investigation of the digital discrimination of neutrons and γ rays with organic scintillator detectors using an artificial neural network", Nucl. Instrum. and Meth. **A607** (2009) 620-628

[Luo10] Xiaoliang Luo, Guofu Liu, and Jun Yang, "Neutron/Gamma Discrimination Utilizing Fuzzy C-Means Clustering of the Signal from the Liquid Scintillator", 2010 First Inter. Conf. on Pervasive Computing, Signal Processing and App., 2010

[Mat69] S. Matsuki, S. Yamashita, K. Fukunaga, D.C. Nguyen, N. Fujiwara, and T. Yanabu, "Elastic and inelastic scattering of 14.7 MeV deuterons and of 29.4 MeV alpha-particles by ^{6}Li and ^{7}Li", Journal Phys. Soc. Japan **26** (1969)

[Mat02] M. Matzke, "Propagation of uncertainties in unfolding procedures", Nucl. Instrum. and Meth. **A476** (2002) 230-241

[Mel07] B. D'Mellow, M. D. Aspinall, R. O. Mackin, et al., "Digital discrimination of neutrons and γ-rays in liquid scintillators using pulse gradient analysis", Nucl. Instrum. and Meth. **A578** (2007) 191-197

[Mon06] M. Montalti, A. Credi, L. Prodi, and M.T. Gandolfi, "Handbook of Photochemistry", 3rd edition, (Taylor and Francis, Boca Raton, Fl, USA, 2006).

[Mut71] G.S. Mutchler, D. Rendic, D.E. Velkley, W.E. Sweeney, Jr., and G.C. Phillips, "The (d,n) reaction on 1p shell nuclei at E_d = 11.8 MeV", Nucl. Phys. **A172** (1971) 469-488

[Naq94] A.A. Naqvi, M.A. Al-Ohali, M.M. Nagadi, A. Bari, "Response function measurement of a deuterated scintillator using a 241Am-Be source", Nucl. Instrum. and Meth. **A353** (1994) 156-159

[Nil08] T. Nilsson, "Radioactive ion beams at FAIR-NuSTAR", Eur. Phys. J. Special Topics 156 (2008) 1-12

[Oja10] M. Ojaruega, F.D. Becchetti, A.N. Villano, H. Jiang, R.O. Torres-Isea, J.J. Kolata, A. Roberts, C.C. Lawrence, "Evaluation of Large Deuterated Scintillator for Fast Neutron Detection (E=0.5-20 MeV) using the d(d,n)^{3}He, ^{13}C(d,n) and ^{27}Al(d,n) reactions", Nucl. Instrum. and Meth. **A652** (2011) 397-399

[Owe62] R.B. Owen, "Pulse Shape Discrimination – A Survey of the Current Techniques", IRE Trans. Nucl. Sci., vol. NS-9 (1962) 285-293

[Par73] Y.S. Park, A. Niiler, and R.A. Lindgren, "Spectroscopy of ^{10}B from ^{9}Be(d,n)^{10}B Reaction", Nucl. Phys. **C8** (1973) 1557 - 1572

[Pau14] S.V. Paulauska, M. Madurga, R.Grzywacz, D.Miller, S. Padgett, H.Tan, "A digitial data acquisition framework for the Versatile Array of Neutron Detector for Low Energy (VANDLE)", Nucl. Instrum. and Meth. **A737** (2014) 22-28

[Pau75] G. Pauletta and F.D. Brooks, "Cross section for the n+d breakup reaction", Nucl. Phys. **A255** (1975) 267-274

[Peh13] B. Pehlivanovic, S. Avdic, P. Marinkovic, S.A. Pozzi, M. Flaska, "Comparison of unfolding approaches for monoenergetic and continuous fast-neutron energy specta", Rad. Measurements **49** (2013) 109-114

[Pie15] B.Pierson, et al., (to be published)

[Pla03] R. Plag, M. Heil, F. Käppeler, P. Pavlopoulos, R. Reifarth, K. Wisshak, "An optimized C6D6 detector for studies of resonace-dominated (n,γ) cross-sections", Nucl. Instrum. and Meth. **A496** (2003) 425-436

[Poz03] S.A. Pozzi, E. Padovani, M. Marseguerra, "MCPN-PoliMi: a Monte Carlo code for correlation measurements", Nucl. Instrum. and Meth. **A513** (2003)

[Ram83] E. Ramström and D. Trostell, "A method for the preparation of 13C targets by the cracking procedure", Nucl. Intrum. and Meth. **219** (1984) 438-439

[Reg02] M. Reginatto, P. Goldhagen, S. Neumann, "Spectrum unfolding, sensitivity analysis and propagation of uncertainties with maximum entropy deconvolution code MAXED", Nucl. Instrum. and Meth. A476 (2002) 242-246

[Rob90] D.A. Roberts, F.D. Becchetti, E.Ben-Jacob, P. Garik, J. Musser, B. Orr, G. Tarle, A. Tomasch, J.S. Holder, D. Redina, B. Heuser, and G. Wicker, "Energy and flux limits of cold-fusion neutrons using a deuterated liquid scintillator", Phys. Rev. **C42** (1990)

[Rob92] D.A. Roberts, F.D. Becchetti, K. Ashktorab, D. Stewart, J. Jänecke, H.R. Gustafson, and M.J. Dueweke, "Deuterated Liquid scintillator (NE230) as a fast neutron detector for cold-fusion and other research", IEEE TNS 39 (1992) 32-535

[Rob95] D.A. Roberts, K. Ashktorab, F.D. Becchetti, J. Jänecke, M.N. Harakh, S.Y. van der Werf, G.P.A. Berg, C.C. Foster, J.E. Lisantti, T. Rinckel, E.J. Stephenson, S.P. Wells, A. Nadasen, S. Shaheen, "Neutron decay from the isobaric analog state in ^{120}Sb populated in ^{120}Sn(^{3}He,t)120Sb at E(^{3}He) = 200 MeV, θ = 0º", Phys. Rev. **C52** (1995) 1361-1367

[Rob13] A. Roberts, A.M. Howard, J.J. Kolata, A.N. Villano, F.D. Becchetti, P.A. Young, M. Febbraro, S.J. Freeman, B.P. Kay, S.A. McAllister, A.J. Mitchell, J.P. Schiffer, J.S. Thomas, and R.O. Torres-Isea, "Proton pari correlations and the neutrinoless double-β decay of ^{76}Ge", Phys. Rev. **C87** (2013)

[Ron09] E. Ronchi, P.-A. Söderström, J. Nyberg, et al., "An Artificial Neutral Network based neutron-gamma discrimination and pile-up rejection…", Nucl. Instrum. and Meth. **A610** (2009) 534-539

[Rou64] M.J. Roush, M.A. Wilson, and W.F. Hornyak, "Pulse shape discrimination", Nucl. Instrum. and Meth. **31** (1964) 122-124

[Rut11] E. Rutherford, "The Scattering of α and β Particles by Matter and the Structure of the Atom", Philosophical Magazine **21** (1911) 669-688

[Sat83] G.R. Satchler, “Direct Nuclear Reactions”, International Series of Monographs on Physics 68, Oxford University Press, Walton Street, Oxford, (1983)

[Sch84] H.R. Schelin, E. Farrelly Pessoa, W.R. Wylie, E.W. Cybulska, K. Nakayama, and L.M. Fagundes, “The $^{12}C(d,n)^{13}N$ reaction between E_d = 7.0 and 13.0 MeV”, Nucl. Phys. **A414** (1984) 67-84

[Smi68] D.L. Smith, R.G. Polk, and T.G. Miller, “Measurement of the response of several organic scintillators to electrons, protons, and deuterons”, Nucl. Instrum. and Meth. **64** (1968) 157-166

[Stu50] Model SIS3150-USB USB2.0 to VME interface, http://www.struck.de/sis3150usb.htm

[Tom71] M.E. Toms, “A computer analysis to obtain neutron spectra from an organic scintillator”, Nucl. Instrum. and Meth. **92** (1971) 61-70

[Tho88] I. J. Thompson, Comput. Phys. Rep. **7, 167** (1988), URL: http://www.fresco.org.uk.

[Tho10] M. Thoennessen, “Plans for the Facility for Rare Isotope Beams”, Nucl. Phys. **A834** (2010) 688-693

[Tor86] W. Tornow, W. Arnold, J. Herdtweck, and G. Mertens, “Measurement of the response of the deuterated scintillators NE-232 and NE 230 to protons and deuterons”, Nucl. Instrum. and Meth. **A244** 477-483

[Uwa82] Y. Uwamino, K. Shin, M. Fujii, and T. Nakamura, “Light output and response function of an NE-213 scintillator to neutrons up to 100 MeV”, Nucl. Instrum. and Meth. **204** (1982) 179-189

[Var91] R.L. Varner, W.J. Thompson, T.L. McAbee, E.J. Ludwig, T.B. Clegg, “A global nucleon optical model potential”, Phys. Rep. 201 (1991) 57-119

[Vil11] A.N. Villano, F.D. Becchetti, J.J. Kolata, M. Ojaruega, A. Roberts, “Efficiency measurements of deuterated liquid scintillators using d(d,n)3He coincidence events”, Nucl. Instrum. and Meth. (2011) 280-283

[You09] S. Yousefi, L. Lucchese, “Digital discrimination of neutrons and gamma rays in liquid scintillators using wavelets”, Nucl. Instrum. and Meth. **A598** (2009) 551-555

[War68] S.I. Warshaw, A.J. Buffa, J.B. Barengoltz, and M.K. Brussel, “Elastic scattering of 3He from 12C from 18 to 24 MeV”, Nucl. Phys. **A121** (1968) 350-366

[Zei74] B. Zeitnitz, R. Maschuw, P. Shur, W. Ebenhoeh, J. Bruinsma, and J.H. Stuivenberg, “Neutron-neutron effective range parameters from kinematically complete experiments on the reaction $^{2}H(n,2n)^{1}H$”, Nucl. Phys. **A231** (1974) 13-28

[Zai12] N. Zaitseva, B.L.Rupert, I. Pawelczak, A. Glenn,H.P. Martinez, L.Carman, M. Faust, N.Cherepy, S.Payne, “Plastic scintillators with efficient neutron/gamma pulse shape discrimination”, Nucl. Instrum. and Meth. **A668** (2012) 88–93